FACULTY OF SCIENCE AND TECHNOLOGY

MASTER THESIS

Study programme / specialisation:
Marine and Offshore Technology

The spring semester, 2022

Open / ~~Confidential~~

Author:
Agata Patrycja Jurga

.....Jurga.....
(signature author)

Course coordinator:
Prof. Yihan Xing
Supervisor(s):
Prof. Muk Chen Ong
Dr. Guang Yin
Marek Jan Janocha

Thesis title:

Numerical Simulations of Turbulent Flow through Piping Systems

Credits (ECTS): 30

Keywords:

Pages: 109

Computational Fluid Dynamic, CFD, OpenFoam, Turbulent flow, Orifice Flowmeter, Pipe bend, Flow conditioner, Honeycomb straightener,

+ appendix: 0

Stavanger, June 15/2022
date/year

To Kuba

Acknowledgements

I would like to thank Professor Muk Chen Ong for convincing me to choose the Marine and Offshore Technology master programme at the University of Stavanger. It proved to be a great adventure not only with regards to the knowledge I gained but also professionals I had an opportunity to work with. I wish to express my profound gratitude to Professor Muk Chen Ong for offering me his best CFD experts for cooperation: Dr. Guang Yin and Marek Jan Janocha whose assistance was invaluable in carrying out this work. Furthermore, Professor Muk Chen Ong has my deepest thanks for his motivating guidance which contributed a lot to my personal development.

I would like to express my sincere appreciation to Dr. Guang Yin and Marek Jan Janocha for their readiness to help, technical support and engagement during my research work. I am also grateful to Dr. Guang Yin and Marek Jan Janocha for thorough CFD discussions from which I benefited a lot.

I wish also to thank the University of Stavanger, Department of Mechanical and Structural Engineering and Materials Science for providing the necessary resources to successfully complete the studies.

Finally, I would like to express my special thanks to my parents and my brother, Jakub, for their encouragement and everlasting love. My heartfelt gratitude goes to Jakub for always being there for me to share his technical skills and raise my spirits during my studies.

Abstract

Piping systems have a wide range of applications across many different industries. Pipelines are essential infrastructure in the offshore oil & gas installations. One of the key challenges when operating complicated piping systems is accurate measurement of the flow characteristics required for example to optimize the process or maintain the flow assurance. The pipe fittings such as elbows, bends, and reducers introduce disturbance in the flow and distort the velocity profile downstream in the pipe which adversely affects the accuracy of flowmeter devices. To counteract these undesired effects, various types of flow conditioners can be installed between the source of flow disturbance and the measuring device. In this thesis, the behavior of turbulent flow passing through three different components of the piping systems is investigated: an orifice plate, a 90-degree pipe bend and thereafter a honeycomb straightener. The Reynolds numbers in present analyses range from 1×10^4 to $\leq 2\times10^5$. First, a validation study of eight different Reynolds-Averaged Navier–Stokes (RANS) turbulence models is performed to choose the model that gives the best prediction of the fluid flow through an orifice flowmeter. Among the benchmarked models, the Explicit Algebraic Reynolds Stress Model (EARSM) shows the best agreement with the experimental validation data. In the second part, the validated turbulence model is used to study the effects of different pipe bend geometries and Reynolds number (Re) on the flow behavior. Based on further numerical simulations of the flow through the pipe bend, it is found that for small curvature radiuses ($Rc/D < 2$), the velocity profiles are highly deformed and separation bubble develops behind the bend. Finally, the influence of a new honeycomb straightener design on the flow quality is investigated downstream of the 90-degree pipe bend. The case of pipe bend with $Rc/D = 2$ is employed to that end. It is concluded that the optimum effectiveness in eliminating the swirl and improving the velocity profile pattern is reached for the honeycomb straightener located at the minimum distance from the bend outlet of $Lb = 5$ and thickness of $t = 0.5$. Furthermore, a detail description of the investigated flow fields are presented in terms of axial velocity profiles, turbulence intensity, velocity perturbation, pressure, vortex formations, secondary flow regions, streamline patterns and swirl intensity.

List of Appended Publications

Paper 1

Jurga, A.P., Janocha, M.J., Yin, G., Giljarhus, K.E.T. and Ong, M.C., 2021. Validation and assessment of different RANS turbulence models for simulating turbulent flow through an orifice plate. In IOP Conference Series: Material Science Engineering, 1201, pp. 012019.

Paper 2

Jurga, A.P., Janocha, M.J., Yin, G. and Ong, M.C., 2022. Numerical simulations of turbulent flow through a 90-degree pipe bend. Journal of Offshore Mechanics and Arctic Engineering. (Under review).

Paper 3

Jurga, A.P., Janocha, M.J., Yin, G. and Ong, M.C., 2022. Numerical investigations of turbulent flow through a 90-degree pipe bend and honeycomb straightener. (Draft). To be submitted to Journal of Offshore Mechanics and Arctic Engineering.

Table of contents

Chapter 1.

Introduction

1.1. Background and motivation

Pipelines account for the largest network of fluid transportation in the world. An important part of the piping system are fittings such as elbows, bends, reducers or Tee-junctions. Pipe fittings connect straight segments of pipes, adjust to different sizes or change the direction of the fluid flow. Important design consideration in piping systems is ability to measure fluid variables such as the pressure and the velocity in a pipe. Only by measuring accurately the main fluid characteristics, a better control of the fluid flow can be achieved. Errors in flow measurement can lead to huge cost and affect adversely efficiency. Especially in the oil and gas industry, the enormous financial loss could result from even small measurement errors due to the great volumes involved in the transfer of oil and natural gas. In order to obtain an accurate flow measurement in a pipe, the flow directly before the meter needs to be fully developed and free from swirl and distortion which is caused by the pipe fitting. The required fully developed flow profile can be achieved by providing straight pipe sections of sufficient length which is often not possible due to the limited space in the piping network. Whenever the straight pipe sections of sufficient length cannot be provided, the most practical way to solve this issue is by using flow conditioners. Flow conditioners are effective devices for reducing the flow meter errors due to swirl and flow profile distortion. Whereas the most popular devices used for measurement and control of a fluid flow in a pipe are orifice plates. As presented in Figure 1.1, the flow metering process is closely related to the flow conditioning which has a huge impact on improving the accuracy of the measurement performance. Fluid flow becomes distorted due to the pipe fittings and that distorted velocity profile requires recovery before it can be measured accurately by the flow meter. With the help of numerical simulations, the flow characteristics such as the pressure drop, velocity distributions or swirl intensity can be found and evaluated before and after installing the flow conditioner. Thus, numerical studies are useful in designing piping networks where consistent delivery pressures and flow rates are the key factors.

There has been extensive research in the past to find the successful way to protect the flowmeters from piping-induced disturbances. There are a large number of experimental and numerical studies on the flow through piping systems, including orifice flowmeter, pipe bends and flow conditioners. Some experimental studies on the flow through an orifice were conducted by Johansen [9] who first studied the orifice flow, Sahin et al. [8] or Tunay [7] who investigated the combination of different geometries of the orifice, Reynolds numbers and their dependence on the discharge coefficient. One of the mainly used fittings causing active flow profile disturbances in industrial piping system is a pipe

bend. The first experimental observation of the secondary flow was made in 1876 by Thomson [14] and later investigated by Williams et al. [15] and Eustice [16]. Dean [17], [18] was the first who formulated a mathematical solution for the secondary flow and implement the dimensionless parameter called Dean number. Enayet et al. [19], Azzola et al. [20] and Shiraishi et al. [21] performed LDV (Laser Doppler Velocimetry) measurements of the velocity for turbulent flow in a pipe bend. It was found that the velocity flow pattern was independent of the Reynolds number but influenced by the change of the curvature radius. Many numerical simulations have also been performed to study the flow in piping networks. Computational Fluid Dynamics (CFD) has been proved to be a powerful tool, e.g., to capture more information about the flow in the separation region behind the orifice plate. Sahin et al. [8] observed two eddies in the upstream and downstream side of the orifice plate by plotting the streamlines. For turbulent flow conditions, the Reynolds-averaged Navier–Stokes (RANS) equations combined with the standard $k-\varepsilon$ model were used in numerical studies of Hollingshead [10] and Ding et al. [11] who investigated the discharge coefficient and the energy dissipation, respectively, with different shapes of the orifice. Eiamsa-ard et al. [12] examined the effect of different turbulence models on the flow characteristic through the orifice and it was found that the Reynolds stress model (RSM) gave better performance than the standard $k-\varepsilon$. Jurga et al. [13], as a part of this thesis in Chapter 3, evaluated the performance of different RANS turbulence models and concluded that the EARSM model, which was used for the first time to predict the turbulent flow through the orifice plate, had the best agreement with experimental data compared with other turbulence models. Also, numerical simulations have been employed to study the flow inside the curved pipes for different geometry and Reynolds numbers. Dutta et al. [22], [23], [24] investigated the influence of Reynolds numbers on the flow separation employing the $k-\varepsilon$ turbulence model. Dutta found that the flow separation could be clearly observed for Rc/D = 1, for which the flow became complex and unsteady downstream of the 90-degree bend. Kim et al. [25] found that among the investigated models, the $k-\varepsilon$ RNG (Re-Normalization Group) model gave a good prediction in the swirl intensity of the secondary flow. Tanaka et. al. [26] employed the Large Eddy Simulation (LES) approach and the results showed good agreement with the experimental data. Jurga et al. [2], as a apart of this thesis in Chapter 4, studied the effects of the curvature radius (Rc) and Reynolds number (Re) on the flow development in the 90-degree pipe bend by employing the EARSM model to resolve the Reynolds stresses. It was concluded that the flow is highly deformed and velocity profiles are skewed for $Rc/D < 2$, while the influence of the Re in range $1\times10^4 \leq \mathrm{Re} \leq 6\times10^4$ on the flow behaviour is small. These observations result, as expected, was also predicted by a lot of earlier research.

The observed effects of upstream bends has an adverse influence on orifice flow meters which was documented by numbers of tests and reported by Branch [3] and Martin [4]. Their results showed that when the orifice plate was positioned closer to the bend, the orifice discharge coefficient decreased what resulted in significant measurement

deviations due to the presence of swirl and distorted velocity profile. A good solution to correct the discharge coefficient error and achieve the desired flow meter accuracy is attained by using flow conditioning. The flow straighteners and conditioners have been used for many years to attempt to improve the velocity profile that has been disturbed by upstream fittings. In order to check the effectiveness of flow conditioners, they were studied together with the flow meters to test their effect on the performance and sensitivity of the measurements. Thus, the two main parameters were assessed, the swirling strength and velocity profile. The first experimental observation of the swirl was made in 1964 by Chigier et al. [5]. A series of swirling air jets, generated by different types of nozzles, were studied with respect to static pressure and axial, radial and tangential components of velocity which resulted in defining the strength of the swirl as the swirl number. The swirl number is used to assess the strength of a swirl around the axis of the main flow. Thus, swirling flow can be defined as a flow that rotates and axially moves along the direction of the flow. Also, the swirl number defined as the ratio of the axial flux of angular momentum to the axial flux of axial momentum was introduced by Gupta et al. [6] who measured the degree of swirl present in the flow in terms of the angular momentum of the combustion air. Mattingly et al. [27] studied the effect of the tube bundle straightener on distorted profile upstream of the orifice meters. Experiments were measured with LDV and the pipe bend geometry was applied as a source of disturbance. Kinghorn et al. [28] evaluated effectiveness of the Etoile straightener of different lengths in removing swirl upstream of the orifice plate which was generated by a vane damper control valve. Hogendoorn et al. [29] compared the effects of ISO tube bundle and the Etoile flow straighteners on flow profile disturbances. Also, numerical research have been focused on investigations of the effectiveness of a flow conditioner. Yehia et al. [30] studied swirling turbulent flow through the Zanker plate in a straight pipe using the Detached Eddy Simulation (DES) and proved that the swirl angle and tangential velocity decrease with the increasing plate thickness. Hallanger [31] assessed the influence of flow conditioners on liquid ultrasonic flow meter by employing $k-\omega$ turbulence model. The results showed that the more stable flow was achieved with the Etoile straightener than the tube bundle. Jurga et al. [32], as a part of this thesis in Chapter 5, evaluated the effectiveness of the honeycomb straightener at the different distances from the bend outlet (Lb) and different values of the honeycomb thickness (t) using the EARSM model. The honeycomb straightener reached the best performance at the minimum distance of $Lb = 5D$ and thickness $t = 0.5$ where the swirl was almost completely removed.

In this thesis, numerical simulations are used to study the behaviour of the turbulent flow through the 90-degree pipe bend without and after installing the honeycomb straightener. A Computational Fluid Dynamics (CFD)-based approach has been presented to help understand the complex flow pattern induced by the pipe curvature. A CFD approach brings several benefits. Numerical analysis save time in the design process and are therefore cheaper and faster compared to physical testing procedures. The parametric

studies are performed to evaluate dependency among various parameters, where one of them is varied and the others are kept unchanged. This allows to evaluate the influences of the parameters by investigating the detailed flow physics. Also, numerical studies go beyond experimental limitations caused by restricted capacity of available facilities to perform traditional tests. However, CFD analysis only approximate a real physical solution and conventional testing procedures cannot be totally excluded, and which should still be performed for validation tests purposes.

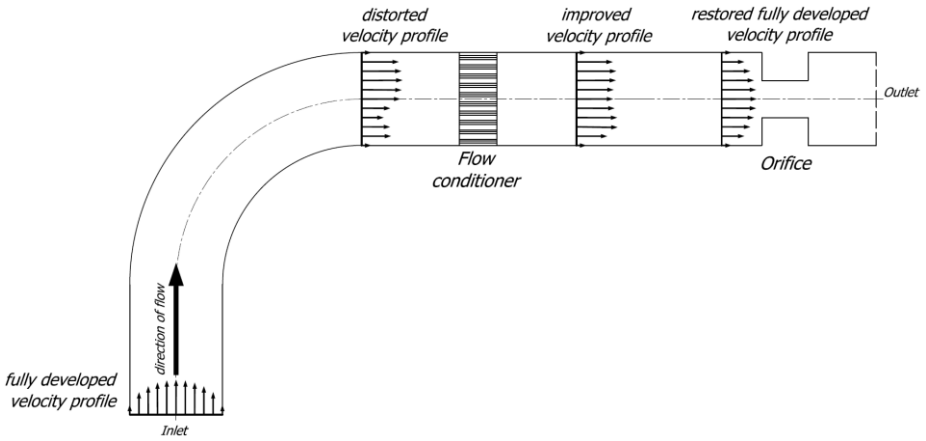

Figure 1.1. An example of flow measurement layout using a flow conditioner and an orifice meter in a flow through 90-degree pipe bend.

1.2. Objectives and methodology

The objective of this study is to better understand the turbulent flow behavior in piping systems with complex geometry. The numerical modelling aspect is explored by validating selected turbulence models with respect to their ability to predict the flow characteristics. Therefore, this investigation is performed to achieve a better understanding of the flow straightening mechanism followed by studies of the orifice flow and upstream bend configurations characterized by strong flow anisotropy. Accordingly, in this thesis, the behavior of turbulent flow is studied through three different components of the piping systems: an orifice plate, a 90-degree pipe bend and thereafter a honeycomb straightener. The objectives are to evaluate the behavior of various RANS turbulence models to determine the best prediction of the fluid flow through an orifice plate, investigate the effects of different values of the curvature radius (Rc) and Reynolds numbers (Re) on the flow development in the circular 90-degree pipe bend and assess the effectiveness of the honeycomb on suppressing the flow swirling for different distances from the bend outlet (Lb) and different values of the honeycomb thickness (t). The goal of a honeycomb geometry is to check if the regular hexagonal pattern, as illustrated in Figure 1.2, could bring the improvements in desired flow conditions.

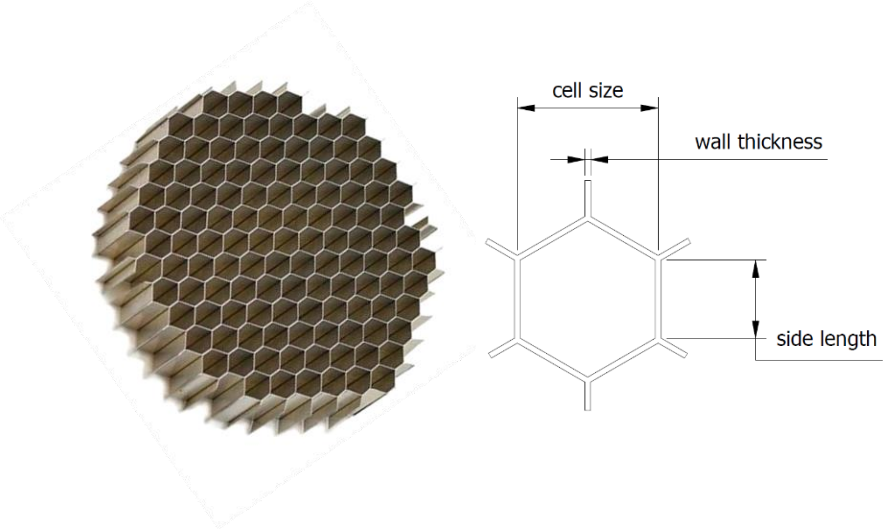

Figure 1.2. An example of the honeycomb flow straightener with a 5 mm cell size [1].

Methodology is based on the numerical study of the flow by using an open-source finite volume method CFD code OpenFOAM v2012 to solve the governing equations of the fluid flow. The turbulent flow is investigated by carrying out the numerical simulations using the Reynolds-Averaged Navier–Stokes (RANS) turbulence model in the present study. The results obtained from numerical model are validated against the previous published numerical and experimental data.

The main objectives established in the present thesis are explored within the scope of the appended publications and are listed as follows:

First research questions: What are the key flow parameters used to evaluate the behavior of various turbulence models to investigate the turbulent flow through the orifice plate? What are the obtained results when compared with available published experimental data? Which turbulence model has the best performance in predicting the turbulent flow in a piping system with complex geometry?

Second research questions: What are the key flow parameters used to evaluate the behaviour of the turbulent flow through a 90-degree pipe bend employing the Explicit Algebraic Reynolds Stress Model (EARSM)? What are the effects of different values of Rc and different Re on the flow development in a pipe bend?

Third research questions: What are the key flow parameters used to investigate the turbulent flow through a 90-degree pipe bend with the honeycomb straightener? What are the effects of different installation distances of the honeycomb (Lb) and different values of the honeycomb thickness (t) on the flow development downstream of the bend outlet?

1.3. Thesis structure

The contents of each chapter are summarized in the following.

Chapter 2: The second chapter presents the review of the theoretical background and previous research with emphasis on selected piping system elements: the orifice flow meter, 90-degree pipe bend and flow conditioner.

Chapter 3: Validation and assessment of different RANS turbulence models for simulating turbulent flow through an orifice plate. This chapter contains the conference paper presented at the Third Conference of Computational Methods & Ocean Technology (COTech 2021) in November 2021. It treats the behaviour of various RANS models, with respect to the pressure drop, velocity distributions and turbulence intensity profiles, by comparing the results with available published experimental data.

Chapter 4: Numerical simulations of turbulent flow through a 90-degree pipe bend. This chapter holds the paper which is under review at the Journal of Offshore Mechanics and Arctic Engineering. Presented study considers the influence of the different pipe curvature and different Re on the flow through a pipe bend using EARSM turbulence model. The main flow characteristics examined here are the axial velocity, the velocity perturbation, the pressure difference and vortical structure.

Chapter 5: Numerical investigations of turbulent flow through a 90-degree pipe bend and honeycomb straightener. This chapter constitutes the paper draft which will be submitted to the Journal of Offshore Mechanics and Arctic Engineering and presents the main theme of the thesis. The research evaluates the effectiveness of the honeycomb straightener installed downstream of the 90-degree bend pipe, at different locations from the bend outlet (Lb) and with different honeycomb thicknesses (t). The swirl and velocity profile are the key parameters covered here.

Chapter 6: Conclusions and recommendations for future work.

References

[1] Performance MRP 2022, Air Straightener Screen, https://performancemrp.com/, Accessed: 02.06.2022.

[2] Jurga, A.P., Janocha, M.J., Yin, G. and Ong, M.C., 2022. Numerical simulations of turbulent flow through a 90-degree pipe bend*J. Offshore Mech. Arct. Eng.* (Under review).

[3] Branch, J. C., 1995. The effect of an upstream short radius elbow and pressure tap location on orifice discharge coefficients. *Flow Meas. Instrum*., 6, pp. 157-62.

[4] Martin, C. N. B., 1986. Effects of upstream bends and valves on oritice plate pressure distributtons and discharge coefficients. *Int. J. Heat Fluid Flow*, 3(3), pp. 135-141.

[5] Chigier, N. A., and Beér, J. M., 1964. Velocity and Static-Pressure Distributions in Swirling Air Jets Issuing From Annular and Divergent Nozzles. *Journal of Basic Engineering*, 86(4), pp. 788.

[6] Gupta, A. K., Lilley, D. G. and Syred, N., 1984. *Swirl Flows*. Abacus Press, Tunbridge Wells, England.

[7] Tunay, T., Sahin, B. and Akilli, H., 2004. Investigation of Laminar and Turbulent Flow Through an Orifice Plate Inserted in a Pipe. *Trans. Can. Soc. Mech. Eng*., 28(2B), pp. 403-414.

[8] Sahin, B. and Ceyhan, H., 1996. Numerical and Experimental Analysis of Laminar Flow Through Square-Edged Orifice With Variable Thickness. *Trans. Inst. Meas. Control*, 18(4), pp. 166-174.

[9] Johansen, F.C., 1930. Flow Through Pipe Orifices at Low Reynolds Numbers. *Proc. R. Soc. A*, 126(801), pp. 231-245.

[10] Hollingshead, C.L., Johnson, M.C., Barfuss, SL. and Spall, R.E., 2011. Discharge Coefficient Performance of Venturi, Standard Concentric Orifice Plate, V-Cone and Wedge Flow Meters at Low Reynolds Numbers. *J. Pet. Sci. Eng*., 78(3–4), pp. 559-566.

[11] Ding, T.M. and Wang, Y., 2015, Comparison Research on Hydraulic Characteristics of Three Type's Orifice Plate. *Open Fuels Energy Sci. J.,* 8(1), pp. 43-46.

[12] Eiamsa-ard, S., Ridluan, A., Somravysin, P., Promvonge, P. and Chok, N., 2008. Numerical Investigation of Turbulent Flow Through a Circular Orifice. *KMITL Sci. J*, 8(1), pp. 44-50

[13] Jurga, A.P., Janocha, M.J., Yin, G., Giljarhus, K.E.T. and Ong, M.C., 2021. Validation and assessment of different RANS turbulence models for simulating turbulent flow through an orifice plate. *IOP Conf. Ser.: Mater. Sci. Eng.* 1201, pp. 012019.

[14] Thomson, J., 1876. On the origin of windings of rivers in alluvial plains, with remarks on the flow of water round bends in pipes. *Proc. R. Soc. London*, 25, pp. 5-8.

[15] Williams, G.S., Hubbell, C.W. and Finkell, G.H., 1902. Experiments at Detroit, Michigan on the effect of curvature on the flow of water in pipes. *Trans. ASCE*, 47, pp.1-196.

[16] Eustice, J., 1911. Experiments of Streamline Motion in Curved Pipe. *Proc. R. Soc. London, Ser. A*, 85, pp.119-131.

[17] Dean, W.R., 1927. Note on the Motion of Fluid in a Curved Pipe. *Philosophical Magazine and Journal of Science*, 20(4), pp. 208-223.

[18] Dean, W.R., 1928. The Stream-line Motion of Fluid in a Curved Pipe. *Philosophical Magazine and Journal of Science*, 30(5), pp. 673-695.

[19] Enayet, M. M., Gibson, M. M., Taylor, A. M. K. P., & Yianneskis, M. 1982. Laser-Doppler measurements of laminar and turbulent flow in a pipe bend. *International Journal of Heat and Fluid Flow*, 3(4), pp. 213-219.

[20] Azzola, J., Humphrey, J.A.C., Iacovides, H. and Launder, B.E., 1986. Developing turbulent flow in a U-bend of circular cross-section: measurement and computation. *Journal of Fluids Engineering*, 108, pp. 214-221.

[21] Shiraishi, T., Watakabe, H., Sago, H., Konomura, M., Yamaguchi, A. and Fujii, T., 2006. Resistance and Fluctuating Pressures of a Large Elbow in High Reynolds Numbers. *J. Fluids Eng.*, 128, pp. 1063-1073.

[22] Dutta, P., Saha, S.K., Nandi, N. and Pal, N., 2016. Numerical study on flow separation in 90^0 pipe bend under high Reynolds number by $k-\varepsilon$ modelling. *Eng. Sci. Technol. Int. J.*, 19(2), pp. 904-910.

[23] Dutta, P., & Nandi, N. 2021. Numerical analysis on the development of vortex structure in 90 pipe bend. *Progress in Computational Fluid Dynamics, an International Journal*, 21(5), 261-273.

[24] Dutta, P., Chattopadhyay, H., & Nandi, N. 2022. Numerical Studies on Turbulent Flow Field in a 90 deg Pipe Bend. *Journal of Fluids Engineering*, 144(6), pp. 061104.

[25] Kim, J., Yadav, M. and Kim, S., 2014. Characteristics of Secondary Flow Induced

by 90-Degree Elbow in Turbulent Pipe Flow. *Eng. Appl. Comput. Fluid Mech.*, 8(2), pp. 229-239.

[26] Tanaka, M., Ohshima, H. and Monji, H., 2009. Numerical investigation of flow structure in pipe elbow with large eddy simulation approach. *Proceedings of the ASME 2009 Pressure Vessels and Piping Division Conference PVP2009*, July 26-30, PVP-77598.

[27] Mattingly, C. E. and Yeh, T. T., 1991. Effects of pipe elbows and tube bundles on selected types of flowmeters. *Flow Meas. Instrum.*, 2(1), pp. 4-13

[28] Kinghorn, F. C., McHugh, A. and Dyet, W. D., 1991. The use of etoile flow straighteners with orifice plates in swirling flow. *Flow Meas. Instrum.*, 2(3), pp. 162-168.

[29] Hogendoorn, J., Boer, A. & Laan, D., 2005. Flow disturbances and flow conditioners: The effect on multi-beam ultrasonic flow meters. In 23rd North Sea Flow Metering Workshop 2005, Paper 16, pp. 241-252.

[30] Yehia, A., Khalid, M. S., Hossam, S. A., & Jaafar, M. N., 2009. CFD analysis of incompressible turbulent swirling flow through zanker plate. *Eng. Appl. Comput. Fluid Mech*., 3(4), pp. 562-572.

[31] Hallanger, A., 2002. CFD Analyses of the Influence of Flow Conditioners on Liquid Ultrasonic Flowmetering. *In Osebaerg Sor, a Case Study, North Sea Flow Measurement Workshop (Vol. 1)*.

[32] Jurga, A.P., Janocha, M.J., Yin, G. and Ong, M.C., 2022. Numerical investigations of turbulent flow through a 90-degree pipe bend and honeycomb straightener. (Draft). To be submitted to *J. Offshore Mech. Arct. Eng.*

Chapter 2.

Flow inside piping systems

2.1. Basic principles

A fluid flow inside piping system is classified as being internal as the fluid flows in a confined space rather than over a surface which is external flow [1]. The confining surfaces, in flow through pipes, guide the flow from an arbitrarily defined inlet state to an equally arbitrary outlet state [2]. When the fluid enters one end of a piping system and leaves the other, the difference in pressure between two points occurs which is called the pressure drop. Another important principle in piping networks is the conservation of mass, which says that the total mass at the beginning of the pipe must equal the total mass at the end of the pipe.

When the fluid is completely bounded by solid walls, the fluid flow is affected by the influence of viscosity. Viscosity is responsible for the no-slip condition and development of the boundary layer. The no-slip condition happens when the fluid adheres to the walls and thus it has zero velocity relative to the surface, whereas it moves in the middle of the pipe, known as the freestream flow condition, resulting in the variation of the velocity as a function of the distance from the wall. Consequently, there are large velocity gradients and viscous effects when approaching the wall. This flow region adjacent to the wall is called the boundary layer. Another parameter caused by viscosity is the skin friction drag, which is the tangential shear force exerted by moving fluid on the surface in the flow direction. It is important to mention that when a fluid flows over the curved surface, e.g., through a pipe bend, the boundary layer may detach from the surface which is called the flow separation [1].

The physical description of the flow inside piping systems is associated with the entrance region and the fully developed region. At the entrance region there is a uniform velocity profile which develops fully after some distance from the inlet and becomes as a fully developed velocity profile, as presented in Figure 2.1 (a). It can be observed that there are steep drop-offs next to the wall of the entrance profile. They are due to the lower pressure close to the surface which, according to Bernoulli's equation (described in detail in Section 2.4), implies the higher velocity than toward the centerline, and conversely. Because this effect is slight, it becomes disregarded for most of the engineering applications. On the other hand, at the pipe inlet, viscous shear stress concentrated near the wall, also known as wall shear stress, is the highest which means the boundary layer thickness is the smallest, as shown in Figure 2.1 (b) leftmost. As the flow proceeds down the pipe, the inlet profile develops, and the shear stress decreases. Consequently, the pressure decreases in the flow direction, so the fluid accelerates at the center of the pipe

while it slows down near the wall to remain the same mass flow rate, which is in compliance with the law of conservation of mass. Finally, when a fully developed region is attained, the pressure forces and the shear forces are in balance [3].

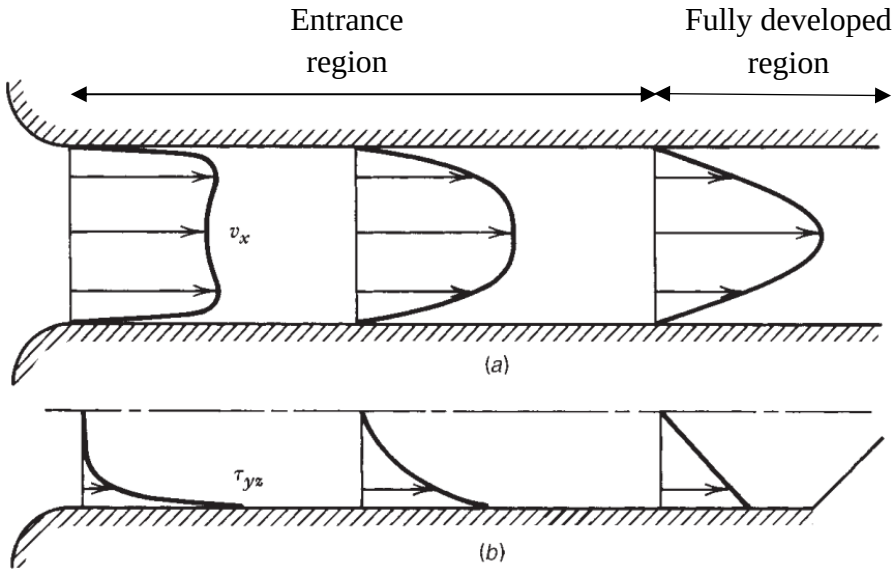

Figure 2.1. The development of the velocity profile (a) and shear stress (b). Reproduced from [3].

2.2. Turbulence

2.2.1. Laminar and turbulent flow

Flow can be divided into two different kinds of flow, laminar and turbulent. The simplest example of the internal flow through a circular pipe is the laminar flow, whereas the turbulent flow is more complex [2], as visualized in Figure 2.3. from experiment of Osborne Reynolds in 1883 [6] who found the existence of transition from laminar to turbulent flow by injecting some dye into to the glass pipe.

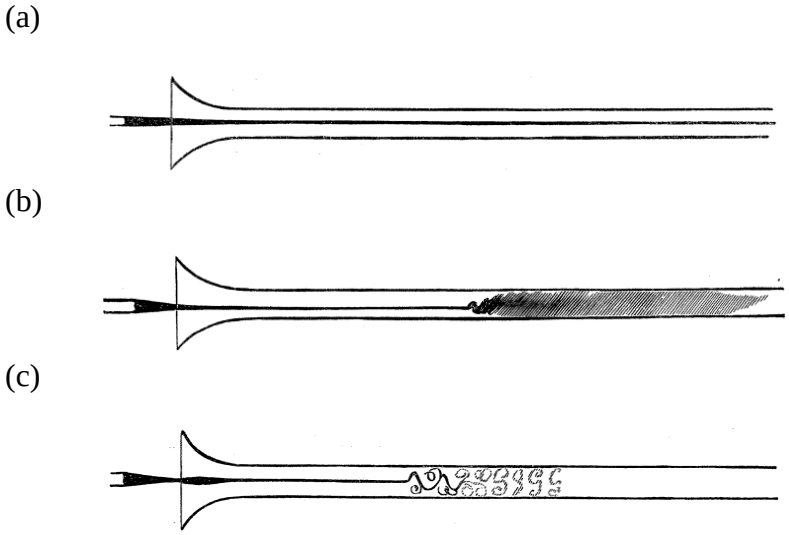

Figure 2.2. Laminar flow (a), transition to turbulent flow and (c) turbulent flow in a pipe. Reproduced from [6].

In Figure 2.32 (a), laminar flow is characterized by smooth layers in the flow stream. The flow in circular pipes has circular layers and the local velocities are parallel to the pipe axis [4]. An example of laminar flow can be oil at low velocities and of high viscosity [1]. In Figure 2.32 (c), turbulent flow is characterized by mixing of the layers observed in laminar flow and the local motions in the fluid are chaotic or highly disordered [4]. An example of turbulent flow can be air at high velocities and of low viscosity [1]. Transitional flow is a flow which is characterized by both laminar and turbulent flow features. The velocity profile of laminar and turbulent flow in a pipe is presented in Figure 2.3. As presented in Figure 2.3, in circular pipes, the velocity profile in laminar flow varies parabolically, from zero at the wall to the maximum at the center. Whereas the axial velocity distribution in turbulent flow is more uniform than in laminar flow. Both flows have zero local velocity at the pipe wall [4].

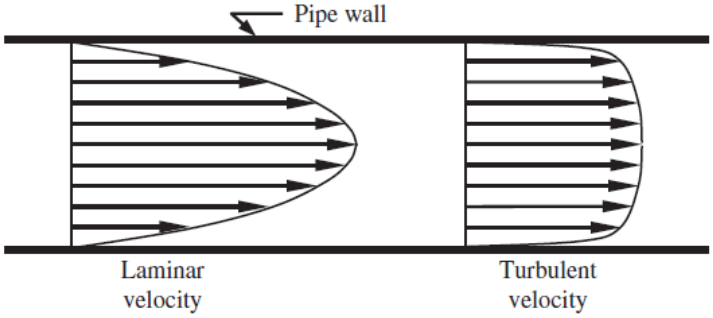

Figure 2.3. Fully developed velocity profiles in a straight pipe. Reproduced from [4].

2.2.2. Reynolds number

The transition from laminar to turbulent flow depends on mainly on geometry, flow velocity and viscosity. In 1883 Osborne Reynolds classified for the first time the state of flow by defining the ratio of inertia forces to viscous forces in the fluid in a circular pipe. It is obvious that when the viscous forces are large enough to dominate, the flow is laminar and when the momentum forces dominate, the viscous flow breaks up and the flow becomes turbulent. The experiments of Osborne Reynolds resulted in the development of the dimensionless parameter, called Reynolds number, Re, that enables to determine the flow regime in pipes [1] and is expressed by Equation 2.1:

$$\mathrm{Re} = \frac{\text{Inertia forces}}{\text{Viscous forces}} = \frac{UD}{\nu} \qquad (2.1)$$

where U is the flow velocity [m/s], D is the characteristic length of the geometry [m], which is the diameter of the pipe in this piping systems and ν is the kinematic viscosity of the fluid $[\mathrm{m}^2/\mathrm{s}]$. The Reynolds number at which the flow becomes turbulent is different for different geometries and flow conditions. For a circular pipe the generally accepted value at which the flow becomes turbulent is 2300 and if Re is less than 2300 the turbulence will not occur in a pipe.

2.2.3. Boundary layer

The velocity boundary layer is a thin region next to the wall of the pipe, where the velocity varies from zero at the wall to 99% of the freestream velocity value. This region determines the flow parameters, such as the velocity profile and the pressure drop which play an important role in study the flow through pipes. Except from the velocity boundary layer, there is also the irrotational flow region, as presented in Figure 2.4. In terms of viscous effects and the velocity gradient, they are significant in the velocity boundary layer and negligible in irrotational flow region.

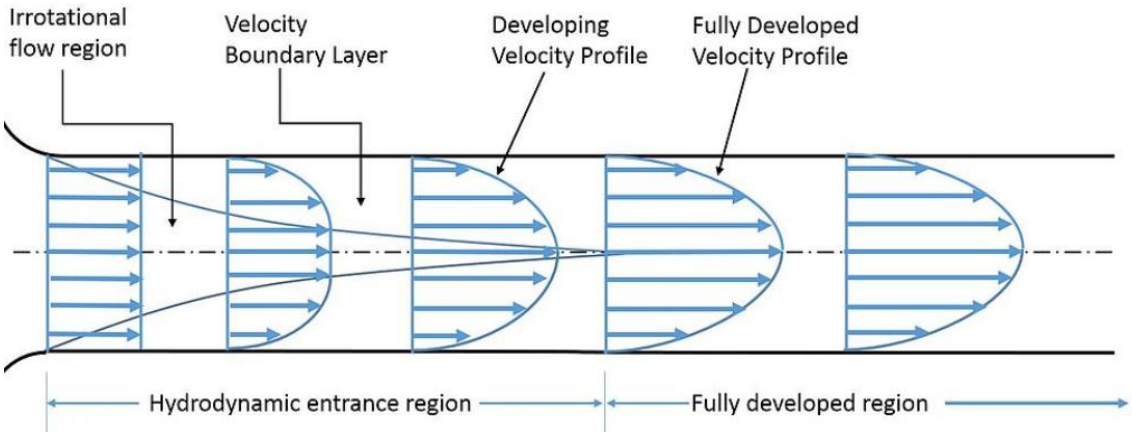

Figure 2.4. The development of the velocity boundary layer. Reproduced from [1].

The inner layer, where the velocity boundary layer is affected by the wall shear stress, is divided into three regions: the viscous sublayer, the buffer layer and the log-law layer, as shown in Figure 2.5. The dimensionless wall units are commonly used to describe the boundary layer topology defined as:

$$u^+ = \frac{U}{u_\tau} \quad (2.2)$$

$$y^+ = \frac{\Delta y u_\tau}{\nu} \quad (2.3)$$

$$u^+ = y^+ \quad (2.4)$$

$$u^+ = \frac{1}{\kappa} \ln (E y^+) \quad (2.5)$$

These regions are characterized by u^+, nondimensional velocity near the wall, and y^+, nondimensional distance between the wall and the first cell, expressed in Equation 2.2 and Equation 2.3, respectively, where u_τ is the wall friction velocity, ν is the fluid kinematic viscosity and Δy is the distance between the wall and the first cell from the wall. The relationship between u^+ and y^+ is given in Equation 2.4 and Equation 2.5, respectively, and forms the law of the wall, which describes the velocity profile of the turbulent flow near the wall. The law of the wall in viscous sublayer shows linear relation in Equation 2.4 and in lag-law layer the logarithmic relation in Equation 2.5 between u^+ and y^+, respectively. The values of constants: κ and E are found from measurements and are applied for all turbulent flows at high Re. On the other hand, for larger values of y^+, the outer layer is characterized by the freestream velocity and the law of the wake which is free from viscous effects [7].

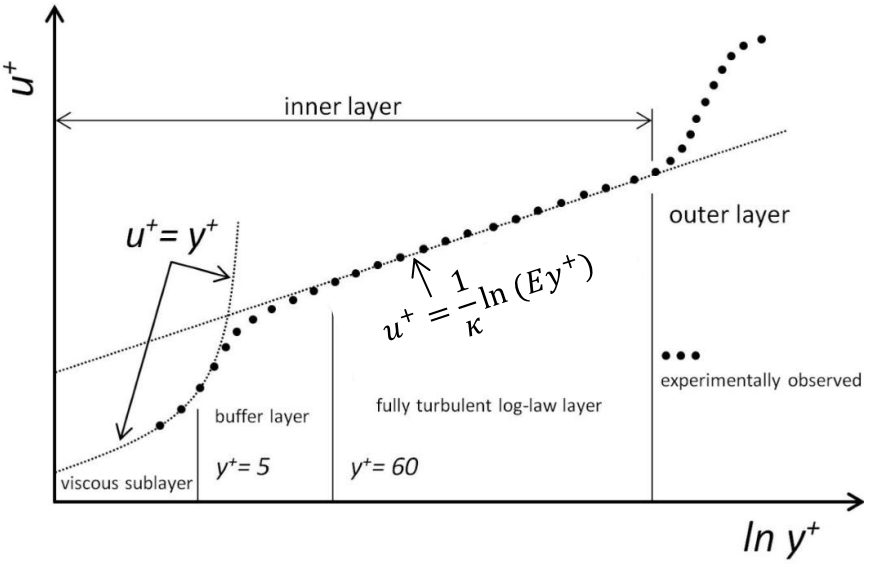

Figure 2.5. The linear and log law of the wall velocity profiles as a function of y^+. Reproduced from [8].

A good agreement of those theoretical equations with experiment data was proved by Schlichting in 1979. Schlichting [9] also discovered that within viscous sublayer ($y^+ < 5$): viscous stresses dominate, in the buffer layer ($5 < y^+ < 70$): viscous and turbulent stresses are similar and in the log-law layer ($y^+ > 70$): turbulent (Reynolds) stresses dominate.

2.3. Flow through pipe bends

The most important geometric parameters of pipe bends are the deflection angle α and the curvature ratio, defined as the curvature radius to pipe diameter ratio, Rc/D. When the flow goes through the bend curvature, flow separation regions and secondary flows occur, as presented in Figure 2.6.

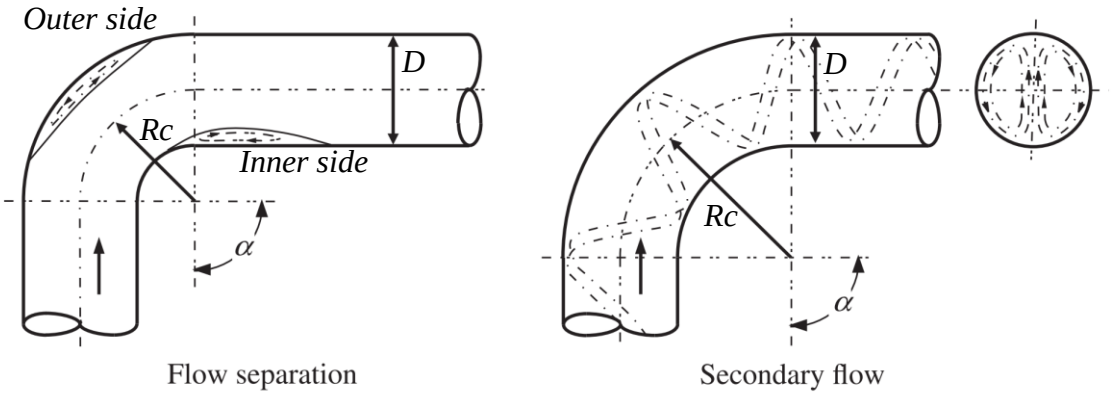

Figure 2.6. The flow through a pipe bend. Reproduced from [4].

The flow separation regions are caused by the separation of the main flow from the inner side right behind the bend and outer side in the bend. On the other hand, the secondary flow is caused by the centrifugal force and frictional effects of the pipe walls and is a function of deflection angle, α, and surface friction. Those three mentioned components, surface friction, flow separation and secondary flow are responsible for the pressure loss in pipe bends.

In the study of flow in curved pipes, the Dean number has been employed. The Dean number is a dimensionless number that has been introduced by Dean [10], [11] to describe the velocity profile in curved pipes which is expressed by the Equation 2.6:

$$De = Re\sqrt{\frac{R}{Rc}} \qquad (2.6)$$

where De is the Dean number, R is the pipe radius and Rc is the curvature radius. In other words, the Dean number represents the ratio of the viscous force acting on a fluid in a pipe bend to the centrifugal force [4].

Nonuniformities in a flow behavior caused by the bend curvature may cause significant flow meter errors. Therefore, the study of potential sources of disturbances, such as pipe bends, is essential in many industrial applications to overcome pressure losses.

2.4. Orifice flowmeter

Orifice plates are flowmeters used for measurement and control of a fluid flow in a pipe. The orifice flowmeter is a flat plate with a circular hole in the middle inserted in the pipe. Flow through an orifice plate is illustrated in Figure 2.7. When the fluid flows in the pipe, it contracts due to the sudden change of the cross-sectional area created by this circular hole. The flow accelerates because of the mass conservation and the pressure drops in the downstream side of the orifice. So, there is high pressure in the upstream and low pressure in the downstream side of the orifice. Orifice flowmeters are often called differential pressure devices as the principle of measurement is based on the differential pressure and Bernoulli's equation presented in Equation 2.8.

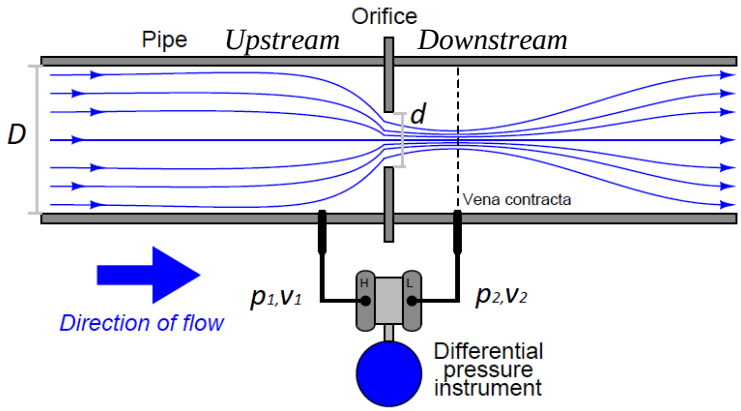

Figure 2.7. The flow through an orifice. Reproduced from [5].

Equation 2.7 is the formula of the flow rate based on the law of conservation of mass, where $\dot{V}$ [m^3/s] is the flow rate, A_1, A_2 are the cross-section areas of the pipe and orifice, respectively, and V_1, V_2 [m/s] is the speed of the fluid in the upstream and downstream side of the orifice, respectively. Equation 2.8 shows Bernoulli's equation for a horizontal flow, where ρ [kg/m^3] is the density of the fluid and p_1, p_2 [Pa] is the pressure at the chosen point in the upstream and downstream side of the orifice, respectively.

$$\dot{V} = A_1 V_1 = A_2 V_2 \;\rightarrow\; V_1 = \frac{A_2}{A_1} V_2 \;\rightarrow\; V_1 = \left(\frac{d}{D}\right)^2 V_2 \qquad (2.7)$$

$$\frac{V_1^2}{2} + \frac{p_1}{\rho} = \frac{V_2^2}{2} + \frac{p_2}{\rho} \qquad (2.8)$$

$$V_2 = \sqrt{\frac{2(p_1 - p_2)}{\rho(1-\beta^4)}} \qquad (2.9)$$

The pressure difference is measured between the upstream and downstream side of the orifice and the flow rate behind the orifice is obtained from Bernoulli's equation by combining Equation 2.7 and Equation 2.8 into Equation 2.9, where β is the ratio between the orifice diameter and the pipe diameter, $\beta = d/D$. However, the Equation 2.9. assumes no loss which in reality exists due to frictional effects and vena contracta area. Vena contracta area, as per Figure 2.7, appears because the flow after passing through the orifice continuously contracts. As a result, the flow rate obtained from Bernoulli's equation is less and thus, different from the actual flow rate so it needs to be corrected with the discharge coefficient, C_d. The value of C_d, which is less than 1 and determined experimentally, is a function of β and Re: $C_d = C_d(\beta,\text{Re})$. Finally, the flow rate for the orifice meters is expressed as Equation 2.10 [1].

$$\dot{V} = C_d A_2 \sqrt{\frac{2(p_1 - p_2)}{\rho(1-\beta^4)}} \qquad (2.10)$$

2.5. Flow conditioning

Flow conditioners homogenize velocity profile in a pipe flow that is disturbed by an upstream installation [14]. Examples of the flow straighteners and flow conditioners given by Annex C of ISO 5167-1 [12] are presented in Figure 2.8.

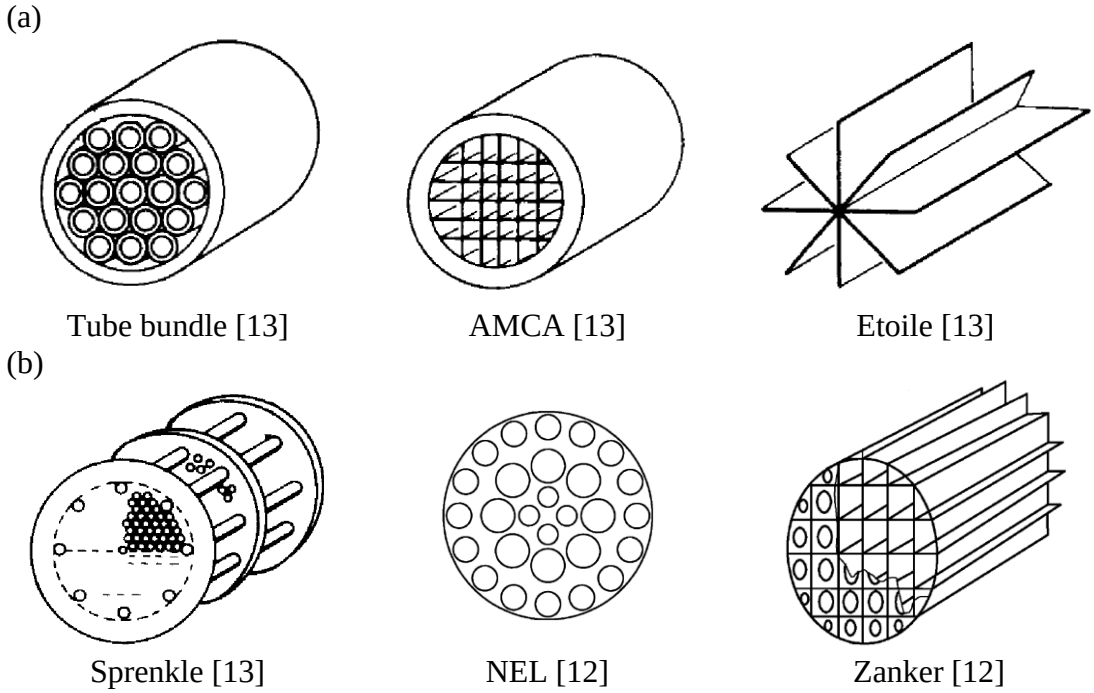

Figure 2.8. Examples of the (a) flow straighteners and (b) flow conditioners according to Annex C of ISO 5167-1. Reproduced from [12] and [13].

The choice of a conditioner depends on the behaviour of the distorted turbulent flow which has to be improved and on the pressure loss which can be allowable based on sizes

and quantity of bores. Flow conditioner may consist of a thin perforated plate, or a passage of ducts laid along the streamwise direction. The cross section of the holes can be of square, circular or regular hexagonal shape. The goal of the various geometries is to break down the swirl and attenuate nonuniformities of the velocity profile in the most effective way. Thus, the swirl and velocity profile are the main parameters to assess the performance of the flow conditioner. Further improve the flow quality by more and more efficient conditioners designs is crucial in modern day piping systems and should be continuously developed to optimize the measurement performance.

References

[1] Cengel, Y.A. and Cimbala, J.M., 2014. *Fluid Mechanics Fundamentals and Applications, Third Edition*. (New York: McGraw-Hill), pp. 1031.

[2] Johnston, J.P., 1975. Internal flows. In Turbulence (pp. 109-169). Springer, Berlin, Heidelberg.

[3] Panton, R.L., 2013. *Incompressible flow*. John Wiley & Sons.

[4] Rennels, D.C. & Hudson, H.M., 2012. *Pipe flow: A practical and comprehensive guide.* John Wiley & Sons.

[5] Facts About Orifice Flow Meters, https://instrumentationtools.com/facts-about-orifice-flow-meters/ (Accessed 13 June 2022).

[6] Reynolds, O., 1883. XXIX. An experimental investigation of the circumstances which determine whether the motion of water shall be direct or sinuous, and of the law of resistance in parallel channels. *Philosophical Transactions of the Royal* society of London, (174), pp. 935-982.

[7] Versteeg, H.K. and Malalasekera, W., 2007. *An introduction to computational fluid dynamics: the finite volume method*. Pearson education.

[8] ANSYS, I., 2011. *ANSYS FLUENT user's guide*. Canonsburg, PA, pp. 15317.

[9] Schlichting, H., 1979. *Boundary-Layer Theory, 7th edn*. McGraw-Hill.

[10] Dean, W.R., 1927. Note on the Motion of Fluid in a Curved Pipe. *Philosophical Magazine and Journal of Science*, 20(4), pp. 208-223.

[11] Dean, W.R., 1928. The Stream-line Motion of Fluid in a Curved Pipe. *Philosophical Magazine and Journal of Science*, 30(5), pp. 673-695.

[12] ISO 5167-1:2003 Measurement of fluid flow by means of pressure differential devices inserted in circular cross-section conduits running full — Part 1: General principle and requirements.

[13] Miller, R. W., 1996. *Flow Measurement Engineering Handbook, 3rd edition*. McGraw-Hill.

[14] Merzkirch, W., Gersten, K., Hans, V., Lavante, E., Peters, F., & Ram, V.V., 2005. *Fluid mechanics of flow metering* Berlin, Springer, pp. 95-110

Chapter 3.

Validation and assessment of different RANS turbulence models for simulating turbulent flow through an orifice plate

Agata Patrycja Jurga [a], Marek Jan Janocha [a], Guang Yin [a], Knut Erik Giljarhus [a], Muk Chen Ong [a]

[a] Department of Mechanical and Structural Engineering and Materials Science, University of Stavanger, Stavanger, Norway.

Published as:

Jurga, A.P., Janocha, M.J., Yin, G., Giljarhus, K.E.T. and Ong, M.C., 2021. Validation and assessment of different RANS turbulence models for simulating turbulent flow through an orifice plate. In IOP Conference Series: Material Science Engineering, 1201:012019.

Abstract

In the present study, numerical simulations using different Reynolds-Averaged Navier–Stokes (RANS) turbulence models are carried out to investigate the turbulent flow through the orifice plate at Reynolds number (Re) of 23000. The orifice thickness to pipe diameter ratio (t) and the orifice diameter to pipe diameter ratio (β) are fixed and equal to 0.1 and 0.5, respectively. The objective is to evaluate the behavior of various RANS models with respect to the relevant flow parameters such as the pressure drop, velocity distributions and turbulence intensity profiles in the pipe by comparing the results with available published experimental data. The following turbulence models are studied: the $k-\varepsilon$, the $k-\varepsilon$ Low Re, the $k-\varepsilon$ RNG, the $k-\varepsilon$ Realizable, the $k-\omega$ SST, the γ – SST, the EARSM and the $k-\varepsilon$ Cubic models. It is found that based on the validation study of the flow through the orifice plate, the following models are in good agreement with experimental measurements: the $k-\omega$ SST, the γ – SST and the EARSM. They show a better performance than the $k-\varepsilon$ model family in predicting the flow features which are important for the orifice flowmeter design.

3.1. Introduction

Orifice plates next to venturi tubes and flow nozzles are among the most popular devices used for measurement and control of a fluid flow in a pipe. They are also frequently called differential pressure flowmeters as the principle of measurement is based on the differential pressure. In the orifice flowmeter, the differential pressure is created when the fluid flows through an artificial restriction (an orifice plate) placed in the cross section of the pipe, resulting in increased fluid velocity and, consequently, decreased pressure after passing the orifice plate. As per Section 4 of ISO 5167-2:2003 [2], the presence of the orifice plate causes a static pressure difference between the upstream (the high pressure) and the downstream (the low pressure) sides of the plate.

The pressure drop is measured at the wall pressure tappings, one on the upstream side and the other on the downstream side of the orifice plate located in a straight pipe [3]. Thus, the fluid flow in the pipe can be described using the Bernoulli's equation which allows calculating the flow rate through a pipe by using the measured differential pressure across the orifice. To get the actual velocity of the fluid, it is important to note that there are pressure losses due to frictional effects and due to the presence of the vena contracta area. To take into account both sources of pressure losses and calculate the real flow rate, the velocity behind the orifice is reduced by the discharge coefficient C_d (defined as the ratio between the actual and theoretical flowrate) which takes values smaller than 1 and is determined experimentally. The value of C_d depends on $\beta = d/D$ (where d is the orifice diameter and D is the pipe diameter) and the Reynolds number ($Re = UD/\nu$, where U is the flow velocity and ν is the kinematic viscosity of the fluid) [1]. ISO 5167-2:2003 [2] refers to the standard orifice plate as shown in Figure 3.1, where it is stated that the diameter d shall, in all cases, be ≥ 12.5 mm and the diameter ratio $\beta = d/D$ shall always be ≥ 0.10 and ≤ 0.75 [2].

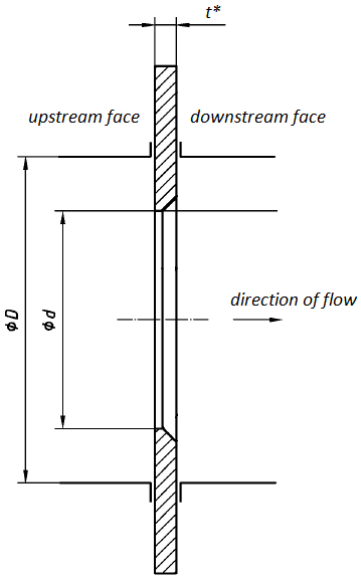

Figure 3.1. The cross-section of a standard orifice plate. Based on [2].

Although there are numerous investigators that have studied orifice flowmeters for different range of Reynolds numbers, the orifice thickness t^* and the orifice diameter to pipe diameter ratio β, for both laminar and turbulent flows, there are few numerical studies comparing the performance of different turbulence models for predicting the flow inside a pipe with an orifice flowmeter. This study is conducted to evaluate the performance of different RANS turbulence models by investigating flow characteristics through the orifice plate inserted in a straight pipe using series of Computational Fluid Dynamics (CFD) simulations. The simulations are carried out for the turbulent flow at Re = 23000 keeping the values of β and t ($t = t^*/D$) fixed.

3.2. Mathematical formulation and numerical method

3.2.1. Flow model

The present numerical models are solving three-dimensional steady Reynolds-averaged Navier-Stokes (RANS) equations of continuity and momentum as follows:

$$\frac{\partial u_i}{\partial x_i} = 0 \tag{3.1}$$

$$u_j \frac{\partial u_i}{\partial x_j} = -\frac{1}{\rho}\frac{\partial p}{\partial x_i} + \frac{\partial}{\partial x_j}\left[(v + v_T)\left(\frac{\partial u_i}{\partial x_j} + \frac{\partial u_j}{\partial x_i}\right)\right] \tag{3.2}$$

where i, j = 1, 2, 3 and x_i, x_j are coordinates of a Cartesian coordinate system, u_i is the time-averaged velocity components (u, v, w), p is the time-averaged pressure, ρ is the density of the fluid, v is the molecular viscosity and v_T is the turbulent eddy viscosity. Based on the Boussinesq assumption, the turbulent eddy viscosity describes the momentum transport caused by turbulent eddies as an analogy to the molecular viscosity. The Boussinesq assumption states that the Reynolds stress tensor ($\tau_{ij} = -\rho\overline{u_i' \; u_j'}$) is proportional to the trace-less mean strain rate tensor, as in Equation (3.3), where $\overline{u_i' u_j'}$ is the time-average of the product of the fluctuating velocity components u_i' and u_j', k is the turbulence kinetic energy ($k = \overline{u_i' u_i'}/2$), δ_{ij} is the Kronecker delta.

$$\tau_{ij} = -\rho\overline{u_i' u_j'} = \rho v_T\left(\frac{\partial u_i}{\partial x_j} + \frac{\partial u_j}{\partial x_i}\right) - \frac{2}{3}\rho k \delta_{ij} \tag{3.3}$$

To compute the turbulent flows using the RANS equations, it is necessary to develop turbulence models that resolve the additional unknown Reynolds stresses. A common classification of RANS turbulence models is based on a number of additional transport equations that are solved simultaneously with Equations (3.1) and (3.2). Also, additional boundary conditions must be specified for the turbulence properties at the inlet and the outlet [1]. For example, for the $k - \varepsilon$ model, k and ε need to be specified in addition to the pressure and velocity boundary conditions. Since the appropriate values of these variables (k and ε) are not always known, a more useful option is to specify the

turbulence intensity, I (ratio of the characteristic turbulent eddy velocity to the free-stream velocity) and the turbulent length scale, l (characteristic length scale of the energy contained in turbulent eddies) [1].

In the present study, the following turbulence models are employed and benchmarked: the linear models: the $k-\varepsilon$ [5], the $k-\varepsilon$ Low Re [7], the $k-\varepsilon$ RNG [8], the $k-\varepsilon$ Realizable [9], the $k-\omega$ SST [11], the γ – SST [18] models and the nonlinear explicit models: the EARSM [14] and the $k-\varepsilon$ Cubic [15] models, briefly described as below:

- The standard $k-\varepsilon$ model proposed by Launder and Spalding [5] solves two differential equations for two dependent variables: the turbulence kinetic energy, k [$\mathrm{m}^2/\mathrm{s}^2$] and the rate of dissipation of the turbulence kinetic energy, ε [$\mathrm{m}^2/\mathrm{s}^3$] [5]. The model gives reasonably accurate predictions at high Reynolds numbers in locations far from walls where the first cell lies in the log-law layer and the standard wall function is used. In the log-law layer, the relationship between the mean velocity and the distance from the wall is assumed as $u^+ = (1/\kappa)\ln(Ey^+)$, where u^+ is the mean wall-parallel velocity, $\kappa = 0.4$ is the von Karman's constant, E = 9.8 is the wall roughness parameter and y^+ is defined as $y^+ = (\Delta y u^*)/\nu$, where Δy is the distance from the wall to the cell center of the nearest computational cell and u^* is the friction velocity. When using the wall function, y^+ should be in the range of $30 < y^+ < 300$ to properly model the log-law layer [6].
- The $k-\varepsilon$ Low Re model is obtained by modifying the standard $k-\varepsilon$ turbulence model to take into account near-wall damping effects and the model replaces the dissipation rate with a modified dissipation rate introduced by Launder and Sharma [7]. For the wall-bounded flows, it is concluded that $k-\varepsilon$ Low Re model at low local Reynolds numbers in the near-wall region is more accurate than the standard $k-\varepsilon$ model. It requires near-wall treatment by introducing a wall function that allows the use of a more refined mesh near the wall to be able to capture flow characteristics within the viscous sublayer ($y^+ < 5$).
- The RNG model was developed using a mathematical technique called the renormalisation group (RNG) by Yakhot et al. [8] to renormalize the Navier-Stokes equations and systematically remove the smallest scales of the turbulence to a point where the remaining scales are resolvable with available computer capacities [8]. The model modifies the dissipation rate equation that accounts for the different scales of motions as opposed to the standard $k-\varepsilon$ model where the eddy viscosity is determined from a single turbulence length scale (only at the specified scale).
- The $k-\varepsilon$ Realizable model has been proposed by Shih et al. [9] and consists of a modified dissipation rate equation which is based on the transport equation of the mean-square vorticity fluctuation at high turbulent Reynolds numbers. Shih et al. [9] showed that the $k-\varepsilon$ Realizable model is a significant improvement over the standard $k-\varepsilon$.
- The $k-\omega$ SST model proposed by Menter [11] is a two-equation turbulence closure which combines the $k-\omega$ model in the near-wall regions and the $k-\varepsilon$ model in the

fully turbulent region far from the walls so that the ε-equation is transformed into the ω-equation by substituting $\varepsilon = k\omega$, where ω is the specific turbulence dissipation rate: $\omega = \varepsilon/k$ [s^{-1}]. The turbulent length scale here is defined as $l = \sqrt{k}/\omega$.

- The γ – SST model is a simplified Langtry-Menter 4-equation Transitional SST model [18]. The intermittency function (γ) and the momentum thickness Reynolds number (Re_θ) are coupled with the $k-\omega$ SST model [11]. The γ determines the percentage of time the flow is turbulent by acting on the turbulent kinetic energy transport equation in the SST model. The model is able to predict the laminar-turbulent transition process.
- The Explicit Algebraic Reynolds Stress Models (EARSM) model was developed by Hellsten [13] and Wallin et al. [14]. In contrary to the linear models using the Boussinesq assumption, the EARSM consists of the transport equations for the kinetic energy and an auxiliary quantity for the individual Reynolds stress anisotropies [14].
- The $k-\varepsilon$ Cubic model is a nonlinear two equation model introduced by Lien at el. [15] which allows the turbulence anisotropy to be predicted. However, the way in which the nonlinear model represents the interaction between the turbulence and the streamline curvature may not be adequate across the whole flow domain [15].

3.2.2. Numerical methods

In the present study, an open source finite volume method CFD code OpenFOAM v2012 is used to solve the governing equations of the fluid flow. A steady state solver simpleFoam which employs the Semi-Implicit Method for Pressure Linked Equations (SIMPLE) is used for the pressure-velocity coupling solution. Second order discretization schemes are used for the convective and diffusive terms.

3.3. Computational setup

3.3.1. Computational domain

The computational domain topology for the straight pipe simulations is shown in Figure 3.2. The pipe diameter is set as D = 1m. The distance between the pipe inlet and outlet for the straight pipe is set to $L = 50D$ (Figure 3.2). The computational domain topology for the straight pipe with the orifice plate is shown in Figure 3.3. The pipe diameter is set as D = 1m. The distance between the pipe inlet and the front face of the orifice plate is set to $Lu = 5D$ and the distance between the pipe outlet and the back face of the orifice plate is set to $Ld = 10D$ (Figure 3.3). The cross sections 1 and 2 are the two locations marked in Figure 3.3, where the centerline pressure values are measured to obtain the discharge coefficients and their distances to the front and back face of the orifice plate are the same as in Nitter et al. [16]. The orifice thickness is set to t^* = 0.1m and the orifice to pipe diameter ratio is set to β = 0.5.

The inlet boundary condition for the straight pipe simulations is a uniform flow with (u, v, w) = (1 m/s, 0, 0). The value of k is calculated as $k = 1.5(uI)^2$ where I is the turbulence intensity estimated as $I = 0.16(Re)^{-1/8}$. The inlet values of ε, ω and γ are calculated according to the recommended expressions given in the corresponding reference papers in Section 3.2.1. The pressure is set as a zero normal gradient at the inlet. At the outlet, the three velocity components as well as the variables: k, ε, ω, γ (depending on the model used) are set as the zero normal gradient and the reference pressure is set as zero. The simulated turbulent velocity profile at the outlet of the straight pipe is then used as the inlet boundary condition for the pipe with the orifice plate simulations as shown in Figure 3.4, which is the same approach as the one used by Nitter et al. [16]. The same fully developed inlet velocity profiles are used for the mesh convergence and validation studies. The inlet values of k, ε, ω or γ for the orifice pipe simulations are also imposed by using the fully developed outlet profiles from the precursor simulations of the corresponding straight pipe cases. The pressure is set as the zero normal gradient at the inlet of the pipe with the orifice plate. At the outlet of the pipe with the orifice plate, the boundary conditions are set to be the same as for the outlet of the straight pipe. On the surface of the pipe wall and the orifice plate, a no-slip boundary condition is prescribed with (u, v, w) = (0, 0, 0).

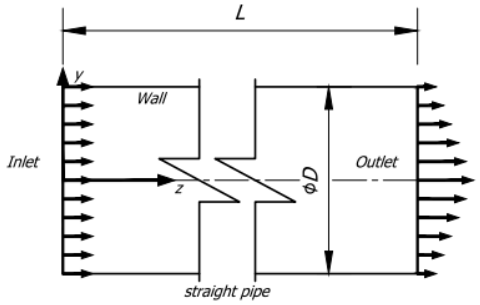

Figure 3.2. The computational domain for the straight pipe simulations[16].

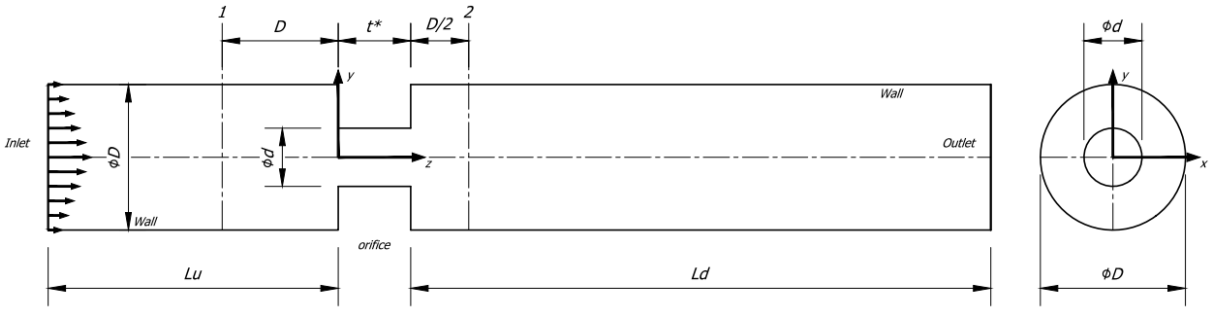

Figure 3.3. The computational domain for the straight pipe with the orifice plate simulations.

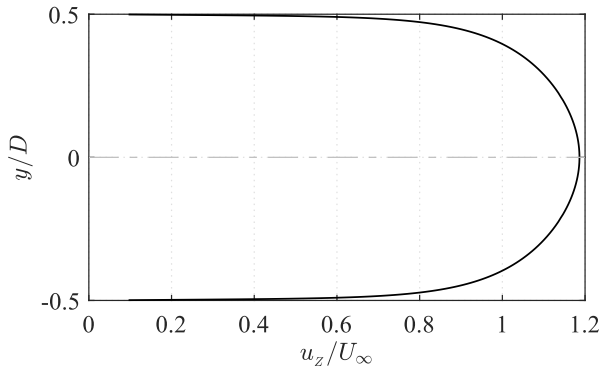

Figure 3.4. An example of the radial profile of the normalised axial velocity upstream of the orifice plate at the inlet (outlet of the straight pipe precursor simulation) applied in the mesh convergence study at Re = 40000 using k − ω model.

3.4. Convergence study

The convergence studies are carried out to determine the required spatial resolution of the computational mesh for the orifice case with $t = 0.25$ ($t = t^*/D$) and $\beta = 0.5$ at $Re = 40000$. A set of three geometrically similar meshes is generated using a constant refinement factor r = 1.25 and presented in Table 3.1. An example of the mesh distribution is shown in Figure 3.5. The mesh is refined close to the walls of the domain to ensure that the $y^+ < 1$. The distributions of the normalized velocity along the centerline in Figure 3.6 and the pressure along the centerline in Figure 3.7 are used to assess the mesh convergence. A good agreement is found between the results obtained on the dense: M2 and very dense: M3 mesh variants, indicating that the M3 can be considered to provide the mesh independent solution of the turbulent flow in the present study.

Table 3.1. Mesh resolutions for convergence study.

Mesh	Number of cells
M1	2703032
M2	5313792
M3	8997648

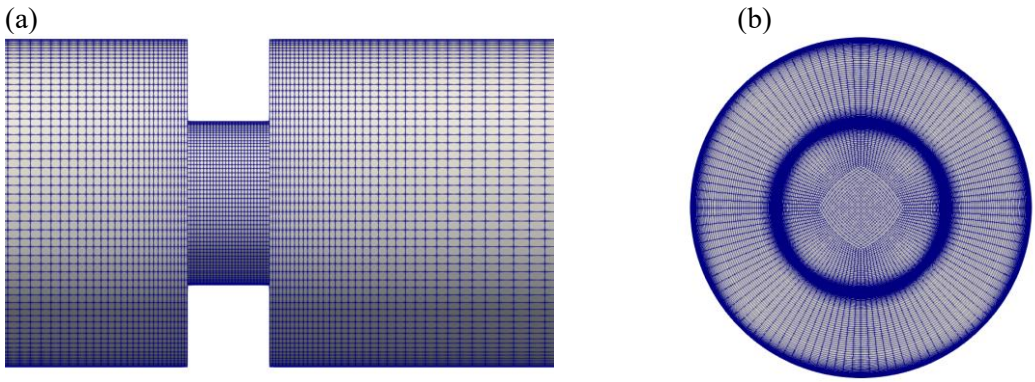

Figure 3.5. An example of the mesh M1 for t = 0.25 and β = 0.5 in (a) the YZ plane and (b) the XY plane.

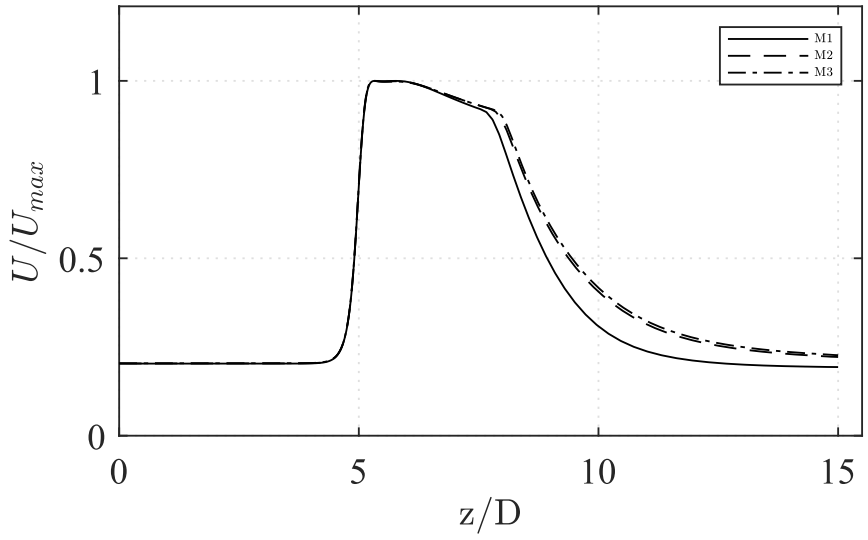

Figure 3.6. The normalised streamwise velocity along the centerline at Re = 40000 with t = 0.25 and β = 0.5 for the investigated mesh density variants: solid: M1, dashed: M2 and dash-dotted: M3.

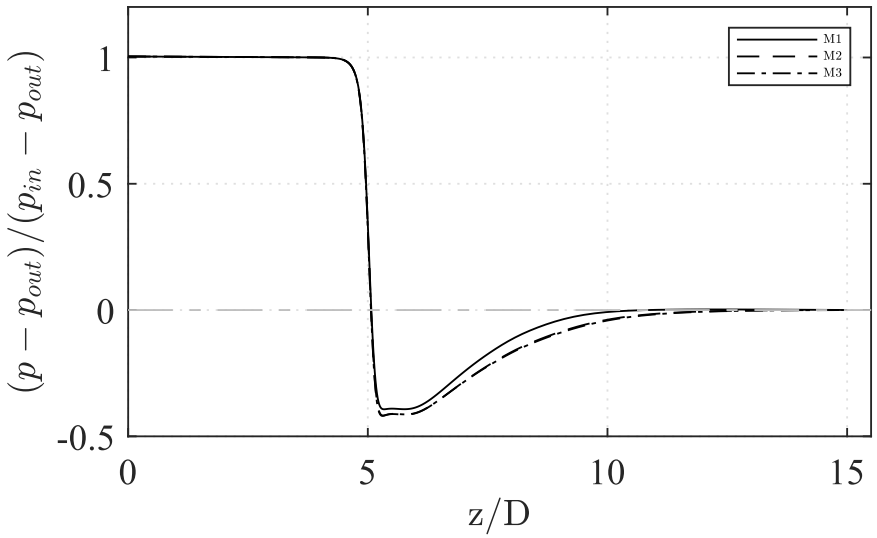

Figure 3.7. The normalised pressure profiles along the centerline at Re = 40000 with t = 0.25 and β = 0.5 for the investigated mesh density variants: solid: M1, dashed: M2 and dash-dotted: M3.

3.5. Results and discussion

A series of numerical simulations using the same grid resolution of the very dense mesh described in Section 3.3.2, is performed using different RANS models briefly described in Section 3.2. In this study, the numerical simulations are carried out at Re = 23000 keeping the value of β and t fixed as follows: β = 0.5 and t = 0.1. The results from the numerical simulations are compared with the experimental data reported by Fiorini [17] and Utanohara et al. [10] for the case of the straight pipe without and with the orifice, respectively. Fiorini [17] conducted the experimental investigation of the turbulent pipe flow at high Reynolds numbers ranging 6500 < Re < 38000. The pressure profiles in Figure 3.8 and the normalized mean velocity profiles in Figure 3.9 for the straight pipe show that the following models: the $k-\omega$ SST, the γ – SST, the EARSM, the $k-\varepsilon$ Cubic and the $k-\varepsilon$ Low Re achieve good agreement with the Fiorini's measurements. However, the $k-\varepsilon$ Cubic and the $k-\varepsilon$ Low Re models do not show good performance when compared to the experimental LDV (Laser Doppler Velocimetry) data published by Utanohara et al. [10] as shown in Figure 3.10 - Figure 3.15. The axial velocity profiles downstream the orifice predicted by the $k-\omega$ SST, the γ – SST and the EARSM models are in good agreement with the experimental results as presented in Figure 3.10, Figure 3.12 and Figure 3.14. Also the shapes of the turbulence intensity profiles predicted by the $k-\omega$ SST, the γ – SST and the EARSM models are qualitatively similar to the shapes of the experimental profiles in Figure 3.11, Figure 3.13 and Figure 3.15. Figure 3.16 shows streamlines plotted on the y-z plane located in the longitudinal axis of symmetry of the pipe with the orifice based on the flow fields predicted by all the investigated turbulence models. The $k-\omega$ SST, the γ – SST, the EARSM, the k-ε RNG,

and the k-ε Realizable show similar size of the recirculation bubble. The recirculation bubble predicted by the $k-\varepsilon$ Low Re, the standard $k-\varepsilon$ and the Cubic $k-\varepsilon$ is significantly smaller than aforementioned models. Thus, it is concluded that there are three models: the $k-\varepsilon$ SST, the γ – SST and the EARSM showing superior performance with respect to simulating the turbulent flow through the straight pipe and through the orifice flowmeter.

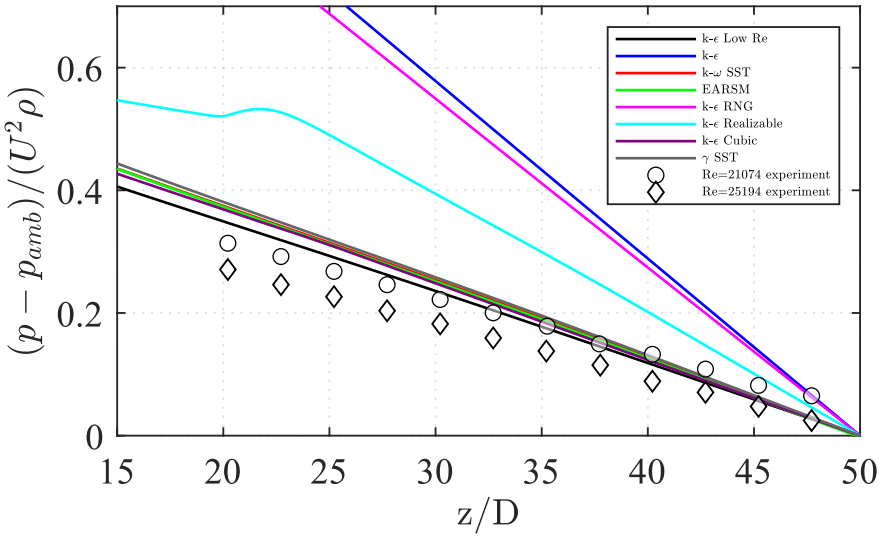

Figure 3.8. The pressure profiles along the centerline at Re = 23000 compared with the experimental data reported by Fiorini [17] between Re = 21074 and Re = 25194 for different turbulence models in the straight pipe.

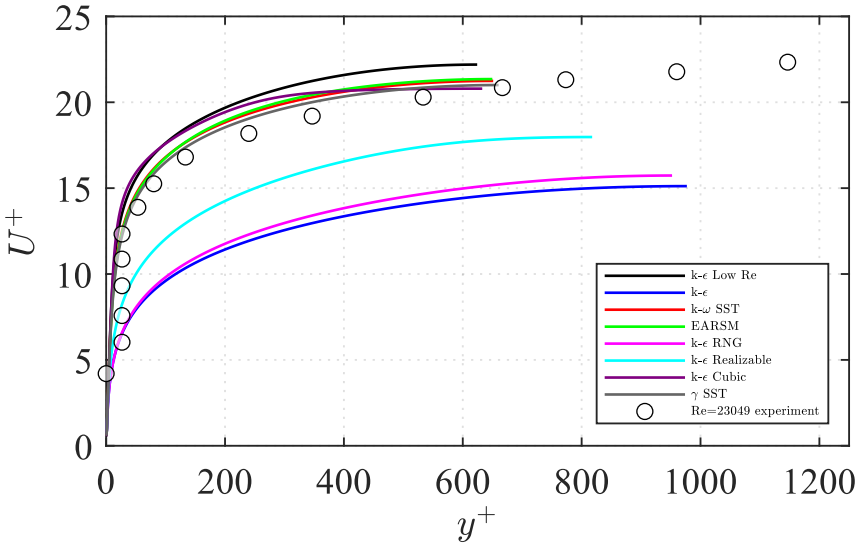

Figure 3.9. The normalized mean velocity profiles at Re = 23000 compared with the experimental data reported by Fiorini [17] for Re = 23049 for different turbulence models in the straight pipe.

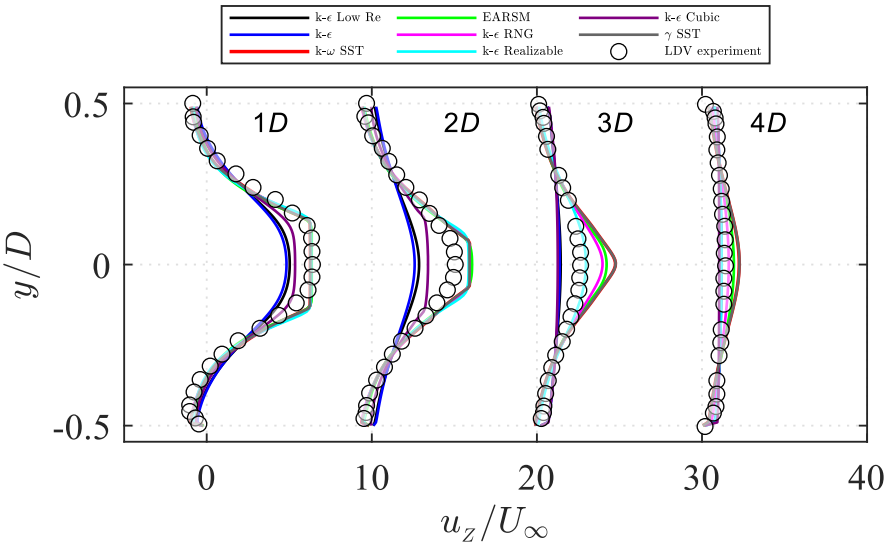

Figure 3.10. The axial velocity profiles at the distance z = 1D, 2D, 3D and 4D downstream from the orifice at Re = 23000 at scale 0 - 10 for each z/D (only the first set of lines conforms to the scale and subsequent sets are offset by u_z/U_∞ = 10 from each other).

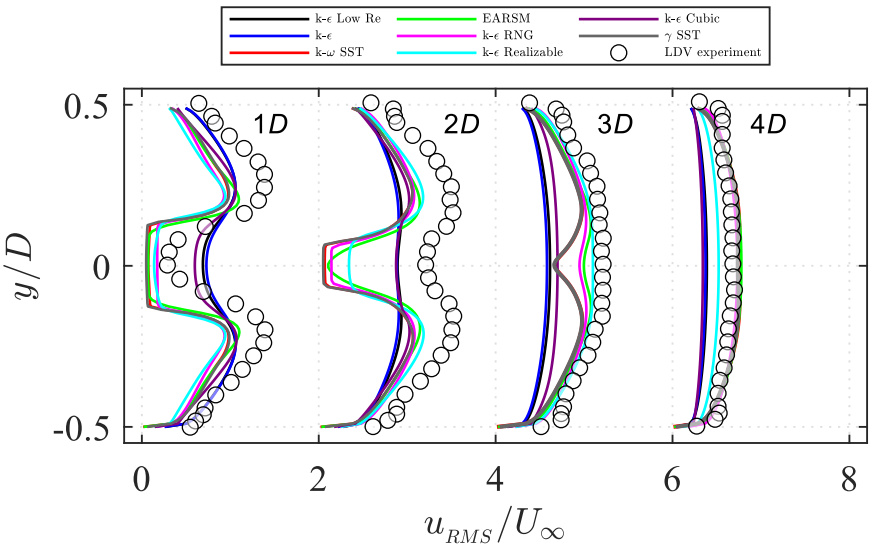

Figure 3.11. The turbulence intensity profiles at the distance z = 1D, 2D, 3D and 4D downstream from the orifice at Re = 23000 at scale 0 - 2 for each z/D (only the first set of lines conforms to the scale and subsequent sets are offset by u_{RMS}/U_∞ = 2 from each other).

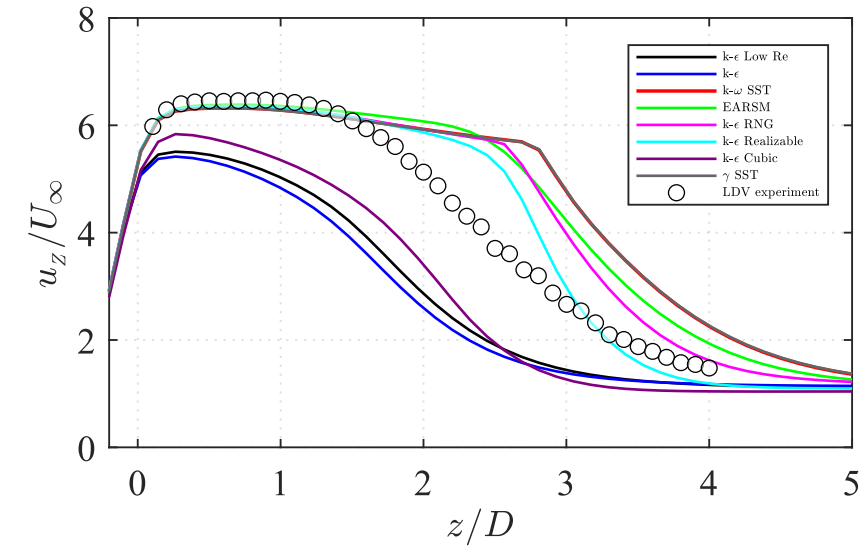

Figure 3.12. The axial velocity profiles along the centerline downstream from the orifice at Re = 23000.

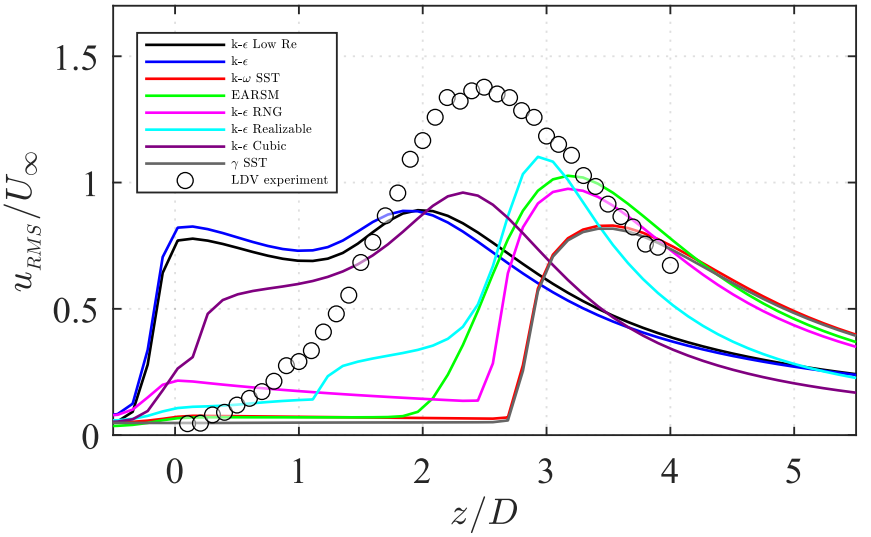

Figure 3.13. The turbulence intensity profiles along the centerline downstream from the orifice at Re = 23000.

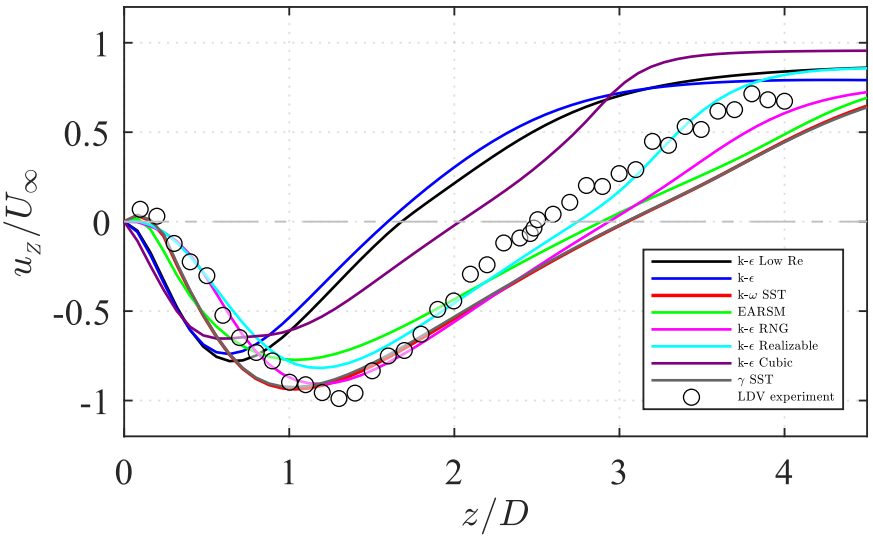

Figure 3.14. The axial velocity profiles near the wall (y = 1 mm from the wall) downstream from the orifice at Re = 23000.

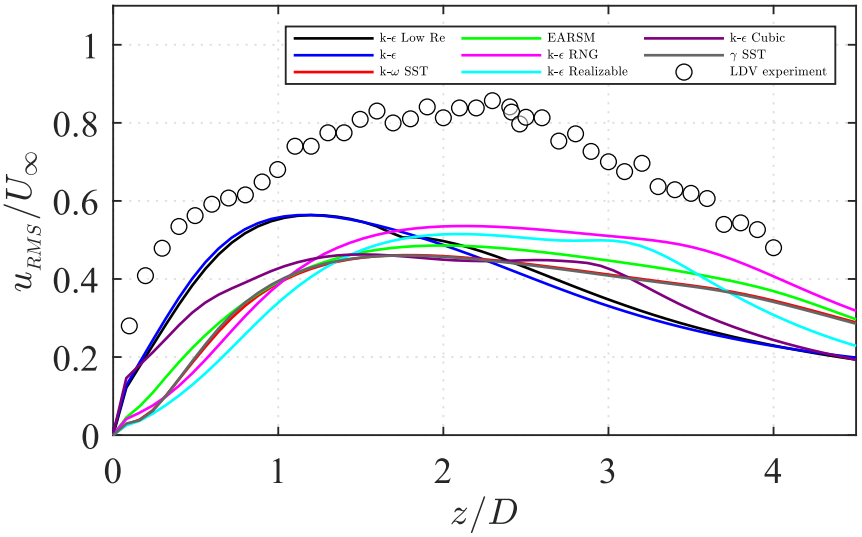

Figure 3.15. The turbulence intensity profiles near the wall (y = 1 mm from the wall) downstream from the orifice at Re = 23000.

(a)

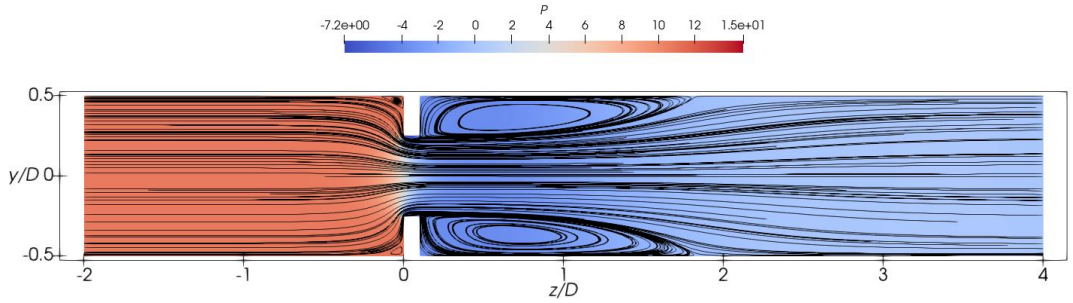

(b)

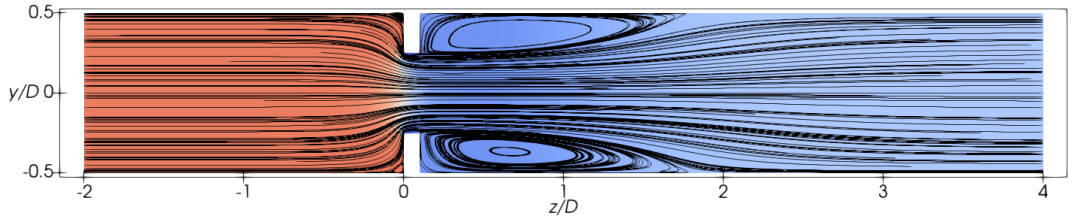

(c)

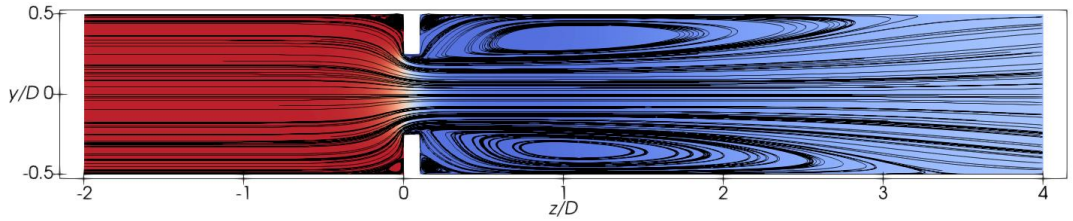

(d)

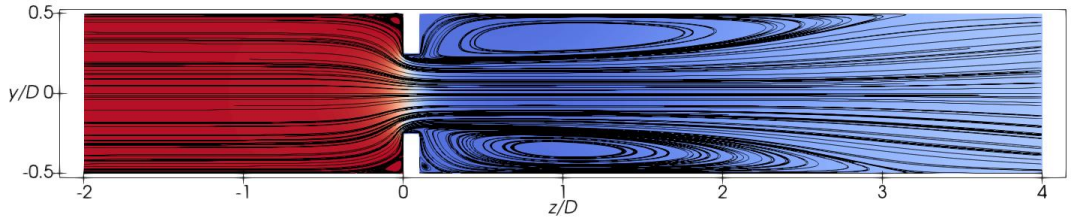

Figure 3.16. The separation flow regions predicted by (a) the $k-\varepsilon$ Low Re, (b) the $k-\varepsilon$, (c) the $k-\omega$ SST, (d) the EARSM, (e) the $k-\varepsilon$ RNG, (f) the $k-\varepsilon$ Realizable, (g) the $k-\varepsilon$ Cubic and (h) the γ – SST. Part 1.

(e)

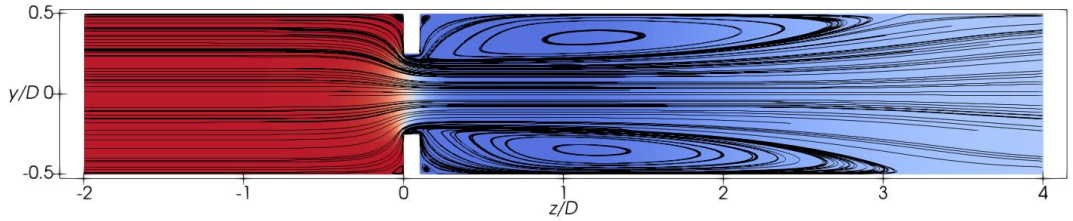

(f)

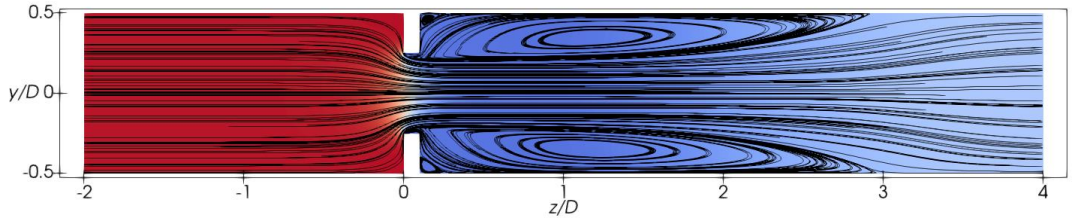

(g)

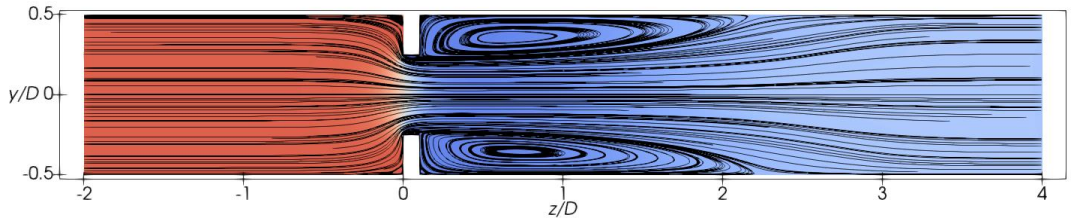

(h)

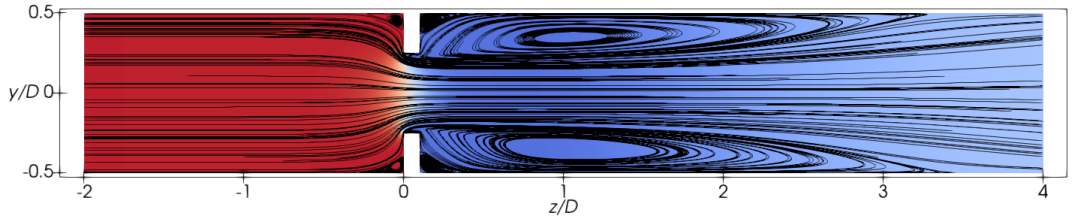

Figure 3.16. The separation flow regions predicted by (a) the $k-\varepsilon$ Low Re, (b) the $k-\varepsilon$, (c) the $k-\omega$ SST, (d) the EARSM, (e) the $k-\varepsilon$ RNG, (f) the $k-\varepsilon$ Realizable, (g) the $k-\varepsilon$ Cubic and (h) the γ – SST. Part 2.

The value of the discharge coefficient (C_d) given by Equation (3.4) is calculated in the same way as given by Nitter et al. [16], where $\Delta P^* = \Delta P/\rho U^2$ is the non-dimensional pressure drop, ΔP is the difference of the pressure value between the cross sections 1 and 2 as shown in Figure 3.3, U is the inlet mean velocity (1m/s) and ρ is the density of the fluid (for the incompressible flow: ρ = 1kg/m^3). The highest predicted value of the

discharge coefficient, as shown in Table 3.2, is given by the $k-\varepsilon$, the $k-\varepsilon$ LS and the $k-\varepsilon$ Cubic models, which is related to the lower predicted pressure differences compared to those predicted by the $k-\omega$ SST, the EARSM, the $k-\varepsilon$ RNG, the $k-\varepsilon$ Realizable and the γ – SST models, where there is no significant variation between the predicted discharge coefficients. According to Table A.2 of Annex A from ISO 5167-2:2003 [2] the discharge coefficient for the orifice with *D* and *D/2* tappings as a function of β, Re and $D \geq 71.12$ mm is given as approximately 0.61 which is very close to the one obtained using the EARSM turbulence model. The percentage error between the C_d = 0.6164 from the numerical simulation with the EARSM model and the one given by ISO is approximately 1 %.

$$C_d = \frac{1}{\sqrt{2}}\left(\frac{1}{\beta}\right)^2 \sqrt{1-\beta^4}\,\frac{1}{\sqrt{\Delta P^*}} \tag{3.4}$$

Table 3.2. Discharge coefficient C_d for Re = 23000 (t = 0.1, β = 0.5).

Turbulence model	C_d [-]
$k-\varepsilon$ LS	0.7260
$k-\varepsilon$	0.7382
$k-\omega$ SST	0.6244
EARSM	0.6164
$k-\varepsilon$ RNG	0.6242
$k-\varepsilon$ Realisable	0.6230
$k-\varepsilon$ Cubic	0.6886
γ – SST	0.6243

3.6. Conclusion

In the present study, the CFD simulations are performed to investigate the flow behavior through the orifice plate using different turbulence models. The numerical study is based on RANS equations for the turbulent flow at Reynolds number of 23000. Eight different RANS turbulence models are used to resolve the turbulent stress and their performances are evaluated.

The turbulent flow profiles through the straight pipe are used as the inlet profiles for the orifice in the pipe flow simulations. The simulation set up is based on the experiments on the orifice flow reported by Utanohara et al. [10]. The predicted results show better agreement with the experimental data of the velocity distribution than with the turbulence intensity profiles. The main conclusion based on the present work is that the turbulence models: the $k-\omega$ SST, the γ – SST and the EARSM models produce similar results that are in a fair agreement with the experimental data. Although the turbulence models based on the Boussinesq eddy viscosity assumption are typically used in the flows through

pipes, the EARSM model shows the best performance for simulating the fully developed turbulent flow through the orifice plate as supported by the presented comparisons with the experimental data. The EARSM's assumption of anisotropic Reynolds stress tensor gives superior results in capturing both separation regions of the flow behind the orifice plate as well as predicting the effect of the curvature of the mean flow.

References

[1] Cengel, Y.A. and Cimbala, J.M., 2014. Fluid Mechanics Fundamentals and Applications, Third Edition, (New York: McGraw-Hill) pp. 1031.

[2] ISO 5167-2:2003 Measurement of fluid flow by means of pressure differential devices inserted in circular cross-section conduits running full — Part 2: Orifice plates.

[3] ISO 5167-1:2003 Measurement of fluid flow by means of pressure differential devices inserted in circular cross-section conduits running full — Part 1: General principle and requirements.

[4] Reader-Harris, M., 2015. Orifice Plates and Venturi Tubes (London: Springer).

[5] Launder, B.E. and Spalding, D.B., 1974. The numerical computation of turbulent flows, *Comput. Methods Appl. Mech. Eng.* 3(2), pp. 269–289.

[6] Versteeg, H.K. and Malalasekera, W., 2007. An introduction to computational fluid dynamics: The finite volume method, Second Edition.

[7] Launder, B.E. and Sharma, B.I., 1974. Application of the energy-dissipation model of turbulence to the calculation of flow near a spinning disc, *Lett. Heat Mass Transfer*, Vol. 1, pp. 131–138.

[8] Yakhot, V., Orszag, S.A., Thangam, S. and Speziale, C.G., 1992. Development of Turbulence Models for Shear Flows by a Double Expansion technique, *Phys. Fluids A Fluid Dyn*. 4(7).

[9] Shih, T.H., Liou, W.W., Shabbir, A., Yang, Z. and Zhu, J., 1995. A New k- ε Eddy Viscosity Model For High Reynolds Number Turbulent Flows, *Computers and Fluids*, 24(3), pp. 227–238.

[10] Utanohara, Y., Nagaya, Y. and Nakamura, A., 2012. Influence of Local Field on Flow Accelerated Corrosion Downstream from an Orifice, *J. Power Energy Syst.* Vol. 6, No. 1.

[11] Menter, F.R., 1994. Two-Equation Eddy-Viscosity Turbulence Models for Engineering Applications, *AIAA J*. 32(8), pp. 1598–1605.

[12] Langtry, R.B., 2006. A Correlation-Based Transition Model using Local Variables for Unstructured Parallelized CFD codes, University of Stuttgart, PhD Thesis.

[13] Hellsten, A., 2005. New Advanced k-omega Turbulence Model for High-Lift Aerodynamics," AIAA J. Vol. 43, No. 9, pp. 1857-1869.

[14] Wallin, S. and Johansson, A.V., 2000. An Explicit Algebraic Reynolds Stress

Model for Incompressible and Compressible Turbulent Flows, J. Fluid Mech. Vol. 403, pp. 89-132.

[15] Lien, F.S., Chen, W.L. and Leschziner, M.A., 1996. Low-Reynolds-Number Eddy-Viscosity Modelling Based on Non-Linear Stress-Strain/Vorticity Relations, *Engineering Turbulence Modelling and Experiments 3*, pp. 91–100.

[16] Nitter, B., Yin, G. and Ong, M.C., 2020. Numerical Simulations of Turbulent Flow Through an Orifice Plate in a Pipe, *J. Offshore Mech. Arct. Eng.* Paper No: OMAE-20-1079.

[17] Fiorini, T., 2017. Turbulent Pipe Flow - High Resolution Measurements in CICLoPE, University of Bologna, PhD Thesis.

[18] Langtry, R.B. and Menter, F.R., 2009. Correlation-Based Transition Modeling for Unstructured Parallelized Computational Fluid Dynamics Codes, *AIAA J.* 47(12), pp. 2894-2906.

Chapter 4.

Numerical simulations of turbulent flow through a 90-degree pipe bend

Agata Patrycja Jurga [a], Marek Jan Janocha [a], Guang Yin [a] and Muk Chen Ong [a]

[a] Department of Mechanical and Structural Engineering and Materials Science, University of Stavanger, Stavanger, Norway.

Published as:

Jurga, A.P., Janocha, M.J., Yin, G. and Ong, M.C., 2022. Numerical simulations of turbulent flow through a 90-degree pipe bend. Journal of Offshore Mechanics and Arctic Engineering. (Under review).

Abstract

The turbulent flow through a 90-degree circular pipe bend is investigated by carrying out the numerical simulations using the Reynolds-Averaged Navier–Stokes (RANS) turbulence model in the present study. The objective of the present study is to evaluate the effects of different values of the curvature radius (Rc) and different Reynolds numbers (Re) on the flow development in the circular pipe bend by employing the Explicit Algebraic Reynolds Stress Model (EARSM) to resolve the Reynolds stresses, unlike the research carried out so far where the turbulence anisotropy has not been considered. The curvature ratio defined as the curvature radius to pipe diameter ratio (Rc/D) is varied between 1 and 4 and the investigated Re range is from 10000 to 60000. The numerical model is validated by comparing the axial velocity profiles with the previous published experimental data. It is found that for the fixed Re and decreasing Rc/D, the axial velocity, the velocity perturbation and the pressure difference in the cross section increase and vorticity becomes stronger. When the curvature ratio gets smaller than 2, the flow velocity profile becomes highly distorted. For the fixed Rc/D, the influence of the Re on the flow behavior is small for the investigated range of Re.

4.1. Introduction

Flow in curved pipes is commonly encountered in many industrial applications such as heat exchangers, processing equipment or cooling systems. The curvature of the pipe geometry tends to introduce secondary flows that can lead to non-uniform fluid transfer. The knowledge of the secondary flow motions is important in piping system design in order to overcome curvature-induced pressure losses [1].

Bends are the pipe sections used for changing the direction of the piping system. The main features of the flow through a bend are regions of separated flow and regions of secondary flow developing in the areas shown in Figure 4.1 (a) and (b), respectively. The secondary flow is caused by a transverse pressure gradient at the bend created by the centrifugal force acting on the moving fluid while changing its direction. Due to the higher axial velocity near the center of the pipe, there is a greater pressure near the center of the pipe than near to the wall and it forces the fluid near the center of the pipe to move towards the outer side of the pipe wall and the fluid near the outer wall moves inwards, which results in the secondary flow. On the other hand, the flow separation regions are caused by the adverse pressure gradient near the outer side in the bend and near the inner side right behind the bend. Both the secondary flow and the flow separation as well as frictional effects along the pipe bend lead to the pressure losses [2].

A comprehensive review of experimental studies on the flow in curved pipes is presented by Berger et al. [1]. The first observation of the secondary flow was made in 1876 by Thomson [3] who investigated an open channel flow where the effects of curvature were most evident. The existence of the secondary flow was investigated later by Williams et al. [4] and Eustice [5]. Williams et al. [4] observed that the location of the maximum axial velocity was moved towards the outer wall of a curved pipe section and Eustice [5] proved the existence of the secondary flow by injecting dye into water flowing through a coiled pipe. However, the first mathematical derivation of a function describing the velocity profile for fully developed flow in curved pipes has been carried out by Dean [6] [7]. Dean formulated a mathematical solution for the secondary flow governed by the dimensionless parameter called Dean number which is proportional to the Reynolds number and the square root of the pipe-to-curvature radius ratio. Weske [8] investigated experimentally the velocity distributions at the outlet of elbows of different cross-sectional shapes at Reynolds numbers (Re) from 2×10^5 to 6×10^5 using Pitot tubes and hot-wire probe. The results indicated that the cross-sectional shape had minor influence on the velocity pattern compared with the curvature radius (Rc). It was found that the occurrence of the backflow and significant distortion of the velocity profile were observed for Rc/D smaller than 1.5. It was also found that the swirling motion persisted downstream of the bends for smaller curvature radii and the variation of Re had no appreciable effect upon the velocity distribution. Enayet et al. [9] performed LDV (Laser Doppler Velocimetry) measurements of the longitudinal velocity for laminar and turbulent flow in a 90-degree pipe bend. Azzola et al. [10] also used LDV to obtain the

longitudinal and circumferential velocity components in a 180-degree pipe bend. Sudo et al. [11] extended their work by investigating the three components of mean flow and the Reynolds stresses of the turbulent flow in a 90-degree pipe bend. Shiraishi et al. [12] investigated flow through a pipe elbow at Reynolds number up to 8.0×10^6 using LDV. It was founded that the overall flow pattern was independent of the Reynolds number and the fluctuating pressure on the pipe wall was dominant in the regions of flow separation and reattachment. The transition between two secondary motions of swirl switching motion and the Dean motion was studied by Hellström et al. [13] using the time-resolved stereoscopic PIV.

In addition to experiments, numerical simulations are frequently employed to study the flow inside the curved pipes for different geometry and Reynolds numbers. Patankar et al. [14] performed turbulence modeling using the $k-\varepsilon$ model to predict the flow behaviors inside a 180-degree pipe bend and a satisfactory agreement with the experimental data was achieved. Masud et al. [15] performed numerical study using Computational Fluid Dynamics (CFD) simulations of a steady, incompressible, viscous flow through a curved pipe with the circular cross-section. They found that axial velocity increased with the increase of Dean number and decreased with the increase of curvature. Dutta et al. [16], [17], [18] investigated the influence of Reynolds numbers on the flow separation characteristics and the development of the vortex structures in 90-degree pipe bend using CFD simulations employing the $k-\varepsilon$ turbulence model. The numerical study was conducted at the Reynolds numbers ranging from 1×10^5 to 10×10^5 and the results showed that with the increasing Reynolds number, the starting point of the flow separation moves upstream of the pipe bend and the reattachment point moves downstream of the pipe bend. This behavior of the flow separation could be clearly observed for $Rc/D = 1$, where Rc/D is defined as the curvature ratio, Rc is the pipe bend radius and D is the pipe diameter. It was also found that the flow became very complex and unsteady downstream of the bend due to the flow separation. Kim et al. [19] studied the flow characteristics downstream of a pipe bend using CFD simulations with different turbulence models. They concluded that among the investigated models, the $k-\varepsilon$ RNG (Re-Normalization Group) model gave a good prediction in the swirl intensity of the secondary flow. The investigated radius of the elbow curvature was in the range of $2D$ to $7D$ and it was observed that with the increasing radius, the swirl intensity decayed quicker. It was also recommended to study the non-linear turbulence models for complex swirling flows as a future work. Tanaka et. al. [20] reproduced the behavior of the laminar and turbulent flow through the elbow by employing the Large Eddy Simulation (LES) approach. The LES approach showed good agreement with the experimental data both for laminar flow at Re = 700 reported by Bovendeerd et al. [21] as well as for turbulent flow at Re = 6×10^4 and 6.7×10^6 reported by Sudo [11] and Shiraishi et al. [12], respectively. The evolution of turbulent characteristics at different Reynolds numbers and curvature radii were investigated using direct numerical simulations (DNS) by

Noorani et al. [22] However, the simulations were limited in the moderate Re range (5300 ≤ Re ≤ 11700) due to the high computational amount for DNS.

Although there are many numerical studies on the flow inside the pipe bend, most of them are employing turbulence models based on the Boussinesq eddy viscosity assumption where the turbulence anisotropy is not taken into account. Jurga et al. [23] evaluated the performance of different RANS turbulence models for predicting the turbulent flow through the orifice plate using CFD simulations at Re = 2.3×10^4. They found that the assumption of anisotropic Reynolds stress tensor of the EARSM model gives the best performance for simulating the fully developed turbulent flow in the pipe with an orifice based on the validation study. Due to the best agreement with experimental data by using the EARSM model compared with other turbulence models as reported by Jurga et al. [23], this model is adopted in the present study to simulate the turbulent flow through the pipe bend and thus regarded as the model that can simulate the flow through the pipe bend more accurately than other turbulence models used so far in the published literature. The EARSM turbulence model is used to evaluate the effects of the different pipe bend geometries and Reynolds numbers for the numerical simulations of the turbulent flow. The geometry of the pipe bend is changed by adjusting the curvature ratio, Rc/D between 1 and 4 and the investigated Re range is from 10000 to 60000. The flow parameters investigated in the present study are the axial velocity, the velocity perturbation, the pressure difference and vorticity. The present paper is organized as follows. First, the numerical model is given in Section 4.2. The computational set up, grid resolution studies and the validation studies are given in Section 4.3. The results and discussions of the parametric study are presented in Section 4.4. Finally, conclusions are given.

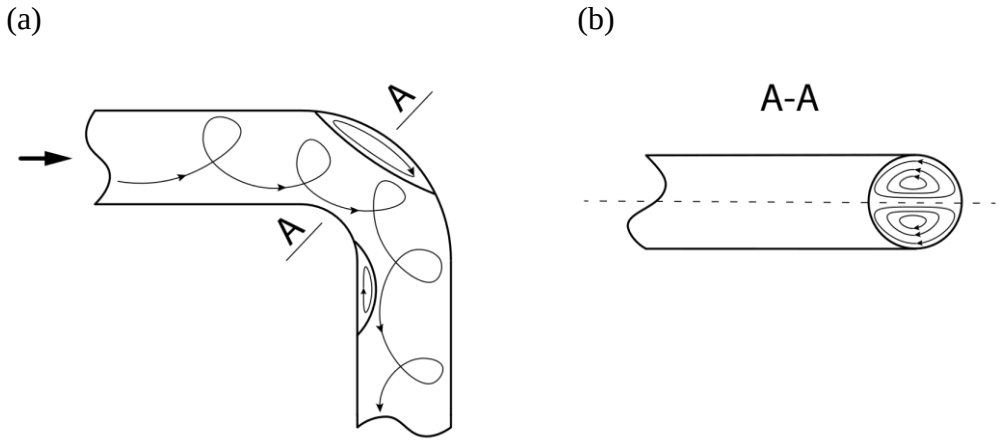

Figure 4.1. Schematic showing (a) separated flow regions and (b) the secondary flow development in the pipe bend. Based on [2].

4.2. Mathematical formulation and numerical method

4.2.1. Flow model

The three-dimensional (3D) steady Reynolds-averaged Navier-Stokes (RANS) equations of continuity and momentum are solved in the present study, which is given as follows:

$$\frac{\partial u_i}{\partial x_i} = 0, \tag{4.1}$$

$$\overline{u_j}\frac{\partial \overline{u_i}}{\partial x_j} = -\frac{1}{\rho}\frac{\partial \bar{p}}{\partial x_i} + \frac{\partial}{\partial x_j}\left(v\frac{\partial \overline{u_i}}{\partial x_j} - \overline{u_i' u_j'}\right), \tag{4.2}$$

where i, j = 1, 2, 3 and x_i, x_j are the coordinates of a Cartesian coordinate system. $\overline{u_i}$ is the time-averaged velocity components as (u, v, w), $\bar{p}$ is the time-averaged pressure, ρ is the density of the fluid and v is the kinematic viscosity of the fluid. $\overline{u_i' u_j'}$ is the Reynolds stress tensor which constitutes the time-average of the product of the fluctuating velocity components u_i' and u_j'. In the present study, the Explicit Algebraic Reynolds Stress Model (EARSM) of turbulence developed by Hellsten [24] and Wallin et al. [25] is employed. Different from the linear models using the Boussinesq assumption, the EARSM includes additional term modelling effects of anisotropy expressed as fully explicit algebraic relation for the Reynolds stress in terms of the mean flow field. The Reynolds stress tensor, τ_{ij}, with anisotropy tensor, a_{ij}, is given in Equation (4.3), where δ_{ij} is the Kronecker delta and k turbulence kinetic energy.

$$\tau_{ij} = \overline{u_i' u_j'} = k\left(a_{ij} + \frac{2}{3}\delta_{ij}\right) \tag{4.3}$$

The anisotropy tensor, a_{ij}, is decomposed into a tensor basis as follows in Equation (4.4):

$$a_{ij} = \beta_1 T_{1,ij} + \beta_2 T_{2,ij} + \beta_3 T_{3,ij} + \beta_4 T_{4,ij} + \beta_6 T_{6,ij} + \beta_9 T_{9,ij} \tag{4.4}$$

where β_i are the coefficients of the tensor basis. The expressions for the tensor $T_{k,ij}$ are given as:

$$T_{1,ij} = S_{ij}, T_{2,ij} = S_{ik}S_{kj} - \frac{II_S\delta_{ij}}{3}, T_{3,ij} = \Omega_{ik}\Omega_{kj} - \frac{II_\Omega\delta_{ij}}{3}, T_{4,ij} = S_{ik}\Omega_{kj} - \Omega_{ik}S_{kj}$$
$$T_{6,ij} = S_{ik}\Omega_{kl}\Omega_{lj} + \Omega_{ik}\Omega_{kl}S_{lj} - \frac{2}{3}IV\delta_{ij} - II_\Omega S_{ij}$$
$$T_{9,ij} = \Omega_{ik}S_{kl}\Omega_{lm}\Omega_{mj} - \Omega_{ik}\Omega_{kl}S_{lm}\Omega_{mj} + \frac{1}{2}II_\Omega\left(S_{ik}\Omega_{kj} - \Omega_{ik}S_{kj}\right) \tag{4.5}$$

The quantities S_{ij} and Ω_{ij} in Equation (4.5) are the nondimensional mean strain and mean rotation tensor, respectively, and II_S, II_Ω and IV are the tensor invariants defined as: $II_S = S_{ij}S_{ji}$, $II_\Omega = \Omega_{ij}\Omega_{ji}$ and $IV = S_{ik}\Omega_{kj}\Omega_{ji}$. A detailed model description can be found in

Hellsten [24]. The derivation of the general EARSM formulation used in Hellsten [24] can be found in Wallin et al. [25].

4.2.2. Numerical methods

In the present study, the open-source finite volume method CFD code OpenFOAM v2012 is used to solve the governing equations of the fluid flow. A steady state solver simpleFoam based on the Semi-Implicit Method for Pressure Linked Equations (SIMPLE) is employed to obtain the pressure-velocity coupling solution. The second order discretization schemes are used to discretize all the convective and diffusive terms.

4.3. Computational setup

4.3.1. Computational domain

In order to obtain appropriate inlet boundary conditions for the pipe bend simulations, precursor simulations of a long and straight pipe are performed. The computational domain for the straight pipe simulations is shown in Figure 4.2. The diameter of the pipe for the straight pipe is set as D = 1m. The distance between the inlet and outlet of the straight pipe is set as $L = 50D$ which is sufficient to form the fully developed turbulent velocity profile. The computational domain for the pipe bend is illustrated in Figure 4.3. The diameter of the pipe bend is set as D = 1m. The distance between the inlet of the pipe and the bend section inlet is set to $Lu = 20D$ and is equal to the distance between the bend section outlet and the pipe outlet which is also set to $Ld = 20D$. The results of convergence study in Section 4.3.2, validation study in Section 4.3.3 and parametric study in Section 4.4 are described referring to the names of the pipe bend planes presented in Figure 4.4.

The inlet boundary condition for the simulations of the straight pipe is a uniform flow with (u, v, w) = (0, 0, 1) [m/s]. The value of k is set as $k = 1.5(UI)^2$, where I is the turbulence intensity estimated as $I = 0.16(Re)^{-1/8}$ and U [m/s] is the flow velocity at inlet. The value of ω is given as $\omega = \sqrt{k}/l$, where l is the turbulent length scale calculated as $l = 0.05D$ [26]. The pressure is set as the zero normal gradient at the inlet. At the outlet, the three velocity components and the variables of k and ω are set as the zero normal gradient. The reference pressure is set as zero. The simulated turbulent velocity profile at Re = 60000 at the outlet of the straight pipe is compared with the experimental data reported by Benjamin et al. [27] at Re = 60000 and Laufer [28] at Re = 50000 in Figure 4.5. The turbulent velocity profile is used as the inlet boundary condition for the simulations of the pipe bend. The same fully developed velocity profile at the inlet is used for the mesh convergence study, validation study and parametric study at Re = 60000. The inlet values of k and ω for the simulations of the pipe bend are also imposed by using the fully developed profiles at the outlet from the precursor simulations of the straight pipe. The pressure is set as the zero normal gradient at the inlet of the pipe

bend. At the outlet of the pipe bend, the same boundary conditions as used at the outlet of the straight pipe are set. On the surface of the walls of the straight pipe and the pipe bend, a no-slip boundary condition is prescribed for the velocity components with (u, v, w) = (0, 0, 0).

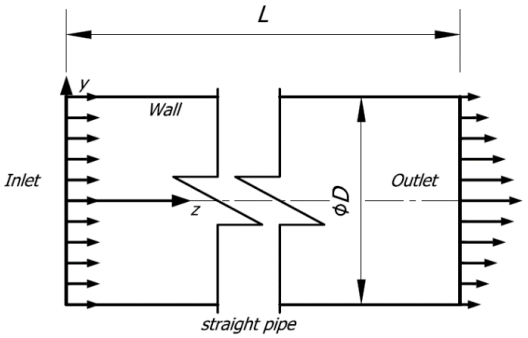

Figure 4.2. The computational domain topology for the simulations of the straight pipe.

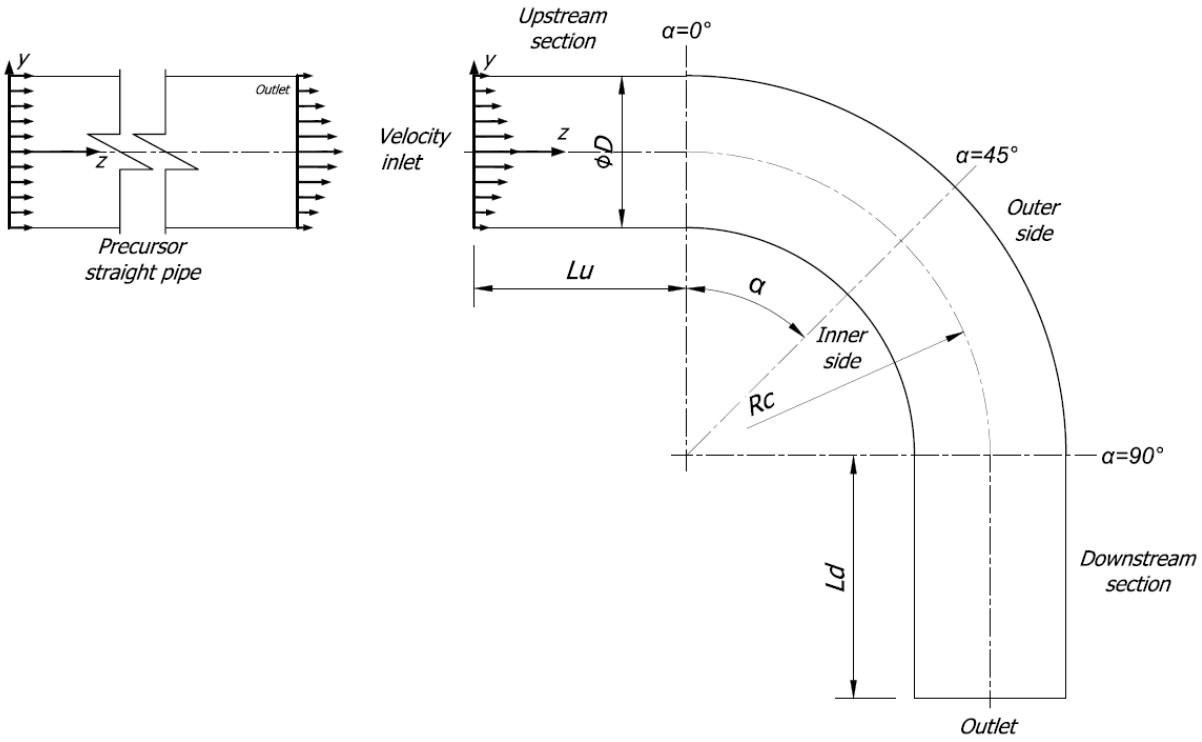

Figure 4.3. The computational domain topology for the pipe bend simulations.

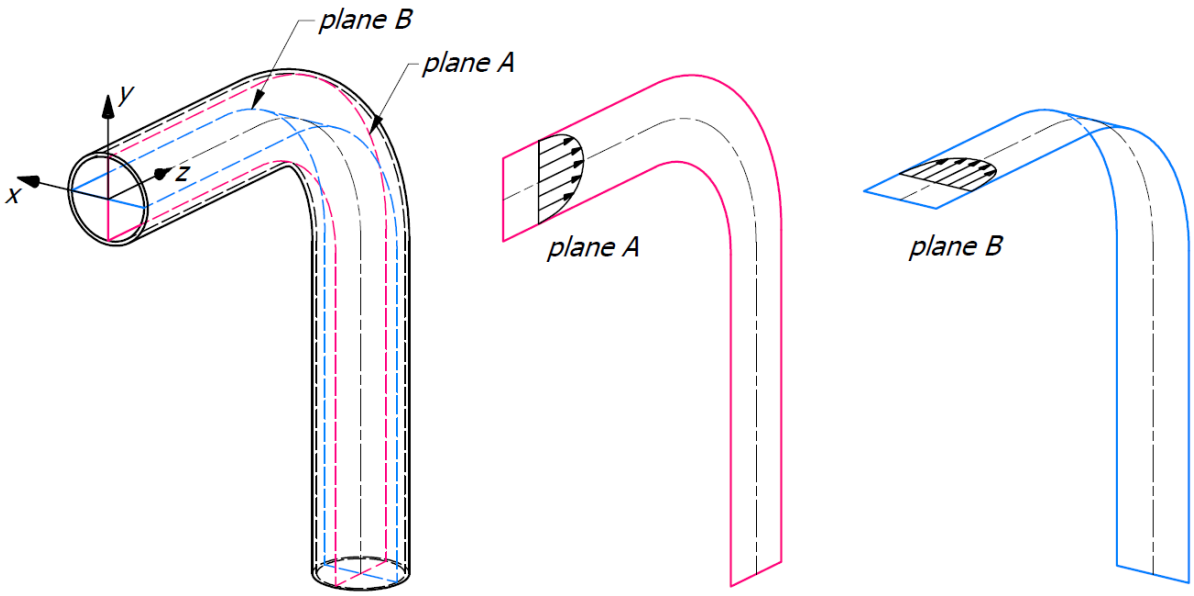

Figure 4.4. Location of the origin of the coordinate system and definition of planes A and B used in the results and discussion part.

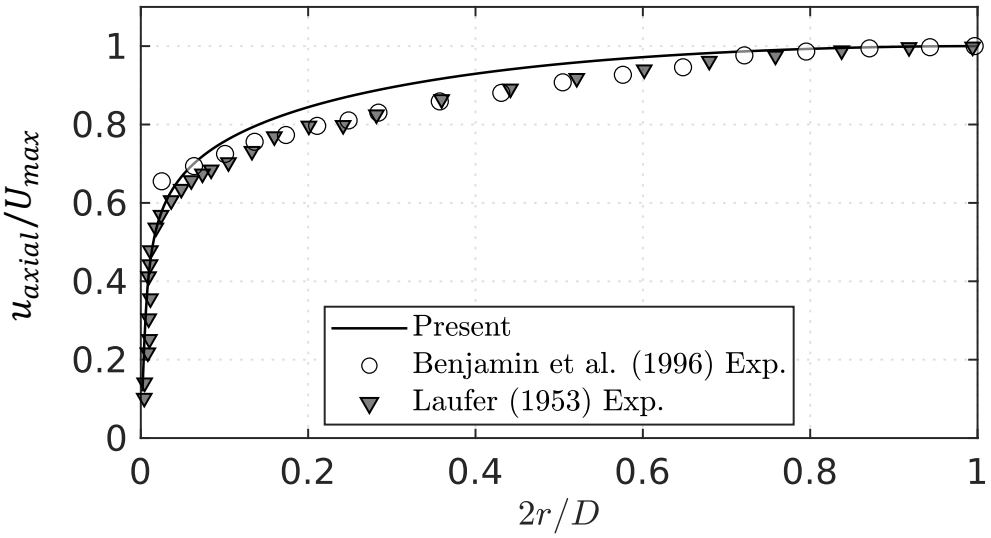

Figure 4.5. The radial profile of the normalised axial velocity in the straight pipe at Re = 60000 compared with the experimental data reported by Benjamin et al. [27] at Re = 60000 and Laufer [28] at Re = 50000.

4.3.2. Convergence study

The grid convergence studies are carried out to ensure that grid independent solutions are obtained. A set of four meshes for the pipe bend of Rc/D = 2 and $Re = 60000$ is generated using a constant refinement factor r = 1.25 in the pipe axis direction. The mesh is refined close to the walls of the domain to ensure that the $y^+ < 1$ (y^+ is defined as $y^+ = \Delta y u_*/\nu$, where u_* is the wall friction velocity and Δy is the distance between the

wall and the center of the first grid above the wall). The resulting cell numbers for different meshes, the thickness of the first grid layer adjacent to the wall and y^+ are presented in Table 4.1. The distributions of the normalized axial velocity in plane A at bend locations of $\alpha = 0^0, 45^0$ and 90^0 and also behind the bend: at $y/D = 2$ and 3 presented in Figure 4.7~4.10 are used to assess the mesh convergence. Based on the obtained velocity profiles, although there is difference in the velocity profiles close to the inner side of the bend pipe using different meshes due to the sensitivity of the separate flow at the bend outlet, a general good agreement is found between the results achieved for the meshes of M3 and M4 at other locations. Therefore, it is indicated that M3 can be considered to provide good balance between the computational cost and discretization error and the grid resolution of M3 is used for the remaining simulations in the present study. An example of the mesh is shown in Figure 4.6.

Table 4.1. Mesh resolutions investigated in the mesh convergence study

Mesh	Number of cells	Thickness of the first grid layer	y^+
M1	468832	$0.002D$	1.0946
M2	1491310	$0.001D$	0.7642
M3	3474300	$0.0006D$	0.5604
M4	6853632	$0.0003D$	0.4611

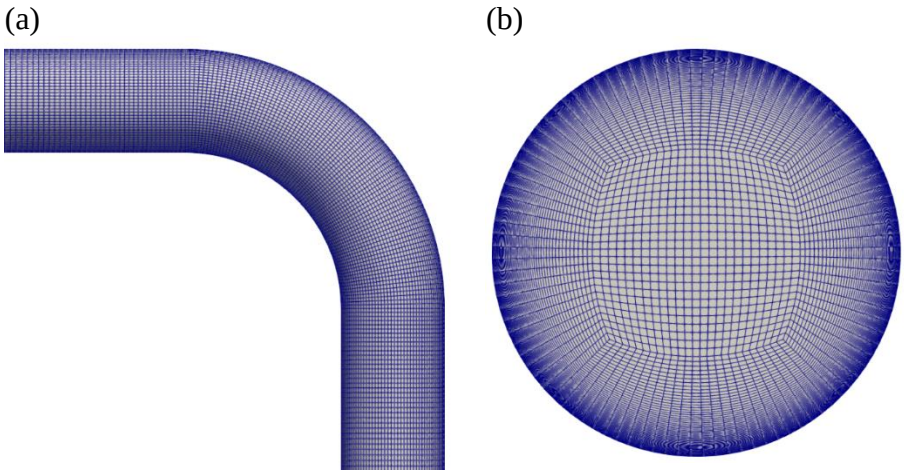

Figure 4.6. An overview of the computational mesh M3: (a) plan view of the surface mesh in the bend section, (b) cross-sectional view of the mesh.

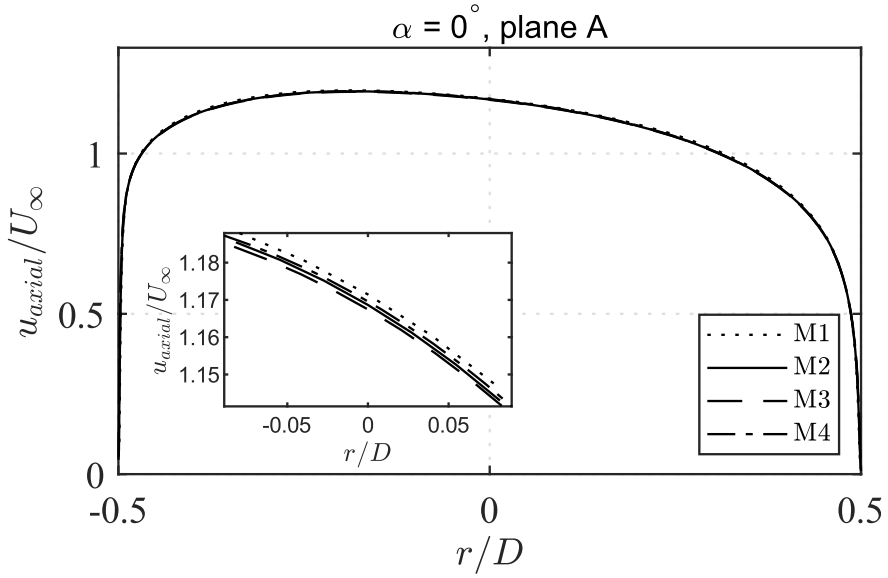

Figure 4.7. The normalised axial velocity at bend $\alpha = 0^0$ in plane A for Re = 60000 and $Rc/D = 2$ for the investigated mesh density variants: dotted: M1, solid: M2, dashed: M3 and dash-dotted: M4.

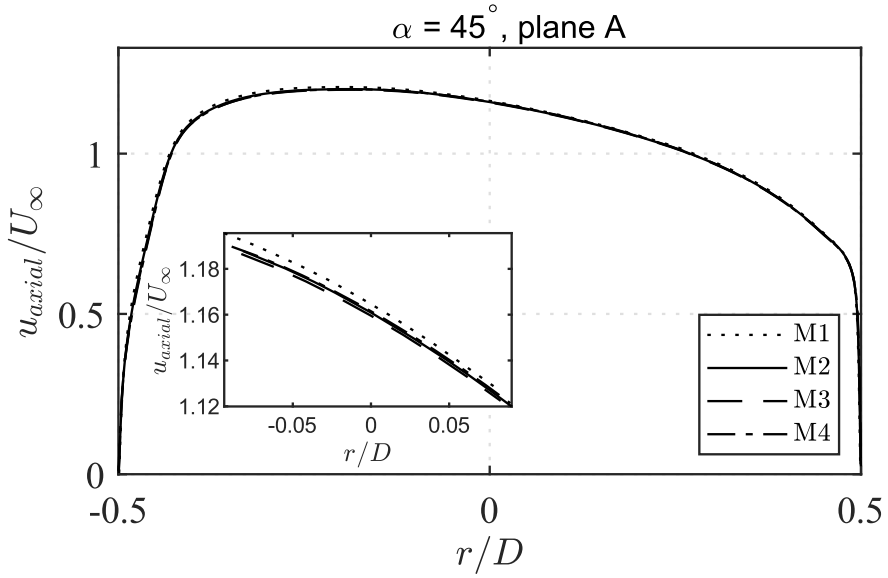

Figure 4.8. The normalised axial velocity at bend $\alpha = 45^0$ in plane A for Re = 60000 and $Rc/D = 2$ for the investigated mesh density variants: dotted: M1, solid: M2, dashed: M3 and dash-dotted: M4.

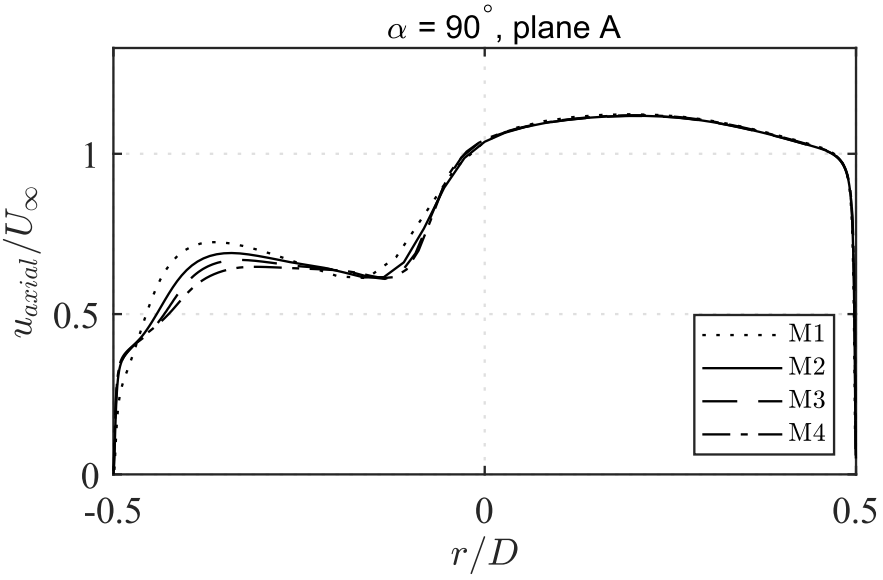

Figure 4.9. The normalised axial velocity at bend $\alpha = 90^0$ in plane A for Re = 60000 and $Rc/D = 2$ for the investigated mesh density variants: dotted: M1, solid: M2, dashed: M3 and dash-dotted: M4.

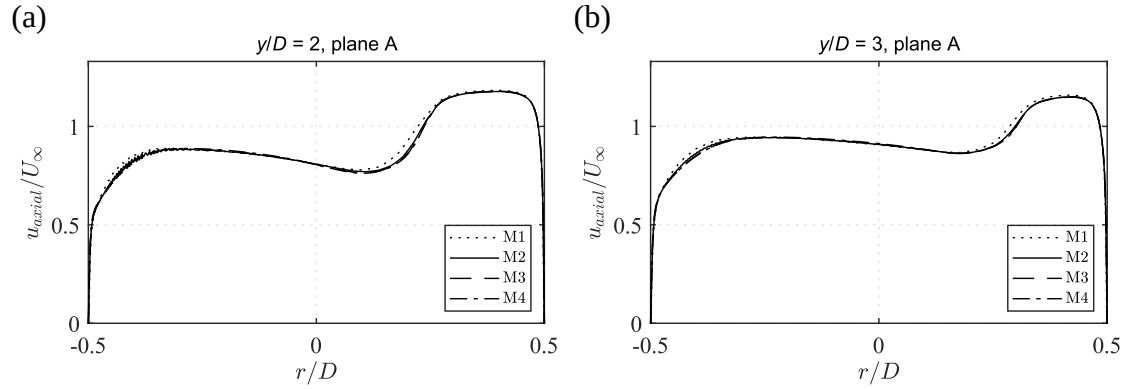

Figure 4.10. The normalised axial velocity at locations: (a) y/D = 2 and (b) y/D = 3 behind the bend in plane A for Re = 60000 and $Rc/D = 2$ for the investigated mesh density variants: dotted: M1, solid: M2, dashed: M3 and dash-dotted: M4.

4.3.3. Validation study

The results of the numerical simulation using the same grid resolution as the mesh M3 described in Section 4.3.2 is compared with the experimental data of Sudo et al. [11] for the 90-degree pipe bend to validate the present adopted numerical model to capture the essential behavior of the turbulent flow through a pipe bend. Sudo et al. [11] conducted their experiment by means of a single inclined hot wire velocity probe to measure the velocity of the flow in the 90-degree bend of cylindrical pipe at Re = 60000 and $Rc/D = 2$.

The normalized axial velocity profiles at the intersection angle $\alpha = 0^0$, 45^0 and 90^0 presented in Figure 4.11 show a fair agreement with the experimental measurements reported by Sudo et al. [11]. In terms of the axial velocity profiles in plane B, the velocity profiles are qualitatively similar to the experimental data and the differences are relatively small as shown in Figure 4.11 (b). Regarding the axial velocity profiles in plane A, some differences are observed compared with the experimental data reported by Sudo et al. [11] at the bend outlet in the inner side region as shown in Figure 4.11 (a) at $\alpha = 90^0$. However, the present results are closer to the numerical simulations reported by Tanaka et al. [20] using the LES approach than those obtained by Kim et al. [19] who employed the $k - \varepsilon$ RNG turbulence model for simulating the flow through the elbow. Therefore, it can be concluded that the present adopted EARSM show similar predicted results of the mean flow velocity distributions to the predictions using the LES model.

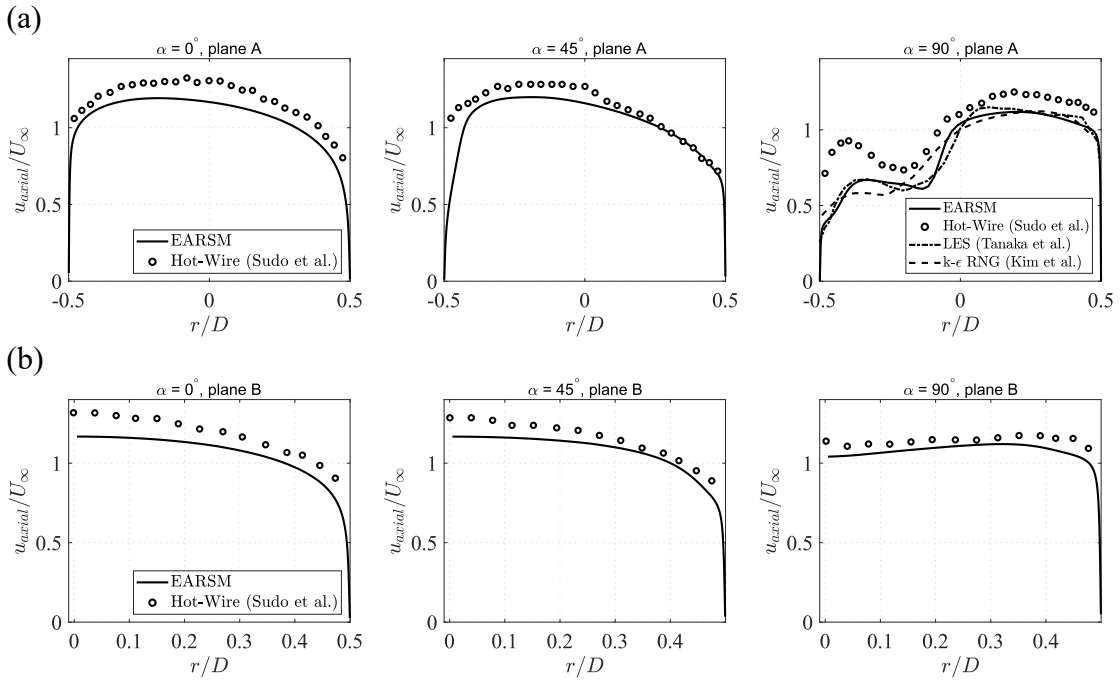

Figure 4.11. The normalized axial velocity in (a) plane A and (b) plane B at $\alpha = 0^0$, 45^0 and 90^0 for Re = 60000 and $Rc/D = 2$ compared with the experimental data reported by Sudo et al. [11] and the numerical simulation by Tanaka [20] and Kim [19] for plane A and $\alpha = 90^0$.

4.4. Results and discussions

4.4.1. Influences of the curvature ratios

A parametric study is carried out for different values of the curvature ratios: $Rc/D = 1, 2, 3$ and 4 at Re varying from 10000 to 60000 with the range of y^+ from 0.12 to 0.56, respectively. At Re = 60000, the normalized axial velocity profiles are investigated at two locations in the bend section ($\alpha = 45^0$ and $\alpha = 90^0$) and at the distance of $1D$

downstream of the bend section outlet. The obtained normalized axial velocity profiles in plane A are presented in Figure 4.12. Figure 4.12 (a) shows that at $\alpha = 0^0$ for $Rc/D = 1$, the velocity profile differs evidently at the inner side of the wall from the cases with $Rc/D = 2$, 3 and 4, where the velocity profiles exhibit similar shapes. Figure 4.12 (b) shows that at $\alpha = 45^0$, the flow close to the inner side of the bend is accelerated for Rc/D = 1 and 2 while for Rc/D = 3 and 4 the flow is decelerated near the inner side and the axial velocity shifts towards the outer side. In Figure 4.12 (c) , at the bend section outlet ($\alpha = 90^0$), the axial velocity displays a typical two-peaks distribution for Rc/D = 2 ~ 4 which has been reported in Dutta & Nandi [29]. With the increasing Rc/D, the axial velocity profile becomes increasingly skewed towards the outer side. For the smallest considered Rc/D = 1 at $\alpha = 90^0$, there is an obvious reversed flow near the inner side characterized by a negative axial velocity due to the flow separation from the inner side.

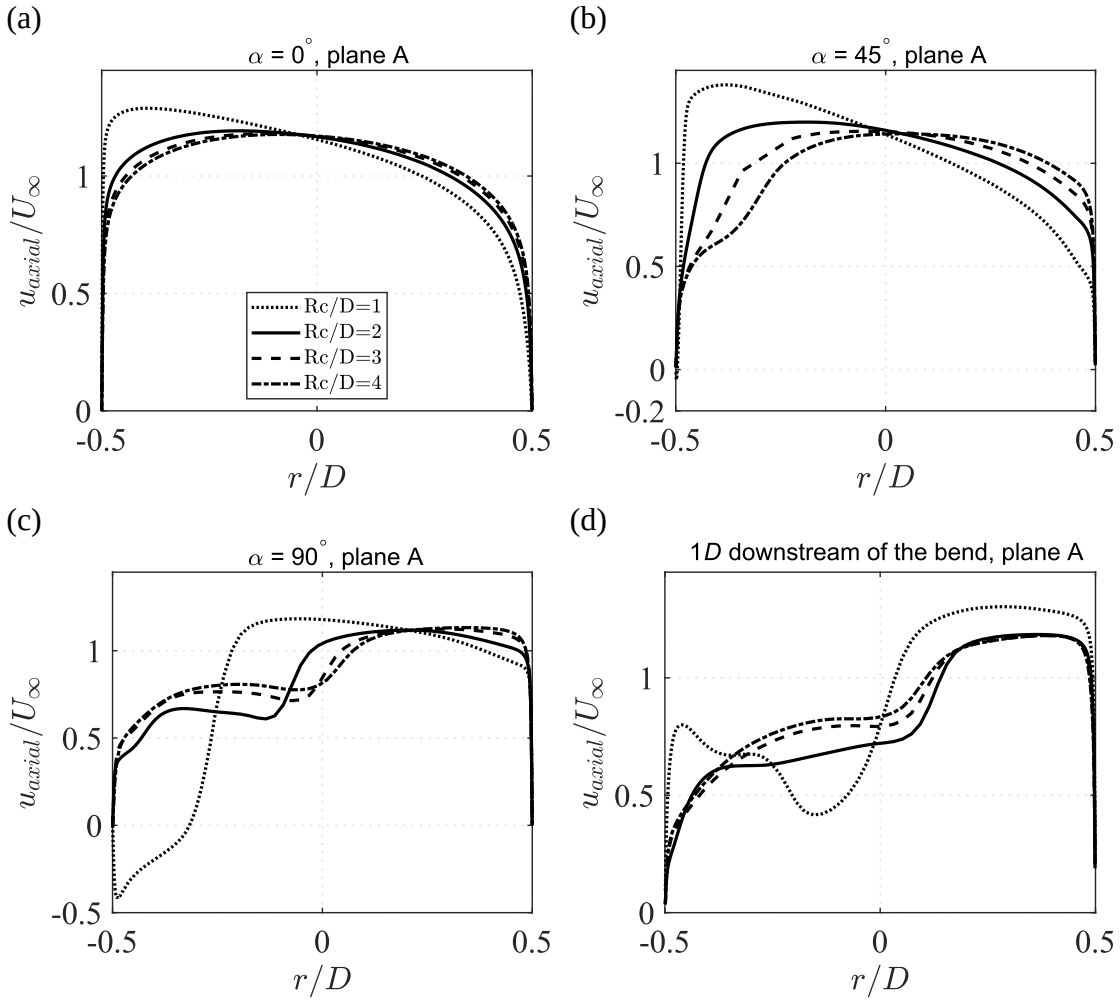

Figure 4.12. The normalised axial velocity at (a) $\alpha = 0^0$; (b) $\alpha = 45^0$; (c) $\alpha = 90^0$; and (d) the distance of 1D downstream of the bend for Re = 60000 in plane A for different values of the curvature ratio, Rc/D.

In Figure 4.12 (d), at the distance of $1D$ to the bend section outlet, a trend of recovery to the pipe flow can be observed in the increasing axial velocity close to the inner side with the increasing Rc/D. However, for Rc/D = 1, the velocity profile of the flow is still highly distorted. Figure 4.13~4.15 show pipe cross-sections oriented normal to the axial direction of the pipe at three locations: $\alpha = 0^0$, 45^0 and 90^0, respectively. The contours of the velocity perturbation U', the pressure p and the axial vorticity ω_{axial} as well as the streamlines in Figure 4.14 and Figure 4.15 are used to study the secondary flow patterns in the bend. Due to the weak secondary flow within the cross-section plane at $\alpha = 0^0$, the streamlines are not plotted in Figure 4.13. The velocity perturbation field is calculated by subtracting the fully developed axial velocity profile at inlet from the velocity field of the entire simulation domain. Therefore, the velocity perturbation shows only the influence of the pipe curvature on the fluid behavior and the deviation from the flow through the straight pipe can be clearly observed. The velocity perturbation, the pressure and the axial vorticity are scaled by U, $U^2\rho$ and U/D, respectively to get non-dimensional physical properties. The axial vorticity refers to the vorticity component in the axial direction of the pipe. The left side of each cross-section corresponds to the inner side of the pipe bend and the right side of each cross-section corresponds to the outer side of the pipe bend, as shown in Figure 4.3.

It can be seen that at $\alpha = 0^0$, a slight deviation from the straight pipe flow begins to form as seen from U' close to the pipe wall. For $Rc/D = 4$, this deviation is small compared with other cases. A pressure gradient also begins to be generated across the planes for all investigated cases. A pair of asymmetric vortices are induced close to the two side walls. At $\alpha = 45^0$ and $\alpha = 90^0$, larger values of velocity perturbations are discernible at the inner side of the bend for Rc/D = 1 due to the stronger flow deformation caused by the bend compared with other cases, especially at $\alpha = 0^0$ in Figure 4.13. Whereas, for increasing Rc/D the region of low values of velocity perturbation gets wider and moves towards the outer side. There is pronounced pressure difference between the inner and outer side due to the centrifugal force acting on the fluid. The pressure difference becomes lower with the increasing Rc/D and with the increasing α. It can be noticed that the strong axial vorticity is close to the pipe wall due to the large velocity gradient within the pipe flow boundary layer. The Dean vortices are also observed in the form of two counter-rotating flows that stay symmetric with respect to the geometric plane of symmetry. In addition, with the increasing Rc/D, the cores of the recirculation motion are moved towards the inner side where there are also located two increasing regions of the strong vorticity at $\alpha = 45^0$ in Figure 4.14. On the other hand, at $\alpha = 90$ in Figure 4.15, the region of the strong vorticity contracts and the vorticity gets weaker for the increasing Rc/D.

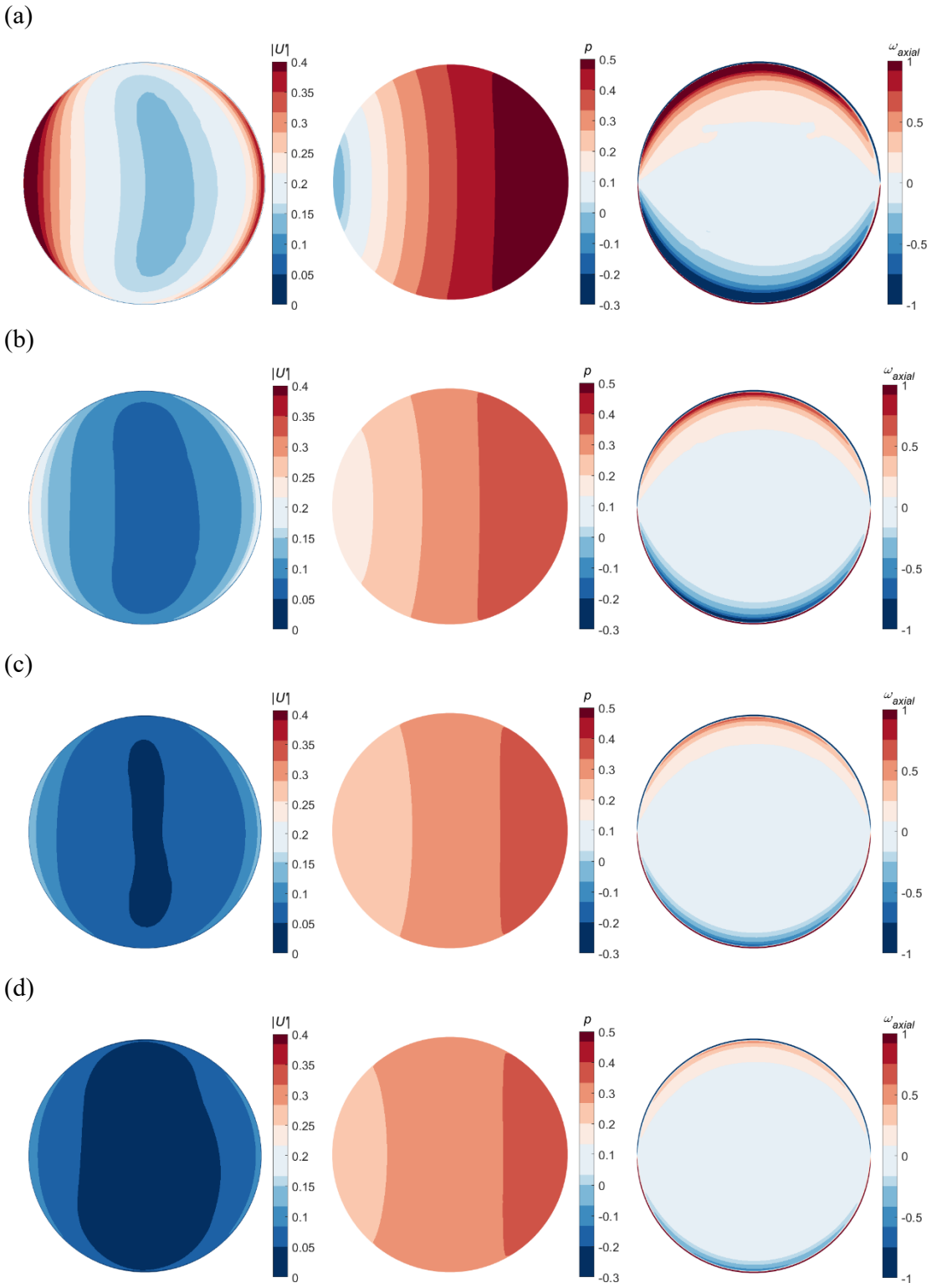

Figure 4.13. The non-dimensional physical properties: the magnitude of the velocity perturbation, the pressure and the axial vorticity (from the leftmost respectively) visualized at $\alpha = 0^0$ for (a) Rc/D = 1, (b) Rc/D = 2, (c) Rc/D = 3 and (d) Rc/D = 4 for Re = 60000.

(a)

(b)

(c)

(d)

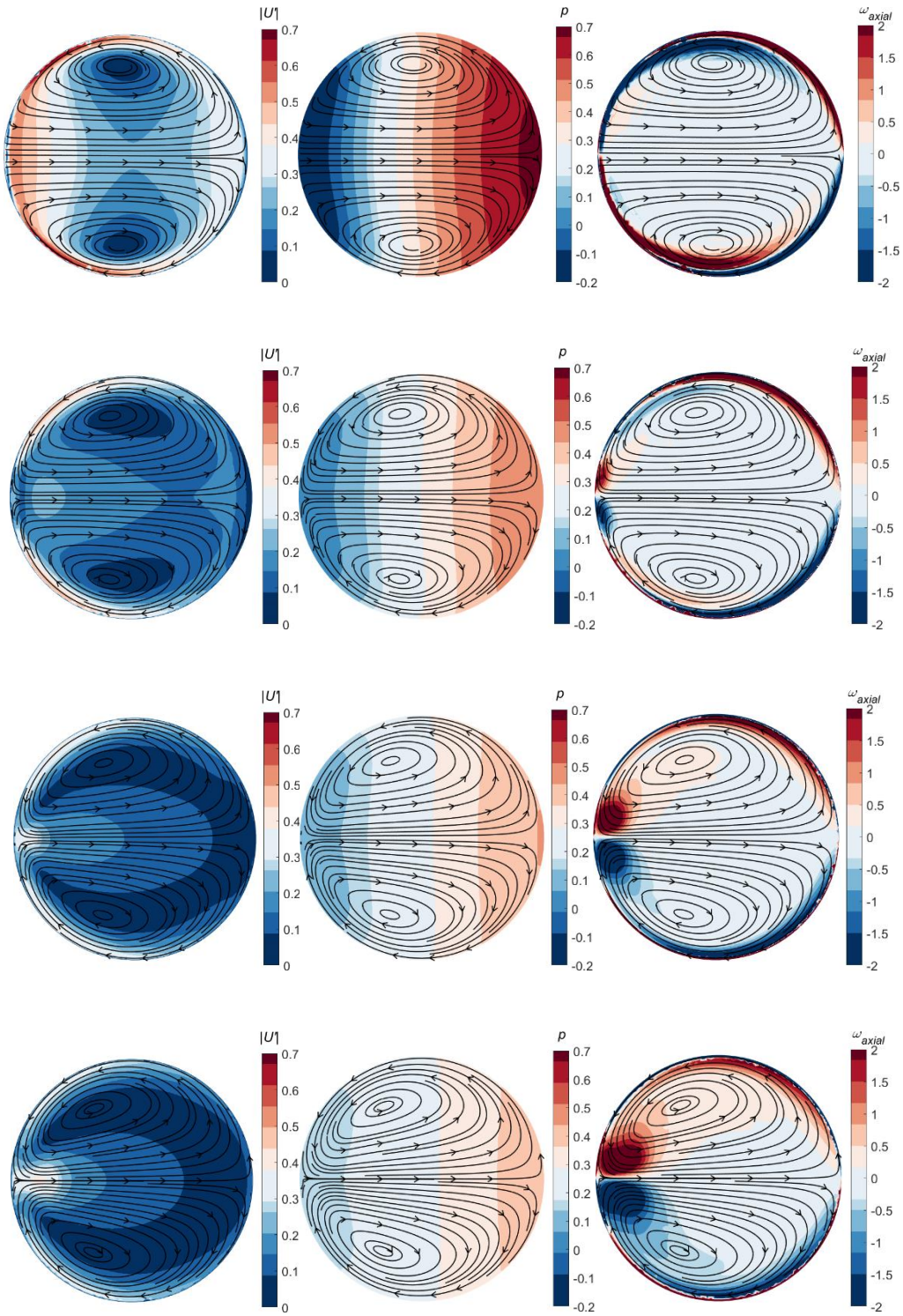

Figure 4.14. Secondary flow and non-dimensional physical properties: the magnitude of the velocity perturbation, the pressure and the axial vorticity (from the leftmost respectively) visualized at $\alpha = 45^0$ for (a) Rc/D = 1, (b) Rc/D = 2, (c) Rc/D = 3 and (d) Rc/D = 4 for Re = 60000.

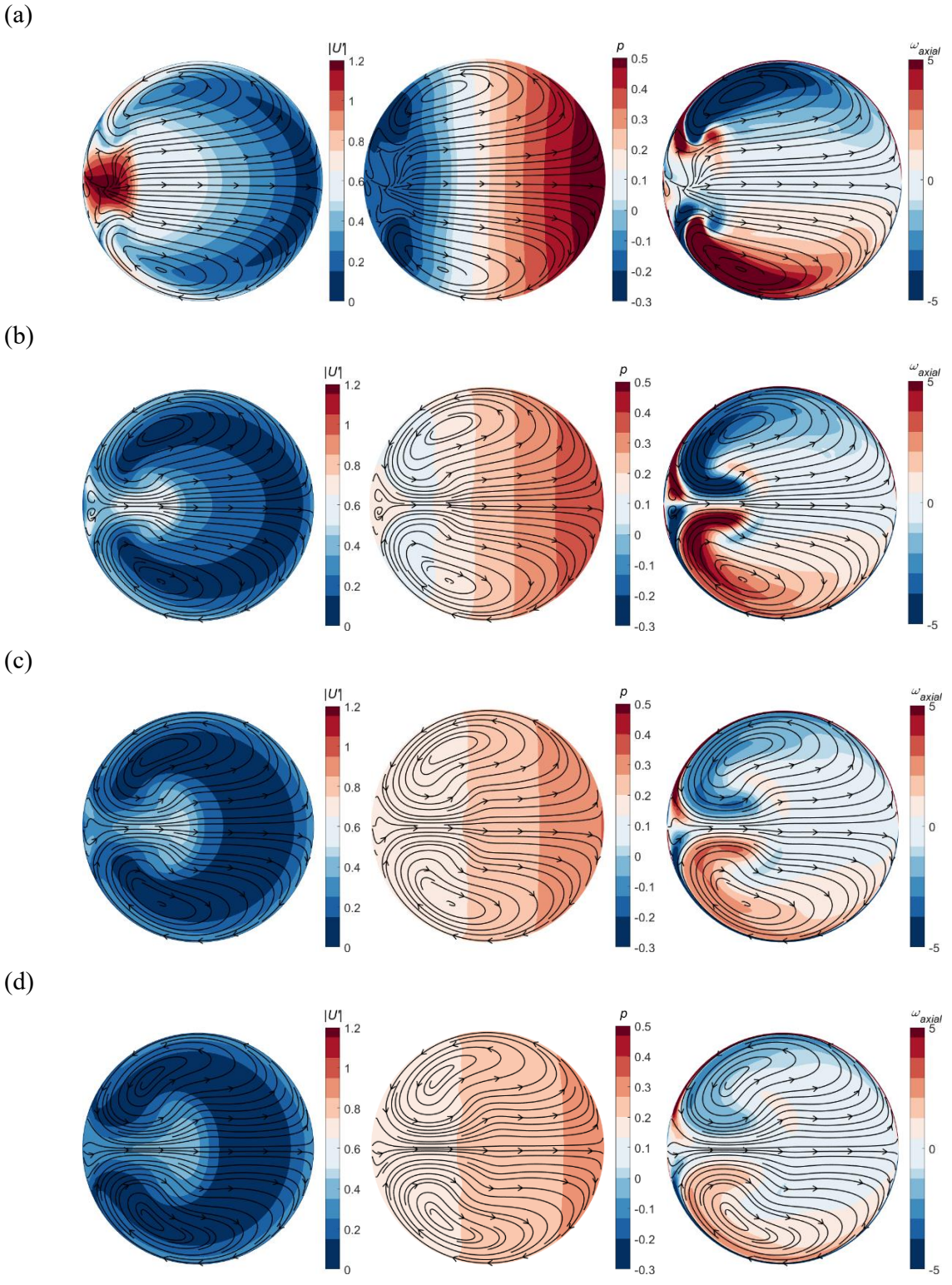

Figure 4.15. Secondary flow and non-dimensional physical properties: the magnitude of the velocity perturbation, the pressure and the axial vorticity (from the leftmost respectively) visualized at $\alpha = 90^0$ for (a) Rc/D = 1, (b) Rc/D = 2, (c) Rc/D = 3 and (d) Rc/D = 4 for Re = 60000.

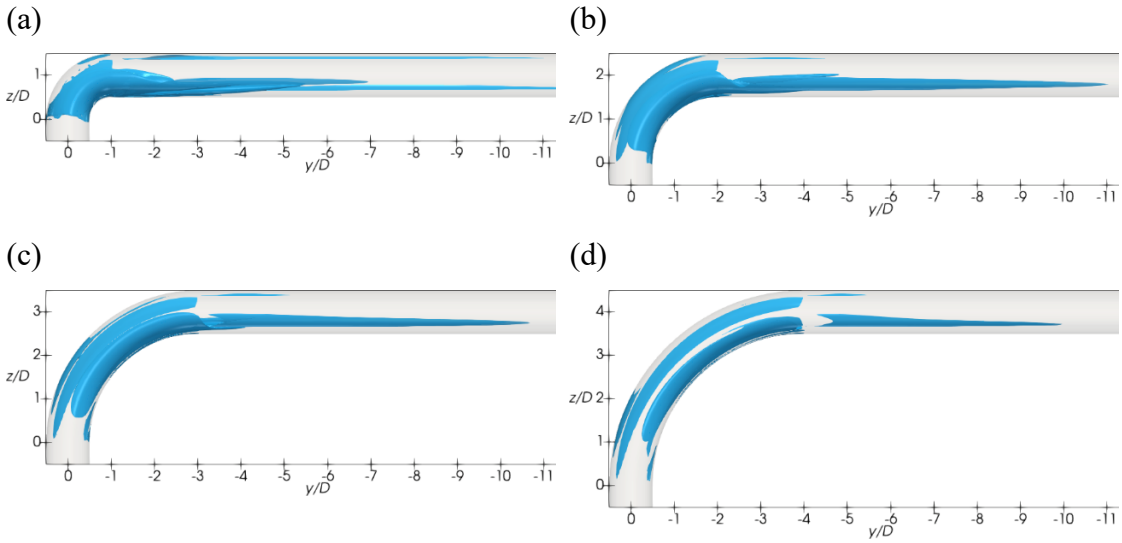

Figure 4.16. The iso-surfaces of the Q-criterion for $Q = 1$: (a) $Rc/D = 1$; (b) $Rc/D = 2$; (c) $Rc/D = 3$ and (d) $Rc/D = 4$ at Re = 60000.

The behavior of the swirling flow for the different curvature ratio is also presented by the vortical structures behind the bend inlet identified by the Q criterion given as $Q = (\Omega^2 - S^2)/2$, where S and Ω are the strain and the rotation tensors, respectively. A single level of $Q = 1$ iso-surfaces are shown in Figure 4.16. It can be seen that in general, strong vortical structures cover the bend pipe and the vortical structures propagate downstream behind the bend. With the increasing Rc/D, the $Q = 1$ iso-surfaces are increasingly gathered around the inner and outer sides of the bend pipe. Additional contours of Q in the cross-sections at $\alpha = 45^0$, $\alpha = 90^0$ and $1D$ distance behind the bend are shown in Figure 4.17. The swirling flow is more dominant for the smaller curvature ratio. With the increasing distance from the bend inlet, the vortices move slightly from the inner side towards the center of the cross-section and their strengths become weaker. The Q contours remain symmetric with respect to the z axis at almost all locations except at the distance of $1D$ behind the pipe bend with Rc/D = 1, which may be due to the extremely distorted flow caused by sudden change of the flow direction through the bend with a small radius. With the increasing Rc/D, the strength of Q becomes almost uniform within the cross-section as shown in Figure 4.17 (d).

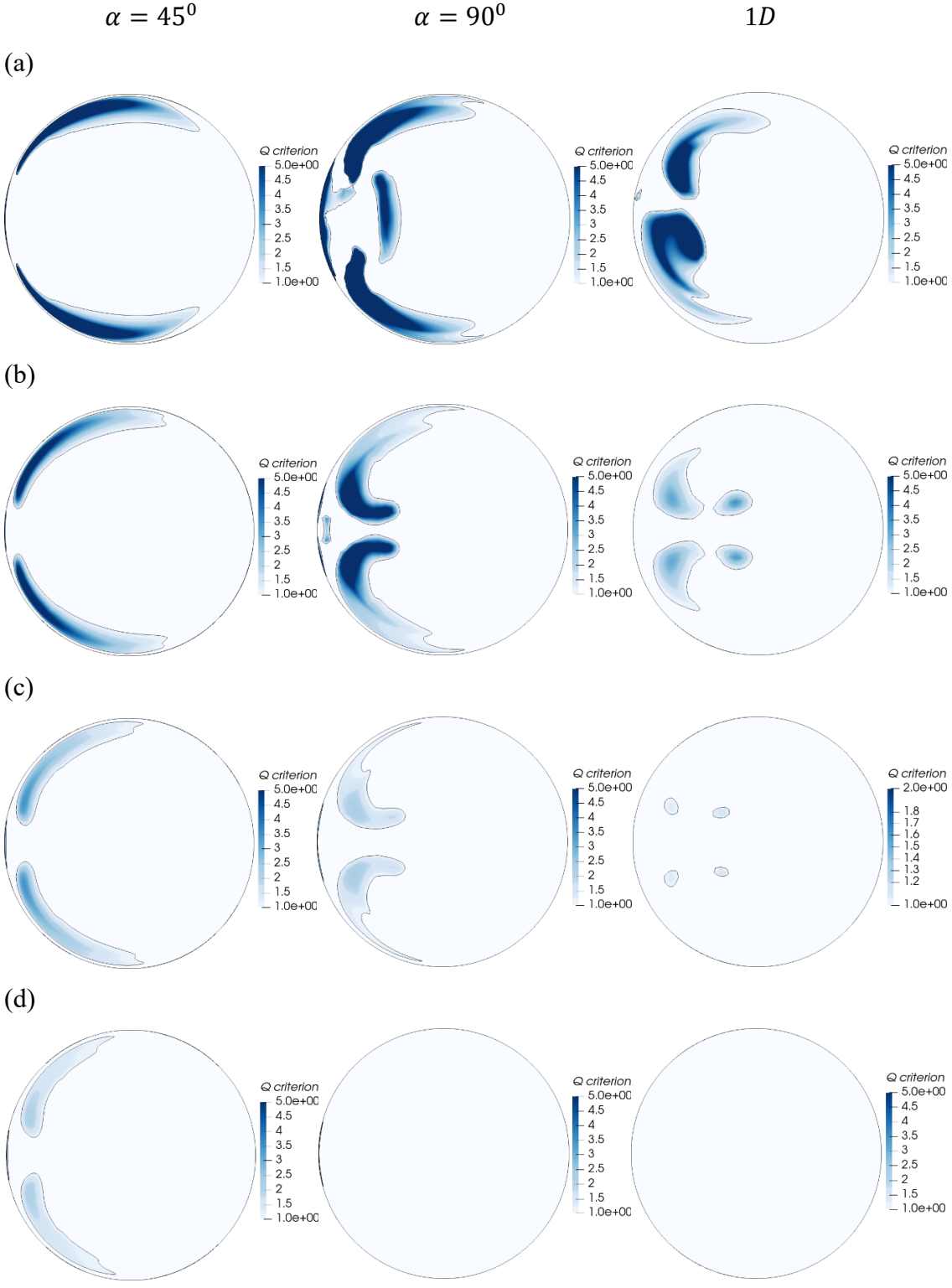

Figure 4.17. Contours of the Q criterion plotted on pipe cross sections for (a) Rc/D = 1, (b) Rc/D = 2, (c) Rc/D = 3 and (d) Rc/D = 4 at Re = 60000.

4.4.2. Influences of Reynolds number

For the further study, the pipe bends with different curvature ratios are chosen to evaluate the effects of Re ranging from 10000 to 60000 on the flow behaviors. The axial velocity profiles for the different Re are compared at three locations: the bend inlet at $\alpha = 0^0$, in the middle of the bend at $\alpha = 45^0$ and at the bend outlet of $\alpha = 90^0$ as shown in Figure 4.18. At $\alpha = 0^0$, the velocity profiles for different Re display similar shapes except around the pipe centerline, there is a slight decrease in the axial velocity with the increasing Re. Especially for $Rc/D = 4$, the velocity profile tends to become flat around the pipe centerline. At $\alpha = 45^0$ for $Rc/D = 1$ and 2, the near-wall velocity gradient becomes larger while there is a decrease in the accelerate region close to the outer side with the increasing Re. For $Rc/D = 4$, there is a trend of an increasing velocity close to the inner side while a decreasing velocity close to the outer side with the increasing Re, which indicates a reduction of the curvature effects at higher Re. A similar trend is also observed at $\alpha = 90^0$. For $Rc/D = 1$ and 2, the accelerate region becomes switch towards the inner side with the increasing Re. However, for $Rc/D = 1$, there is almost no Re effect on the velocity profiles. In addition, the secondary flows are represented by the streamlines plotted at two locations: $\alpha = 45^0$ and $\alpha = 90^0$ in Figure 4.19 and 4.20. It can be seen that the swirling motions show overall similar patterns. With the increasing Re, the amplitudes of the high-pressure region close to the outer side are reduced while they are enhanced in the low-pressure region close to the inner side. At $\alpha = 90^0$, the high vorticity tends to be attached to the inner side from the pipe center with the increasing Re, which indicates that the flow tends to be less deformed by the bend at higher Re.

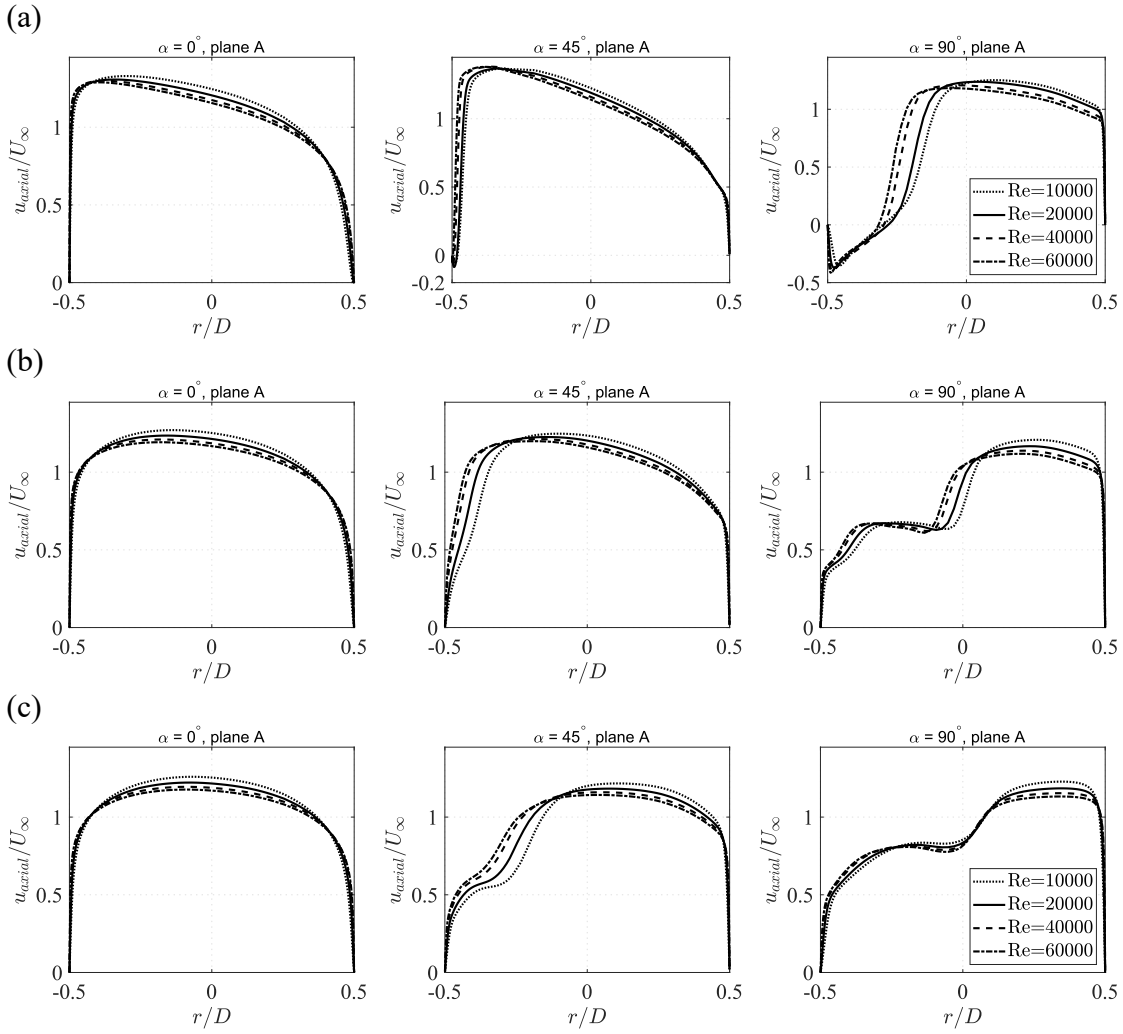

Figure 4.18. The normalized axial velocity for (a) $Rc/D = 1$; (b) $Rc/D = 2$ and (c) $Rc/D = 4$ at $\alpha = 0^0$, 45^0 and 90^0 in plane A for different Reynolds numbers.

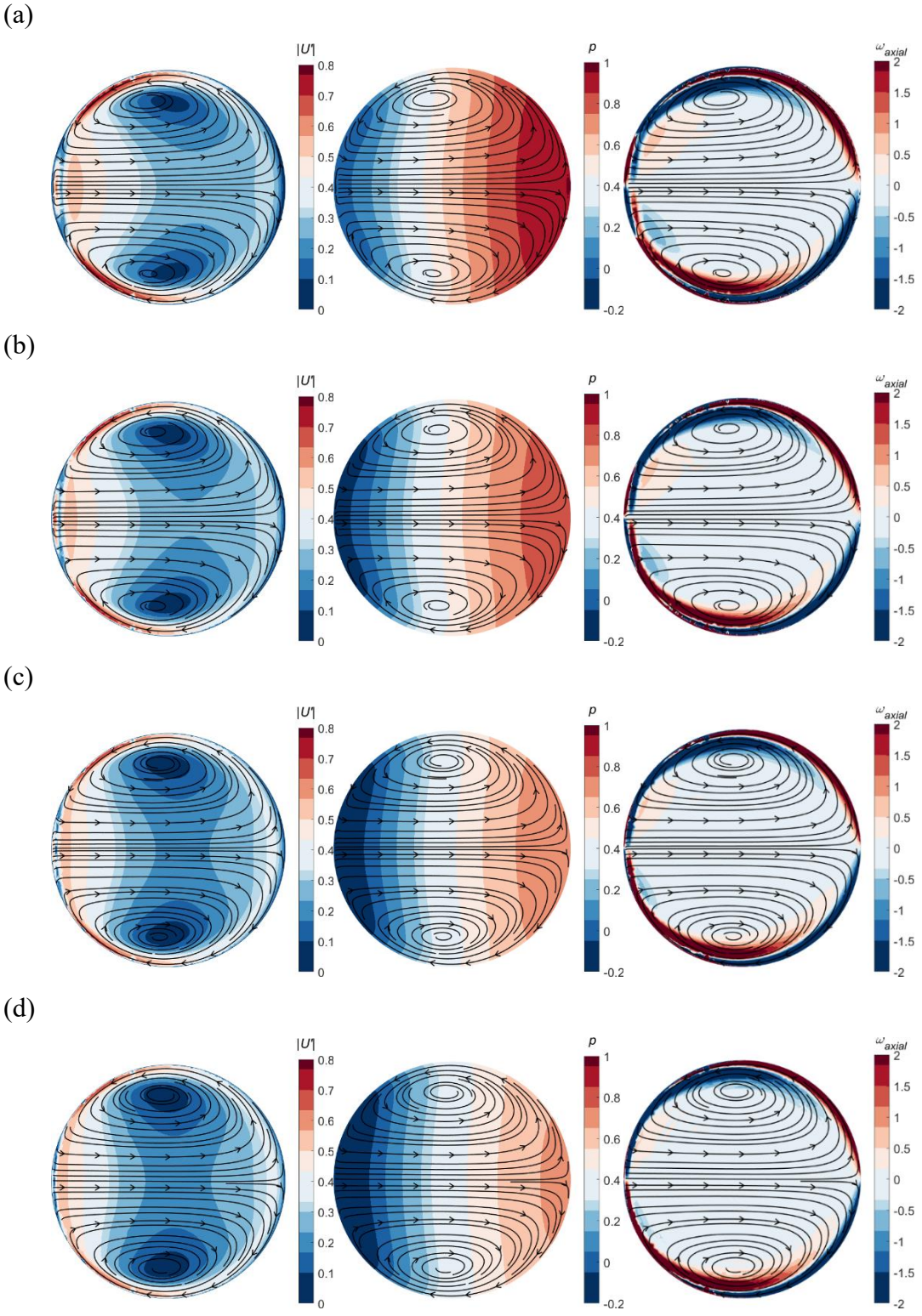

Figure 4.19. Secondary flow and non-dimensional physical properties: the magnitude of the velocity perturbation, the pressure and the axial vorticity (from the leftmost respectively) visualized at $\alpha = 45^0$ for (a) Re = 10000, (b) Re = 20000, (c) Re = 40000 and (d) Re = 60000 for Rc/D = 1.

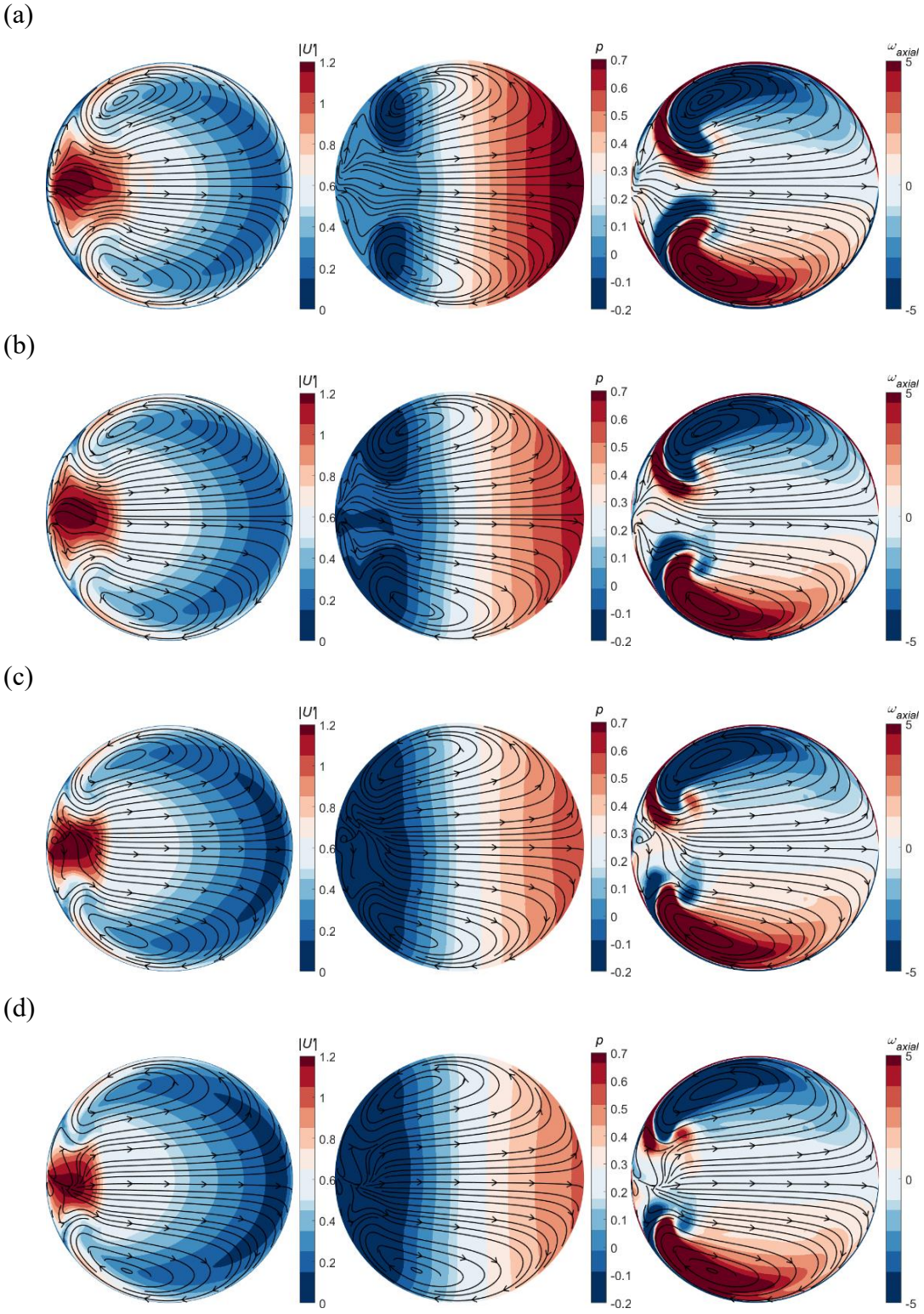

Figure 4.20. Secondary flow and non-dimensional physical properties: the magnitude of the velocity perturbation, the pressure and the axial vorticity (from the leftmost respectively) visualized at $\alpha = 90^0$ for (a) Re = 10000, (b) Re = 20000, (c) Re = 40000 and (d) Re = 60000 for Rc/D = 1.

4.5. Conclusion

In the present study, the CFD simulations are performed to investigate the behavior of the flow through a 90-degree pipe bend with different curvature ratios and at different Reynolds numbers. For the first time, the EARSM turbulence model is used to resolve the Reynolds stress in the pipe bend, which considers the turbulence anisotropy. The predicted results using the selected converged grid resolution show a good agreement with the experimental data confirming the validity of the present numerical model for simulating turbulent flows through the pipe bend and indicated that the EARSM has better agreement with the experimental data than other turbulence models used so far in the published literature. Numerical simulations are then performed to investigate the flow characteristics for different curvature ratios of the bend and different Re. It is found that the flow behavior at the pipe bend and downstream the bend depends strongly on the curvature ratio of the bend (Rc/D) resulting in highly deformed flow for $Rc/D < 2$. The main conclusion based on the present work is summarized as follows:

- The velocity profiles become highly skewed with a pronounced velocity deficit on the inner side of the cross-section and accelerated fluid flow on the outer side. The strength of the velocity perturbation becomes larger as well as the pressure gradients in the cross-section increase with the decreasing Rc/D. The vortical structure also becomes stronger. For pipe geometries with Rc/D larger than 1, there is also strong axial vorticity induced from the inner side to the center of the bend.
- Within the investigated range of Re, physical quantities such as the axial velocity, the velocity perturbation, the pressure difference and the vorticity observed for a given geometry are relatively insensitive to the varying Re. With the increasing Re, there is a trend of a weakening influence of the bend radius on the flow behavior.

Acknowledgement

This study was supported with computational resources provided by the Norwegian Metacenter for Computational Science (NOTUR), under Project No: NN9372K.

References

[1] Berger, S.A., Talbot, L. and Yao, L.S., 1983. Flow in curved pipes. *Annu. Rev. Fluid Mech.*, Vol.15, pp.461-512.

[2] Jayanti, S., Bends, Flow and Pressure Drop in. A-to-Z Guide to Thermodynamics, Heat & Mass Transfer, and Fluids Engineering. https://www.thermopedia.com/content/577/, 2021 (accessed 30 August 2021).

[3] Thomson, J., 1876. On the origin of windings of rivers in alluvial plains, with remarks on the flow of water round bends in pipes. *Proc. R. Soc. London*, Vol.25, pp. 5-8.

[4] Williams, G.S., Hubbell, C.W. and Finkell, G.H., 1902. Experiments at Detroit, Michigan on the effect of curvature on the flow of water in pipes. Trans. ASCE, Vol.47, pp. 1-196.

[5] Eustice, J., 1911. Experiments of Streamline Motion in Curved Pipe. *Proc. R. Soc. London, Ser. A*, 85, pp. 119-131.

[6] Dean, W.R., 1927. Note on the Motion of Fluid in a Curved Pipe. *Philosophical Magazine and Journal of Science*, Vol. 4, 20, pp. 208-223.

[7] Dean, W.R., 1928. The Stream-line Motion of Fluid in a Curved Pipe. *Philosophical Magazine and Journal of Science*, Vol. 5, 30, pp. 673-695.

[8] Weske, J.R., 1948. Experimental investigation of velocity distributions downstream of single duct bends. *National Advisory Committee for Aeronautics*, NACA-TN-1471.

[9] Enayet, M. M., Gibson, M. M., Taylor, A. M. K. P., & Yianneskis, M. 1982. Laser-Doppler measurements of laminar and turbulent flow in a pipe bend. *International Journal of Heat and Fluid Flow*, 3(4), pp. 213-219.

[10] Azzola, J., Humphrey, J.A.C., Iacovides, H. and Launder, B.E., 1986. Developing turbulent flow in a U-bend of circular cross-section: measurement and computation. *Journal of Fluids Engineering*, 108, pp. 214-221.

[11] Sudo, K., Sumida, M. and Hibara, H., 1998. Experimental investigation on turbulent flow in a circular-sectioned 90-degree bend. *Exp. Fluids* 25, pp. 42-49.

[12] Shiraishi, T., Watakabe, H., Sago, H., Konomura, M., Yamaguchi, A. and Fujii, T., 2006. Resistance and Fluctuating Pressures of a Large Elbow in High Reynolds Numbers. *J. Fluids Eng.*, Vol.128, pp.1063-1073.

[13] Hellström, L.H., Zlatinov, M.B., Cao, G. and Smits, A.J., 2013. Turbulent pipe flow downstream of a bend. *Journal of Fluid Mechanics*, 735, pp. 1-12.

[14] Patankar, S.V., Pratap, V.S. and Spalding, D.B., 1975. Prediction of turbulent flow in curved pipes. *Journal of Fluid Mechanics*, 67(3), pp. 583-595.

[15] Masud, M.A., Islam, R., Sheikh, R. and Alam, M., 2010. Stable solution zone for fluid flow through curved pipe with circular cross-section. *Journal of Naval Architecture and Marine Engineering*, 7(1), pp. 1813-8235.

[16] Dutta, P., Saha, S.K., Nandi, N. and Pal, N., 2016. Numerical study on flow separation in 90^0 pipe bend under high Reynolds number by $k-\varepsilon$ modelling. *Eng. Sci. Technol. Int. J.*, 19(2), pp. 904-910.

[17] Dutta, P., & Nandi, N. 2021. Numerical analysis on the development of vortex structure in 90 pipe bend. *Progress in Computational Fluid Dynamics, an International Journal*, 21(5), pp. 261-273.

[18] Dutta, P., Chattopadhyay, H., & Nandi, N. 2022. Numerical Studies on Turbulent Flow Field in a 90 deg Pipe Bend. *Journal of Fluids Engineering*, 144(6), pp. 061104.

[19] Kim, J., Yadav, M. and Kim, S., 2014. Characteristics of Secondary Flow Induced by 90-Degree Elbow in Turbulent Pipe Flow. *Eng. Appl. Comput. Fluid Mech.*, 8(2), pp. 229-239.

[20] Tanaka, M., Ohshima, H. and Monji, H., 2009. Numerical investigation of flow structure in pipe elbow with large eddy simulation approach. *Proceedings of the ASME 2009 Pressure Vessels and Piping Division Conference PVP2009*, July 26-30, PVP-77598.

[21] Bovendeerd, P.H.M, Van Steenhoven, A.A., Van de Vosse, F.N. and Vossers, G., 1987. Steady entry flow in a curved pipe. *J. Fluid Mech.*, 177, pp. 233-246.

[22] Noorani, A., El Khoury, G.K. and Schlatter, P., 2013. Evolution of turbulence characteristics from straight to curved pipes. *International journal of heat and fluid flow*, 41, pp.16-26.

[23] Jurga, A.P., Janocha, M.J., Yin, G., Giljarhus, K.E.T. and Ong, M.C., 2021. Validation and assessment of different RANS turbulence models for simulating turbulent flow through an orifice plate. *IOP Conf. Ser.: Mater. Sci. Eng.* 1201, pp. 012019.

[24] Hellsten, A., 2005. New Advanced k-omega Turbulence Model for High-Lift Aerodynamics. *AIAA J.*, 43(9), pp.1857-1869.

[25] Wallin, S. and Johansson, A.V., 2000. An Explicit Algebraic Reynolds Stress Model for Incompressible and Compressible Turbulent Flows. *J. Fluid Mech.*, 403, pp. 89-132.

[26] ANSYS, Inc. ANSYS Fluent User'r Guide, Release 15.0, November 2013.

[27] Benjamin, S.F., Clarkson, R.J., Haimad, N. and Girgis, N.S. 1996. An Experimental and Predictive Study of the Flow Field in Axisymmetric Automotive Exhaust Catalyst Systems. *SAE Int. J. Fuels Lubr. SAE International*, 105(4), pp. 1008-1019.

[28] Laufer, J. 1953. The structure of turbulence in fully developed pipe flow, National Advisory Committee for Aeronautics-Report-1174, pp. 417-434.

[29] Dutta, P. and Nandi, N., 2015. Effect of Reynolds number and curvature ratio on single phase turbulent flow in pipe bends. Mechanics and Mechanical Engineering, 19(1), pp. 5-16.

Chapter 5.

Numerical investigations of turbulent flow through a 90-degree pipe bend and honeycomb straightener

Agata Patrycja Jurga [a], Marek Jan Janocha [a], Guang Yin [a] and Muk Chen Ong [a]

[a] Department of Mechanical and Structural Engineering and Materials Science, University of Stavanger, Stavanger, Norway.

Published as:

Jurga, A.P., Janocha, M.J., Yin, G. and Ong, M.C., 2022. Numerical investigations of turbulent flow through a 90-degree pipe bend and honeycomb straightener. (Draft). To be submitted to Journal of Offshore Mechanics and Arctic Engineering.

Abstract

Flow straighteners are devices used in piping systems to remove the swirling in a flow caused by pipe fittings such as bend pipes, elbows or reducers. In the present study, the design considerations for the honeycomb straightener inserted downstream of a 90-degree pipe bend are explored. The cross-section shape of the investigated honeycomb constitutes regular hexagonal pattern. The turbulent flow through the 90-degree circular pipe bend with the honeycomb straightener is investigated by carrying out numerical simulations using the Reynolds-Averaged Navier–Stokes (RANS) turbulence modelling approach. The Explicit Algebraic Reynolds Stress Model (EARSM) is adopted to resolve the Reynolds stresses. The objective of the present work is to evaluate the effectiveness of the honeycomb at suppressing the flow swirling for different distances from the bend outlet (Lb) and different values of the honeycomb thickness (t). The effectiveness is measured by investigating flow parameters such as the axial velocity profile, swirl intensity and vorticity. The honeycomb thickness to pipe diameter ratio (t/D) is varied between 0.1 and 1. The normalized distance from the bend outlet to the honeycomb straightener (Lb/D) is varied between 1 and 5 and. The disturbance in the velocity field is generated by the pipe bend with the curvature radius to pipe diameter ratio (Rc/D) of 2 and Reynolds number (Re) of 2×10^5. The numerical model is validated by comparing the axial velocity profiles with the previous published experimental data. It is found that both the increase in Lb/D and t/D improves the performance of the device in removing the swirl behind the bend outlet. The swirl intensity decreases exponentially along the flow. Although, the axial velocity profile gets smoother for larger Lb/D, the profile is not fully recovered to the straight pipe flow. The best performance is reached for the honeycomb straightener located at the distance $Lb/D = 5$ and thickness $t/D = 0.5$.

5.1. Introduction

Flow straighteners next to flow conditioners are devices that can greatly reduce or eliminate swirl created by pipe fittings such as bend pipes, elbows or reducers. Although the term “flow conditioner” can also describe the flow straightener which works as a swirl remover, the latter may not simultaneously achieve the acceptable flow conditions specified in ISO 5167-1, 7.3.3 [1] and thus may not produce the fully developed flow. Flow conditioners are positioned downstream of a pipe fitting. They have two main advantages: eliminate the swirl and restore the symmetry of the velocity profile. Swirl, as described by Baker [2], requires a long flow path to decay and can introduce severe metering inaccuracies. Firstly, by reducing the installation length of the straight pipe required to reach the fully developed flow, flow conditioners contribute to save large amount of space. Secondly, when positioned between the pipe fitting and a flow meter, they improve the accuracy of the flow rate measurement which is maximized when a velocity profile is fully developed and free from swirl. Thus, the application of the flow conditioners is cost effective and essential for optimizing measurement performance of a flow meter.

Numerous experimental and numerical investigations have been performed in the past decades to study the effectiveness of various types of flow conditioners in the piping systems. In 1990 Laws [3] invented a flow conditioner that met the requirements of ISO 5167 [3] regarding the swirl and flow conditions within a relative short straight run piping. The experimental work was carried out in test rigs at Re = 1.8×10^5 and the velocity and swirl measurements were performed by means of a Pitot rake and a Conrad yaw meter, respectively. The flow conditioner by Laws [3] consisted of a perforated plate with a central hole and holes at the inner and outer rings. The plate had holes of increasing diameters towards the plate center and decreasing near the plate edge. Laws [3] gave limited combinations of hole sizes and their numbers ensuring that the plate could produce effectively swirl-free fully developed flow. Bates [4] indicated the effectiveness of the K-lab flow conditioner in the gas metering system on a process platform in the Alwyn North field. The flow meter was positioned $30D$ from the pipe reduction and it turned out that this length was not sufficient to naturally dissipate the strong swirl. This issue was corrected by installing K-lab flow conditioners. Mattingly et al. [5] studied the effect of distorted profile caused by the elbow upstream of the orifice meters and the influence of the tube bundle straightener installed between $3.8D$ and $5.7D$ from the bend outlet. Experiments were conducted using a single and double elbow configurations to generate the swirl and velocity profiles were measured with a Laser Doppler Velocimeter (LDV). Their results indicated that the investigated flow conditioner could remove swirl, but it might introduce errors in flow measurement. It was recommended that flow conditioners and flow meters should be considered as one unit and calibrated together. Kinghorn et al. [6] evaluated effectiveness of the Etoile straightener of different lengths in removing swirl upstream of the orifice plate. The swirl was generated by a vane damper control valve. It was found that the minimum length of the Etoile straightener

should be $1D$ to remove the swirl and the minimum installation distance of the straightener upstream of the flow meter should vary between $5D$ to $14D$ to ensure an error of less than ±0.5%. Ouzzane et al. [7] investigated the effects of swirling velocity profiles on the operation of an orifice flow meter with and without the NEL flow conditioner where the swirl was generated by the ball valve. It was proved that the swirl disappeared at the distance of $2.5D$ and a fully developed profile was still asymmetrical at shorter distances than $4.5D$. Ouzzane et al. [7] concluded that the NEL plate was a good flow straightener, but an inefficient flow conditioner in short installations. Laribi et al. [8] compared the effectiveness of three flow conditioners, the Etoile, the tube bundle and the Laws perforate plate downstream of a double 90-degree bend. The LDA was used for measurements. The decay of the swirling turbulent pipe flow downstream of three flow conditioners and their effect on accuracy of the different orifice diameter to pipe diameter ratios (β) were examined. The result of the experimental study showed that all three conditioners gave good measurement performance at the minimum distance of $12D$ and $13.5D$ downstream of the double bend for β = 0.5 and β = 0.62, respectively. For β = 0.7 the smallest discharge coefficient error was observed for the Etoile straightener at $7.5D$. It was concluded that the discharge coefficient errors of 0.5% caused by swirl were unavoidable for flow conditioners at distances less than $12D$. Hogendoorn et al. [9] analysed the effects of ISO tube bundle and the Etoile flow straighteners on flow profile disturbances and turbulence intensity in the experimental test rig and measurements were carried out by means of Laser Doppler Anemometry (LDA). Hogendoorn et al. [9] concluded that the ultrasonic flowmeter had better measurement performance when using the ISO tube bundle than the Etoile flow straightener.

Comprehensive numerical research have been focused on finding the proper turbulence model to predict the swirling flow so that the numerical simulations can become a valuable tool to evaluate the effectiveness of a flow conditioner. Erdal et al. [10] investigated experimentally and numerically flow through the K-lab/Laws flow conditioner with different upstream pipe bend configurations at Re = 2×10^5. Three different $k-\varepsilon$ models were used to predict the flow by comparing the results with LDV measurements in a test rig facility. Erdal et al. [10] concluded that the modified Chen-Kim $k-\varepsilon$ model had the best agreement with experiments downstream of the plate and at the same time instructed to employ more advanced turbulence models to improve the flow predictions. The decay of the inlet swirl intensities is confirmed by numerical simulations of Vaidya et al. [11]. Vaidya et al. [11] conducted direct numerical simulations by using rotating honeycomb to generate disturbances and investigated the swirl behaviour at Re = 1730. They found the dependency of swirl decay on the inlet swirl intensity showing that the increasing inlet swirl intensity leads to a quicker decay of the swirl downstream of the pipe. Kim et al. [12] used the $k-\varepsilon$ RNG turbulence model to examine the swirl intensity downstream of the 90-degree pipe bend. It was found that when moving downstream of the pipe bend, the swirl decayed and subsided faster as the curvature radius was larger. Furthermore, it was found that the swirl intensity

is insensitive to the varying Reynolds number in the range of $5\times10^4 \leq \mathrm{Re} \leq 2\times10^5$. Tamrina et al. [13] compared two turbulence models to predict the velocity distributions of the swirling flow in the pipe and discovered that Reynolds Stress Model gave better agreement with experimental data than the standard $k-\varepsilon$. Yehia et al. [14] studied swirling turbulent flow through the Zanker plate in a straight pipe using CFD simulations. Yehia et al. [14] found that the Detached Eddy Simulation (DES) gave the best agreement with ISO pressure drop correlation compared with other investigated models and this model was used for further research to study the effects of the plate thickness on the flow behaviour. It was proved that the swirl angle and tangential velocity decrease with the increasing plate thickness. Hallanger [15] conducted CFD analysis to assess the influence of flow conditioners on liquid ultrasonic flow meter used on the Oseberg Sør platform where Norsk Hydro experienced unstable velocity profiles in an oil metering station. Numerical simulations with employed $k-\omega$ turbulence model revealed that the problem was caused by the insufficient distance between the existing seven-pipe tube bundle conditioner and the ultrasonic meter installed downstream. The results showed that the more stable flow was achieved when the tube bundle was replaced with the Etoile straightener. As a result, Norsk Hydro substituted the tube bundle with the Etoile flow straightener to fulfil the NPD (Norwegian Petroleum Directorate) requirements. Askari et al. [16] developed a CFD model using academic COMSOL software to investigate the performance of the perforated flow conditioners, Mitsubishi and Spearman flow conditioners. The model was validated using experimental data of Spearman et al. [17] and gave good prediction of the flow behaviour. Thus, it was concluded that a new CFD model can be used for simulating the flow through the flow conditioners of different geometries.

Although flow straighteners have been used for decades, there is a considerable room for improvement and further research shall be conducted to define the geometry that would bring the optimum performance. The main goal is to maximize the swirl mitigation, obtain more stable velocity profile and minimize the length downstream of the source of the flow disturbance. Flow straightener used in the present study consists of a honeycomb with hexagonal opening pattern and is inserted downstream of a 90-degree circular pipe bend. The turbulent flow through the pipe bend with the honeycomb straightener is investigated by carrying out the numerical simulations using the Reynolds-Averaged Navier–Stokes (RANS) turbulence model. Due to the best performance of the Explicit Algebraic Reynolds Stress Model (EARSM) for predicting the turbulent flow through the orifice plate as reported by Jurga et al. [18] and further employment of the model to simulate the flow through a 90-degree pipe bend by Jurga et al. [19], the EARSM is also adopted in the present study to resolve the Reynolds stresses. Also, since the flow metering process is closely related to the flow conditioning, it is reasonable to stick to the same model and keep continuity of the EARSM application for further research. Therefore, the EARSM turbulence model is used to evaluate the effects of the honeycomb at the different distances from the bend outlet (Lb) and different values of

the honeycomb thickness (t) for the numerical simulations of the turbulent flow. The geometry of the honeycomb is changed by adjusting the honeycomb thickness to pipe diameter ratio, t/D, between 0.1 and 1 and the investigated distance from the bend outlet to pipe diameter ratio, Lb/D, for 1, 3 and 5. The flow characteristics evaluated in the present study are the axial velocity profiles, the swirl intensity, vorticity and streamline patterns.

5.2. Mathematical formulation and numerical method

Flow model and numerical methods used in this study are referred to the previous research papers reported by Jurga et al. [18] and [19] as described in Sections 3.2.1 and 4.2.1 of Chapters 3 and 4, respectively.

5.3. Computational setup

5.3.1. Computational domain

In order to form the fully developed turbulent velocity profile as the inlet for the pipe bend with the flow conditioner simulations, the precursor simulation of the straight pipe is performed and follow the computational domain setup of Jurga et al. [19]. The computational domain for the pipe bend with the flow conditioner is illustrated in Figure 5.1. The pipe diameter is set as D = 1m and the cross-section area across the fitting remains constant. The distance between the inlet of the pipe and the bend inlet is set to Lu = 10.6D and the distance between the bend outlet and the pipe outlet is set to Ld = 25 D. The curvature radius to pipe diameter ratio defined as the curvature ratio, Rc/D, is set to 1.42 for the convergence and validation study, as per the experiment of Erdal et al. [10]. According to Jurga et al. [19], the velocity profile becomes highly deformed and complex for $Rc < 2$ so the minimum considered value for the curvature ratio for the parametric study is set to Rc/D = 2. The cross-sectional shape of the studied honeycomb straightener is of regular hexagonal pattern. One of the key factors in the design process is the honeycomb porosity defined as the ratio between the actual flow cross-section area and the total cross-section area which is set to 93% in the present study. The honeycomb thickness to pipe diameter ratio denoted as t/D and the honeycomb distance from the bend outlet to pipe diameter ratio denoted as Lb/D are set to 0.123 and 5, respectively, for the convergence and validation study as per the experiment of Erdal et al. [10]. For the parametric study, t/D and Lb/D are investigated in different configurations to assess the effectiveness of the flow conditioner. The results of convergence study in Section 5.3.2, validation study in Section 5.3.3 and parametric study in Section 5.4 are described referring to the definition of planes presented in Figure 5.2.

The turbulent velocity profile obtained from the precursor simulation of the straight pipe is used as the inlet boundary condition for the simulations of the pipe bend with the flow conditioner for the mesh convergence study, validation study and parametric study at Re

= 2×10^5. The inlet values of the turbulent kinetic energy (k) and the specific turbulence dissipation rate (ω) for the simulations of the pipe bend with the flow conditioner are implemented from the results of the precursor simulation at the outlet of the straight pipe. The pressure is set as the zero normal gradient at the inlet of the pipe bend. At the outlet of the pipe bend, the three velocity components and the variables of k and ω are set as the zero normal gradient. Also, the reference pressure is set as zero at the outlet of the pipe bend. The surface of the 90-degree pipe bend and the flow conditioner walls are assumed to have a no-slip boundary condition, prescribed for the velocity components with (u, v, w) = (0,0,0).

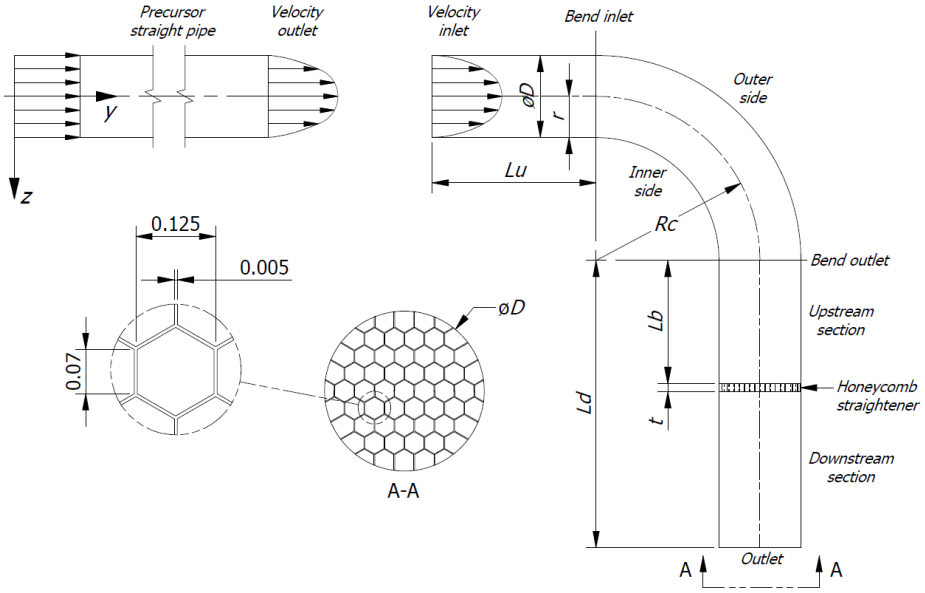

Figure 5.1. The computational domain topology for the pipe bend simulations with the honeycomb straightener.

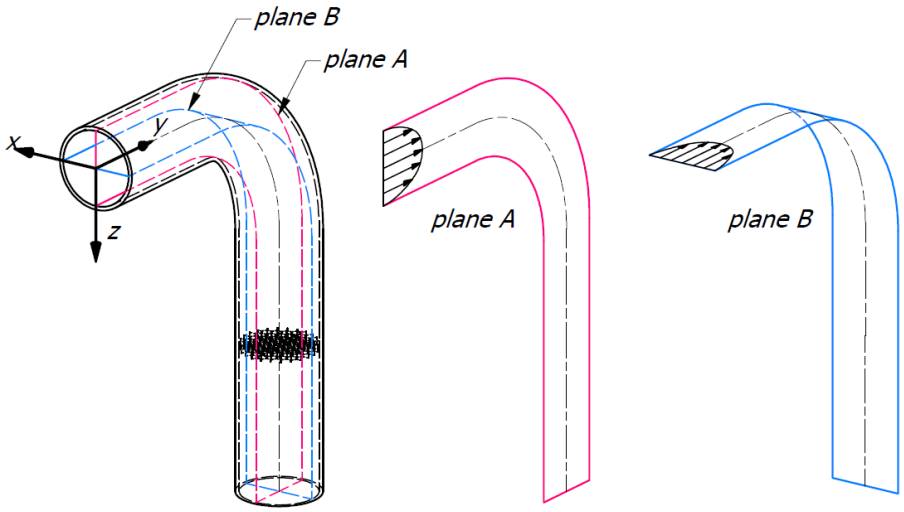

Figure 5.2. Location of the origin of the coordinate system and definition of planes A and B used in the convergence, validation and parametric study.

5.3.2. Convergence study

The grid convergence study is performed to ensure that grid-independent solution is achieved. A set of three meshes for the pipe bend of Rc/D = 1.42 and the honeycomb of t/D = 0.123 and Lb/D = 5 for Re = 2×10^5 is generated using a constant refinement factor of 2 in the pipe axis direction: the coarse, medium and fine meshes denoted as M0, M1 and M2, respectively. As presented in Figure 5.3, the values of y^+ (y^+ is defined as $y^+ = \Delta y u_*/\nu$, where u_* is the wall friction velocity, Δy is the distance between the wall and the centre of the first grid above the wall and ν is the kinematic viscosity) are much bigger than 1 and the maximum ones are located at the honeycomb walls at the plate edge. Since the $y^+ > 30$, the Spalding's wall function is applied to capture flow characteristics within the entire range of the y^+, i.e., within the viscous sub-layer and in the log-law region. The resulting numbers of cells and average values of the y^+ for different meshes are presented in Table 5.1. The thickness of the first grid layer adjacent to the wall is $0.0002D$ for all studied meshes. In order to investigate the mesh convergence, the distributions of the normalized axial velocity profiles in plane A upstream and downstream of the honeycomb are presented in Figure 5.4. The axial velocity profile is scaled with the bulk velocity to get non-dimensional property. In general, a good agreement is found between the results achieved for the meshes M1 and M2 at the bend location of $\alpha = 45^0$ and all the examined locations downstream of the honeycomb. An obvious difference in the velocity profiles for the fine mesh of M2 near the inner side of the pipe bend at $\alpha = 90^0$ and at the distance z/D = 2.5 upstream of the honeycomb is observed due to the flow separation. Based on the obtained results, it is believed that M1 can be considered as a favourable balance between the computational cost and discretization error so that the grid resolution of M1 is used for the further simulations of the present study. An example of the mesh M1 and the direction of the cell size growth is shown in Figure 5.5.

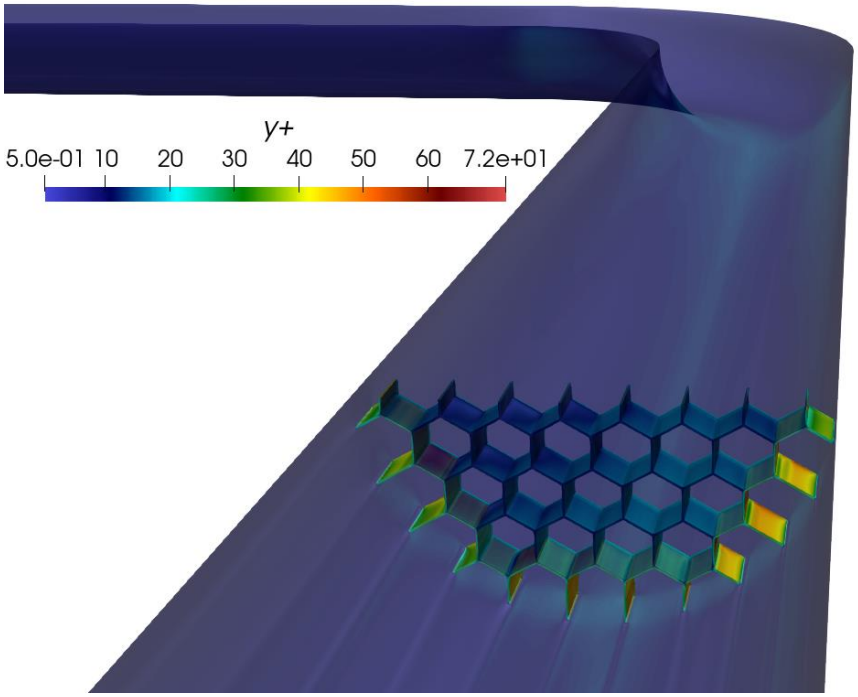

Figure 5.3. The distribution of y+ at the flow domain walls in the 3D view of the cutting plane y-z

Table 5.1. Mesh resolutions investigated in the mesh convergence study

Mesh	Number of cells	average y^+
M0	6020800	16.851
M1	11540224	14.419
M2	22633184	12.518

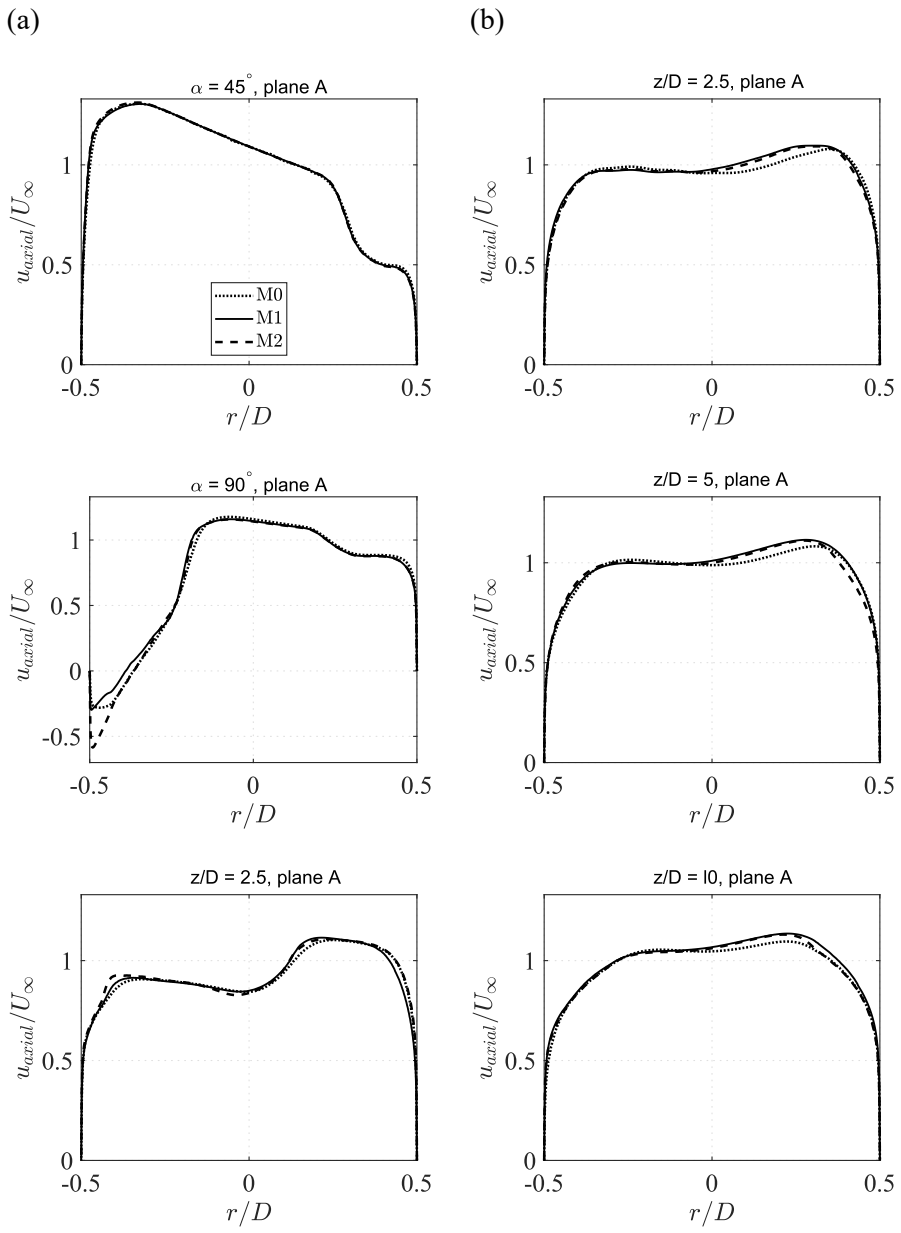

Figure 5.4. The normalized axial velocity profiles (a) upstream and (b) downstream of the honeycomb in plane A for Re = 2×10^5 and Rc/D = 1.42 for the investigated mesh density variants.

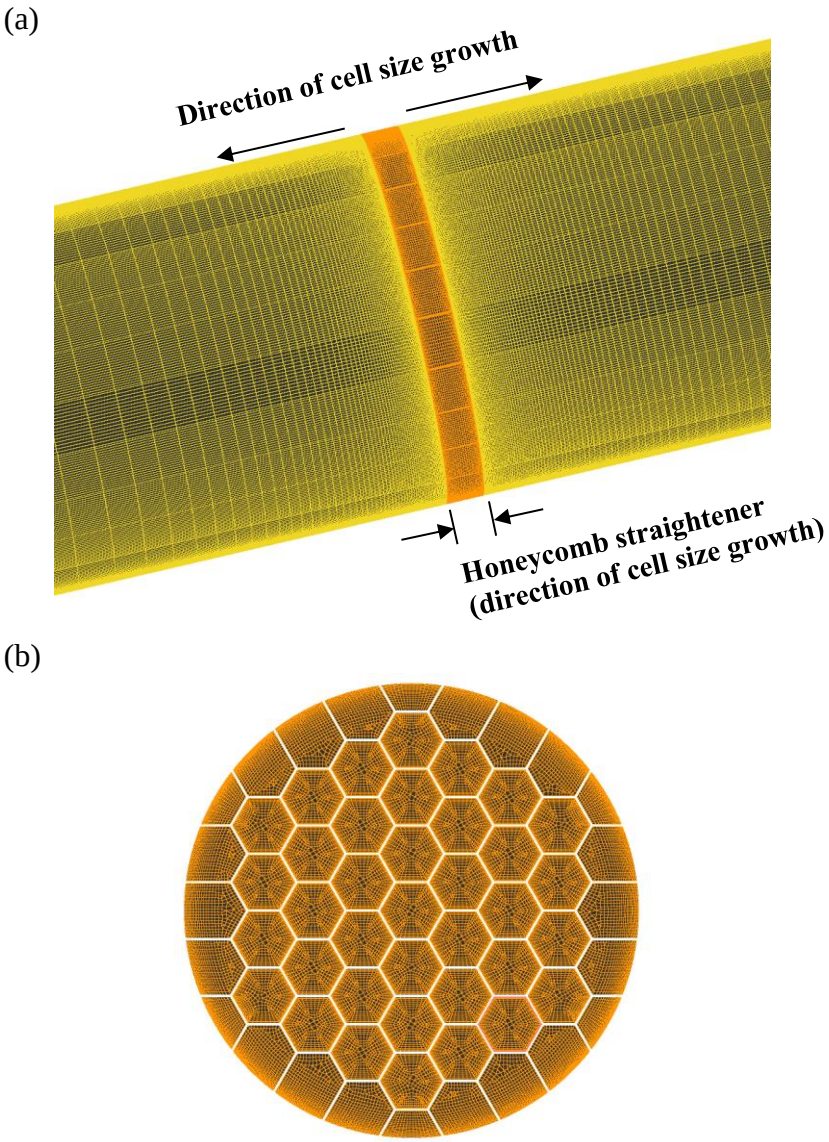

Figure 5.5. An overview of the computational mesh M1 with the honeycomb straightener: (a) meshing of the total volume, (b) cross-sectional view of the honeycomb flow domain.

5.3.3. Validation study

The results of the numerical simulation using the same grid resolution as the mesh M2 described in Section 5.3.2 are compared with the experimental data of Erdal et al. [10] for the K-Lab/Laws flow conditioner inserted in the 90-degree pipe bend. The goal of the comparison is to validate the present adopted numerical model to capture the crucial behaviour of the turbulent flow through the flow conditioner installed downstream of the pipe bend. Erdal et al. [10] carried out the experiment by means of LDV to measure the velocity profiles upstream and downstream of the flow conditioner at Re = 2×10^5 and $Rc/D = 1.42$. The K-Lab/Laws flow conditioner, introduced by Laws [3], consists of 19 holes of unequal size distributed in radial rings with the minimum thickness of $D/8$. The

geometry of the K-Lab/Laws and overview of the computational mesh used for the validation study are presented in Figure 5.6 and Figure 5.7, respectively.

The normalized axial velocity profiles in plane A and B at different positions upstream and downstream from the flow conditioner, z/D, presented in Figure 5.8 and Figure 5.9, are compared with the experimental data reported by Erdal et al. [10]. The ordinate in Figure 5.8 and Figure 5.9 is offset by 0.5 units. There is a slight difference observed in agreement between the results upstream and downstream of the K-Lab/Laws. In Figure 5.8, the measurement is performed midway between the bend outlet and the conditioner, at z/D = 2.5. Although relatively small deviations from the experimental curve near the middle of the pipe, the velocity profiles show a decent agreement with the LDV measurements reported by Erdal et al. [10]. On the other hand, in Figure 5.9, downstream of the K-Lab/Laws, the axial velocity profiles exhibit similar shapes to the experimental data. It can be concluded that the present model performs well in predicting the axial velocity profile of the flow and is used in the parametric study in Section 5.4.

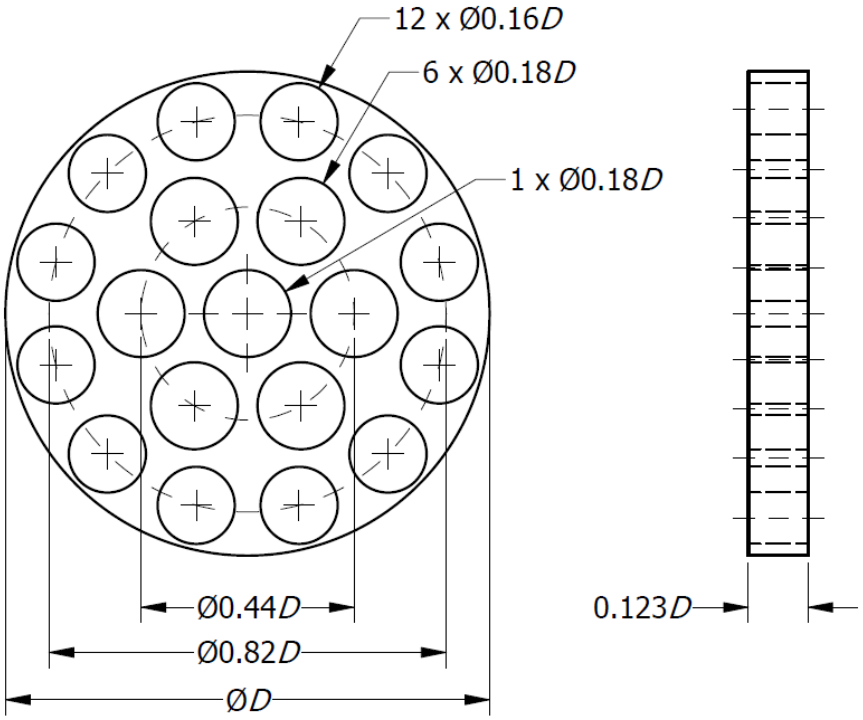

Figure 5.6. The computational domain topology of the K-Lab/Laws flow conditioner used for the validation study.

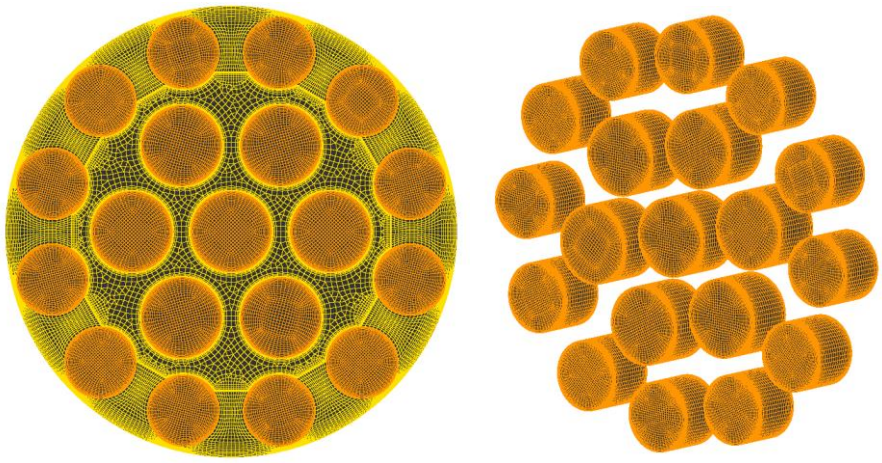

Figure 5.7. An overview of the computational mesh with the flow conditioner K-Lab/Laws used for the validation study: (a) cross-sectional view of the total volume, (b) 3D view of the K-Lab/Laws flow domain.

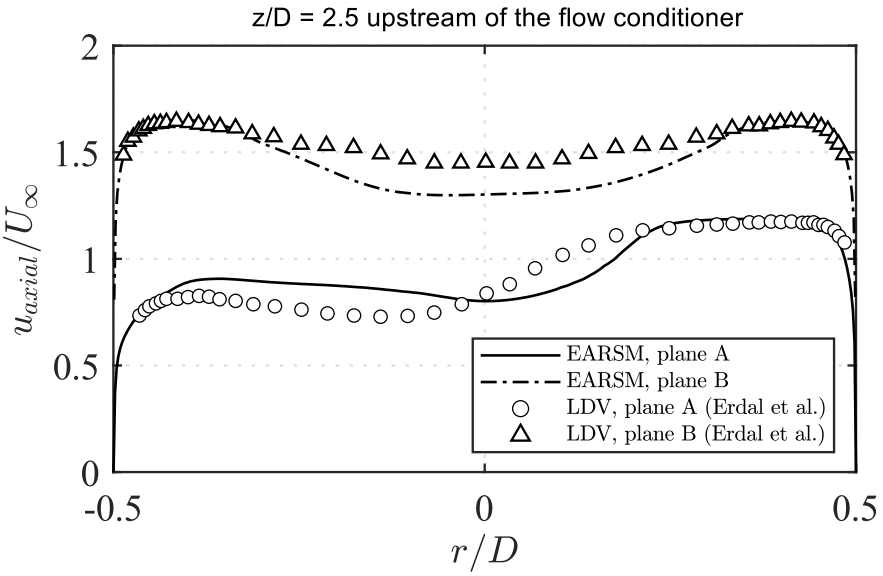

Figure 5.8. The normalized axial velocity profiles in plane A and B at z/D = 2.5 upstream of the honeycomb for Re = 2×10^5 and Rc/D = 1.42 compared with the experimental data reported by Erdal et al. [10].

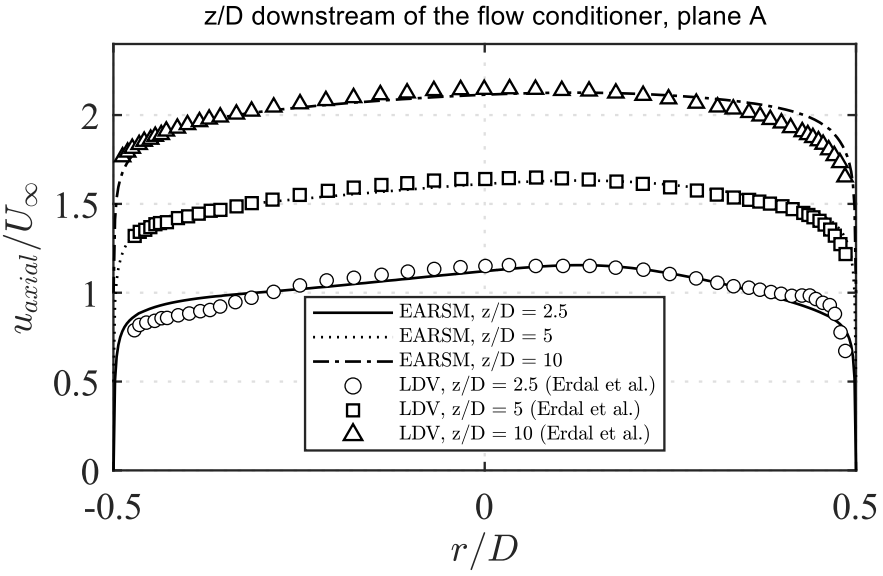

Figure 5.9. The normalized axial velocity profiles in plane A at different z/D downstream of the honeycomb for Re = 2×10^5 and Rc/D = 1.42 compared with the experimental data reported by Erdal et al. [10].

5.4. Results and discussion

5.4.1. Influences of the honeycomb distance from the bend outlet

A parametric study is carried out for different locations of the honeycomb from the bend outlet: Lb/D = 1, 3 and 5, for the honeycomb thickness fixed: t/D = 0.1, at Re = 200000 and Rc/D = 2. The magnitude of the velocity on the y-z plane is presented in Figure 5.10 together with the pipe bend without honeycomb to view the influence of the honeycomb. The honeycomb reaccelerates the flow close to the inner wall of the pipe where the backflow develops due to the bend. However, it can be clearly observed that when the honeycomb is placed at the closest distance from the bend outlet (Figure 5.10 b), the flow profile is more distorted than that in case without the honeycomb. The smooth flow is achieved when the honeycomb is installed at the further distance from the bend outlet, at $Lb/D = 5$. However, at first glance, there is no significant difference in the magnitude of the velocity between the honeycomb at $Lb/D = 5$ and that in case without the honeycomb. Therefore, a more detailed investigation is performed to achieve a better understanding of the flow straightening mechanism. The normalized axial velocity profiles are studied at three locations downstream of the honeycomb, at the distances $z/D = 6$, 10 and 15 measured from the bend outlet. The velocity profiles are compared with those of the straight pipe and the 90-degree pipe bend without the honeycomb. The obtained normalized axial velocity profiles in plane A and B are presented in Figure 5.11. It is shown that for the honeycomb placed closest to the bend outlet, at $Lb/D = 1$, the velocity profiles are deviating the most from the fully developed flow between the inner and outer side, in contrast to the other honeycomb positions. Although the discrepancies caused by $Lb/D = 1$ weaken along the flow, they still show poor performance when

compared to the pipe bend without honeycomb. In Figure 5.11, at the distance of $z/D =$ 6 from the bend outlet, the axial velocity profiles for $Lb/D = 1$ and $Lb/D = 3$ display the two-peak distributions, where the flow is accelerated close to the inner side of the bend, slightly deaccelerated in the middle and considerably more accelerated near the outer side in plane A. Also, the peaks of the axial velocity for $Lb/D = 1$ and 3 shift towards the outer side. Figure 5.11 shows that for $Lb/D = 5$, the flow pattern oscillates at the level of the pipe bend without honeycomb velocity profile, between the inner and outer side of the bend. This fluctuating behaviour happens due to the strong jet flow which occurs right after passing through the honeycomb bores, creating the flow separation at the measurement distance, z/D = 6, which is very close to the back face of the honeycomb. However, with the increasing z/D, the oscillations disappear, as depicted in Figure 5.11 for z/D = 10 and 15. Also, with the increasing z/D and Lb/D, the two-pick distributions get smoother and the velocity profiles tend to become flat around the pipe centerline. It is observed that the honeycomb installed at the investigated positions cannot recover a non-distorted velocity profile in the straight pipe. Nevertheless, the honeycomb with the distance of Lb/D = 5 at z/D = 15, in Figure 5.11, shows the best agreement with the fully developed velocity profile in the straight pipe and thus shows better performance than the pipe bend without honeycomb.

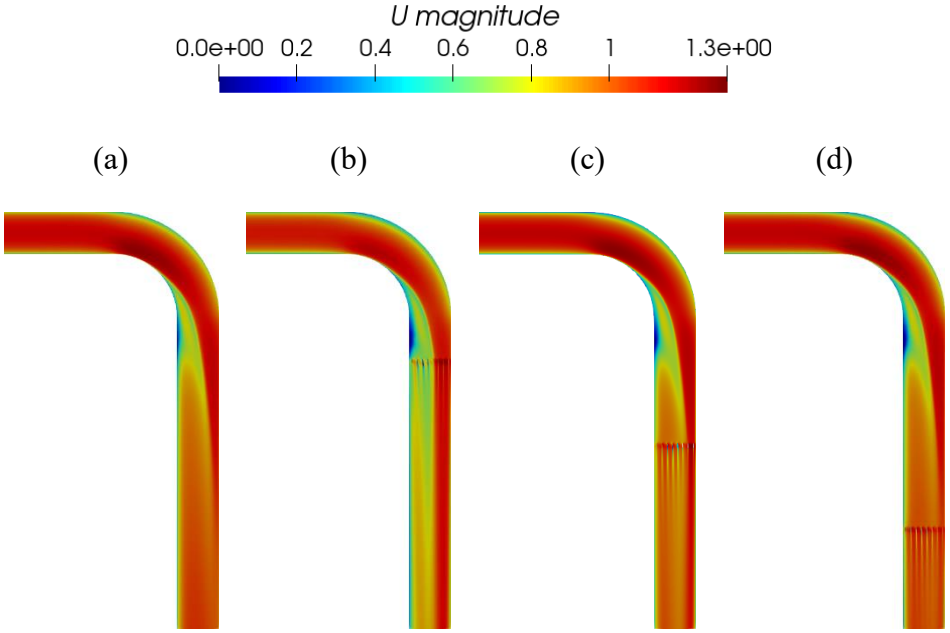

Figure 5.10. The magnitude of the velocity in plane A for (a) the pipe bend without the honeycomb and (b), (c) and (d) with the honeycomb at locations: $Lb/D = 1$, $Lb/D = 3$ and $Lb/D = 5$, respectively, for the honeycomb thickness fixed, t/D = 0.1.

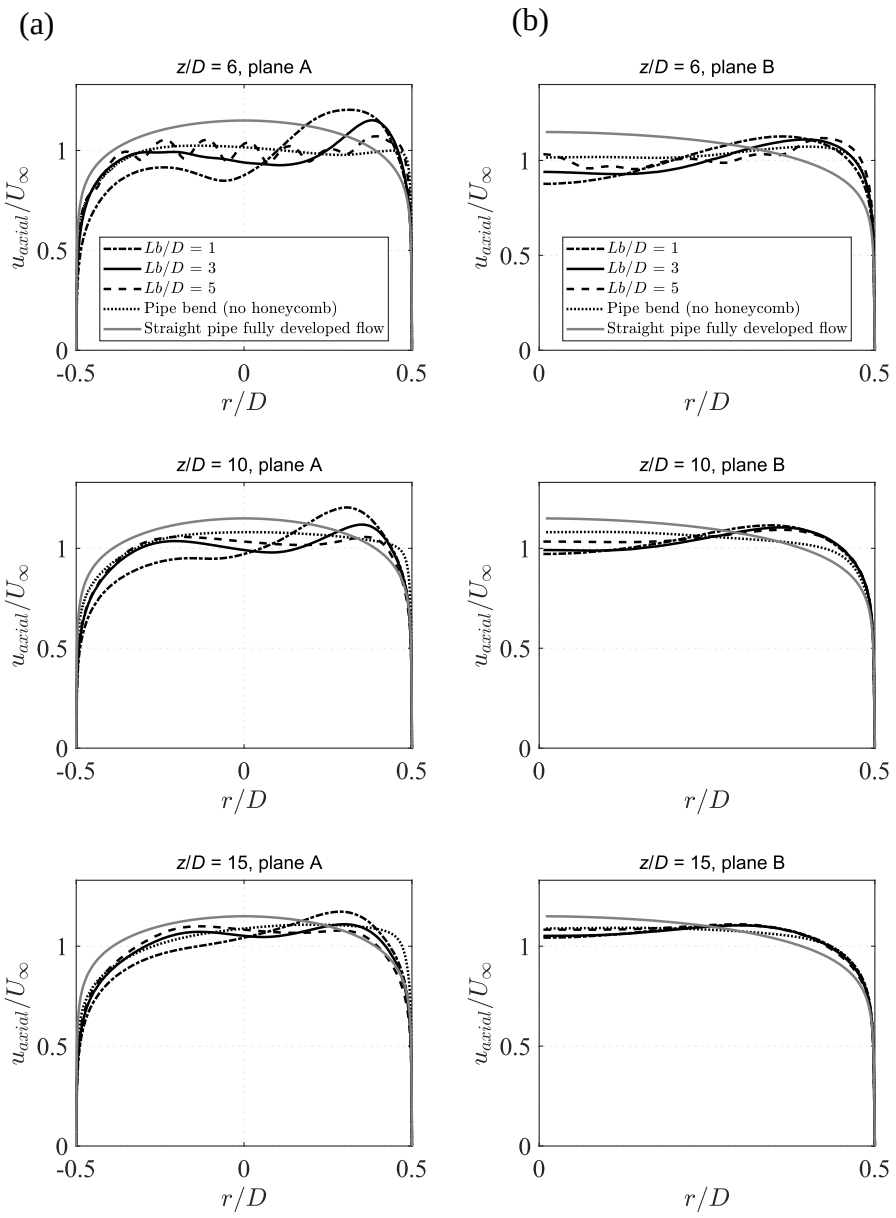

Figure 5.11. The normalized axial velocity in (a) plane A and (b) plane B at $z/D = 6$, 10 and 15 downstream of the bend outlet for different locations of the honeycomb, Lb/D, compared with the velocity profile of the pipe bend and the straight pipe.

Another important parameter used to evaluate the effectiveness of the flow conditioners is the swirl intensity. The swirl intensity has been calculated according to the definition in Equation (5.1) used by Kim et al. [12] for the elbow flows:

$$I_s = \frac{\int [\vec{U} - (\vec{U} \cdot \hat{n})\,\hat{n}]^2 \, dA}{U_b^2 \int dA} \tag{5.1}$$

where I_s is the normalized swirl intensity, $\vec{U}$ is the vector of the flow velocity, $\hat{n}$ is a unit vector normal to the area of the pipe section, U_b is the mean axial velocity and A is the

area of the pipe section. The swirl intensity is normalized by the value of intensity at the location of the bend outlet. The normalized swirl intensity is investigated in the downstream region of the 90-degree pipe bend with the honeycomb straightener placed at the locations of Lb/D = 1, 3 and 5 from the bend outlet and presented in Figure 5.12. The results are plotted in logarithmic scale on I_s-axis in order to clearly see the distinction between examined honeycomb distances compared with the pipe bend without honeycomb. It can be observed that the swirl intensity generated by the pipe bend with and without flow conditioning displays the same characteristics at the distance between the bend outlet and the front face of the honeycomb. However, when passing through the honeycomb straightener, there is a sudden jump of the swirl intensity when the flow enters the honeycomb straightener and a sudden drop at the exit of the honeycomb when the strong jet flows out of the honeycomb bores. Then, the value of I_s decays exponentially and almost completely disappear along the axis, whereas the swirl intensity of the pipe bend without the honeycomb steadily declines linearly at the higher values of I_s. The values of I_s show similar trends of exponentially decay for all different locations of the honeycomb. However, with the increasing Lb/D, the swirl intensity considerably decays at shorter distances from the bend outlet. In other words, it subsides much more quickly for Lb/D = 5, whereas for Lb/D = 1, it persists for a longer distance downstream of the pipe before it levels out.

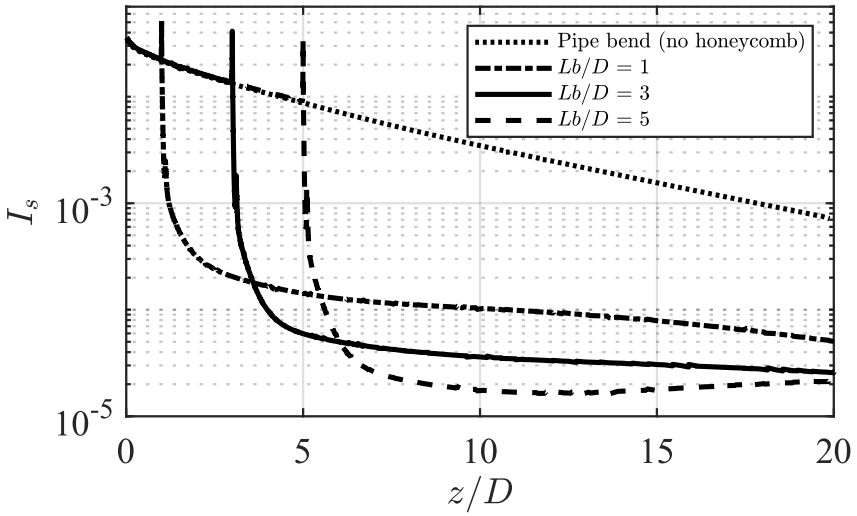

Figure 5.12. The normalized swirl intensity, I_s, along the pipe for different locations of the honeycomb from the bend outlet, Lb/D.

Figure 5.13 shows the pipe cross-sections oriented normal to the axial direction of the pipe to visualize the contours of the axial vorticity, ω_{axial}, measured at three locations: z/D = 6, 10 and 15 downstream of the bend outlet. The results of the pipe without the flow straightener and the pipe with the flow straightener installed at three different positions: Lb/D = 1, Lb/D = 3 and Lb/D = 5 are also included for comparison. The

axial vorticity refers to the vorticity component in the axial direction of the pipe that is perpendicular to the plane of the flow, and it is scaled by U/D to get the non-dimensional physical property. The left side of each cross-section corresponds to the inner side of the pipe bend and the right side of each cross-section corresponds to the outer side of the pipe bend, as shown in Figure 5.1. The influence of the honeycomb straightener on the fluid behaviour is obvious when comparing Figure 5.13 (a) with the rest of the cases in Figure 5.13 (b) (c) and (d). The two strongest counter-rotating axial vortices referring to the secondary flow or Dean vortices discussed by Jurga et al. [19] is obviously noticed for the pipe bend without the honeycomb, in Figure 5.13 (a), due to the strong flow deformation caused by the pipe curvature. The two regions of the strong axial vorticity stay symmetric with respect to the geometric plane of symmetry. As depicted in Figure 5.13 (b), (c) and (d), the vorticity gets immediately weaker and almost fades away when the honeycomb is installed with the increasing Lb/D. However, there is still pronounced axial vorticity attached to the pipe wall due to the large velocity gradient within the pipe flow boundary layer. There are also two visible regions of the weak vorticity, concentrated at the inner side of the pipe, which get smaller for the increasing Lb/D. For Lb/D = 5 at $z/D = 15$, the extension of the vorticity decreases the most.

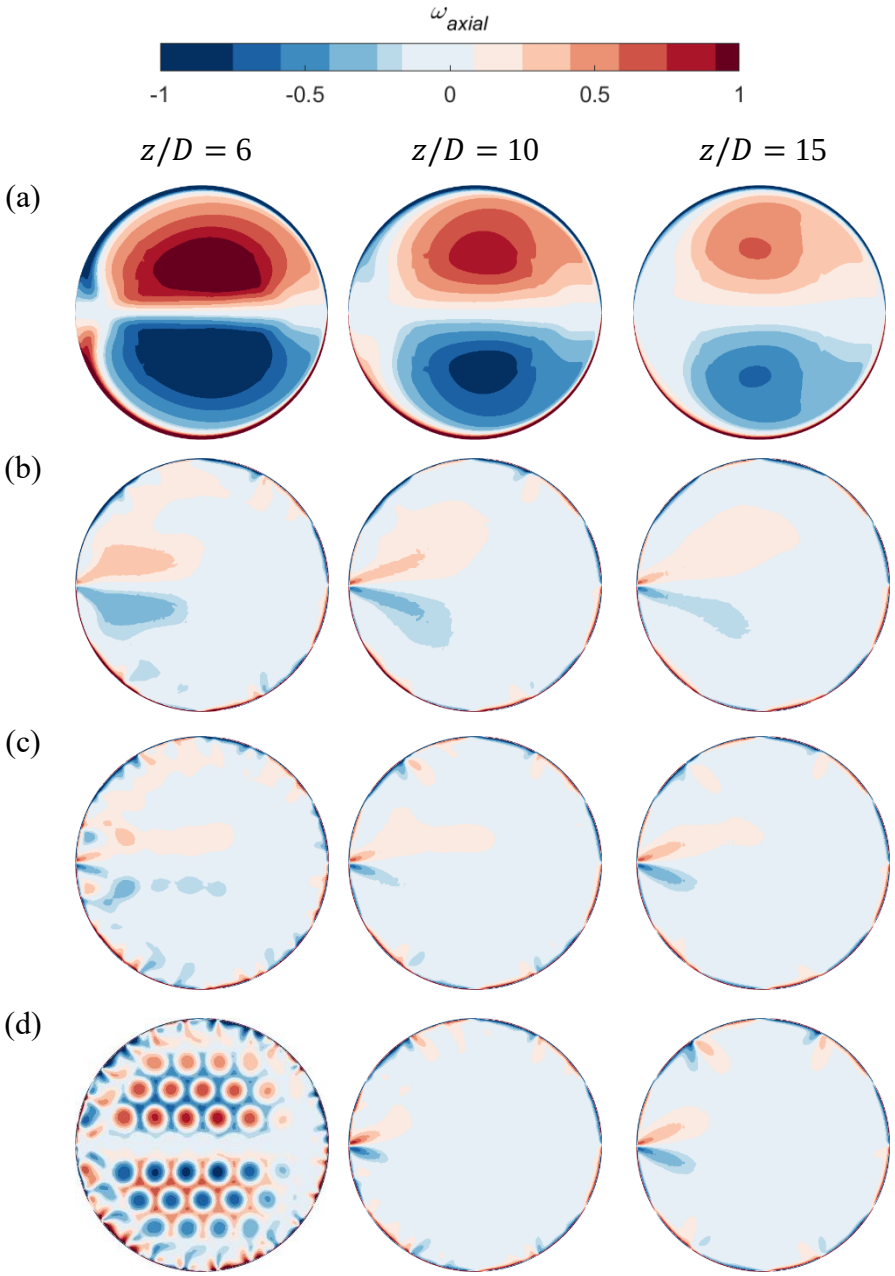

Figure 5.13. The normalized axial vorticity for (a) the pipe bend without the honeycomb and (b), (c) and (d) with the honeycomb at locations: $Lb/D = 1$, $Lb/D = 3$ and $Lb/D = 5$, respectively.

The flow streamlines in the pipe bend, before and after inserting the honeycomb straightener, is presented in Figure 5.14 by 3D views of velocity streamlines coloured with contours of the vorticity magnitude. The chaotic and swirling flow pattern, observed in Figure 5.14 (a), starts at the bend and proceeds towards the downstream of the pipe. It is visualized by the highly distorted velocity streamlines and the large value of vorticity magnitude, due to the sudden change of the flow direction through the bend. The effect of the honeycomb presence is clearly seen right after passing through the honeycomb, in

Figure 5.14 (b), (c) and (d). The swirl is immediately eliminated and the streamlines become straight and smooth. The vorticity magnitude gets weaker along the flow direction.

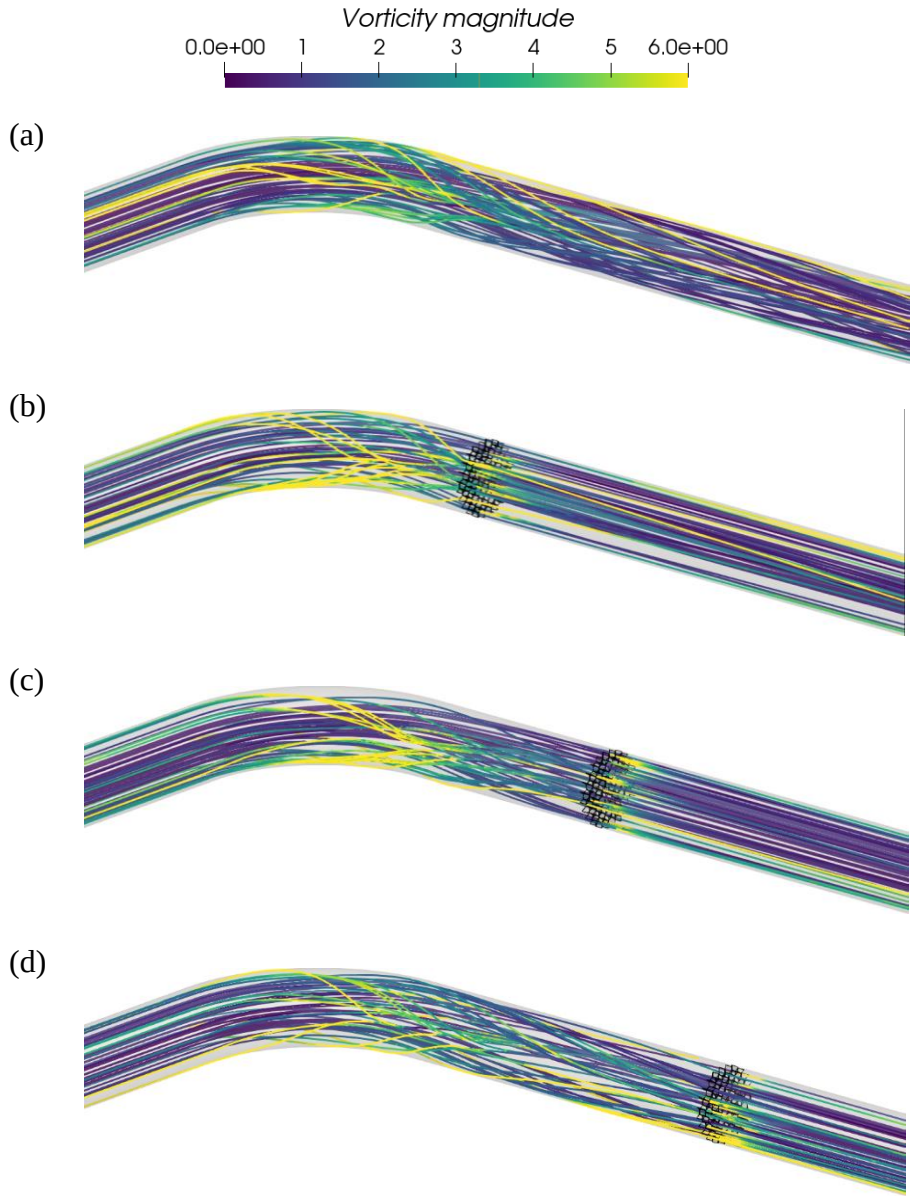

Figure 5.14. Velocity streamlines colored with vorticity contours for (a) the pipe bend without the honeycomb and (b), (c) and (d) with the honeycomb at locations: $Lb/D = 1$, $Lb/D = 3$ and $Lb/D = 5$, respectively.

5.4.2. Influences of the honeycomb thickness

For the further parametric study, the pipe bend with the honeycomb at the shortest and longest examined distance of Lb/D = 1 and Lb/D = 5, respectively, are chosen to evaluate the effects of the honeycomb thickness on the flow behavior in the downstream section. The honeycomb thickness is in the range of t/D = 0.1 to 1. The magnitude of

the velocity on the y-z plane for the different honeycomb thickness is presented in Figure 5.15. It can be clearly observed that when the honeycomb thickness is increased from t/D = 0.1 to t/D = 1 for both cases of Lb/D, it does not significantly affect the flow pattern. In Figure 5.15 (a) for Lb/D = 1, the flow is deformed in the same way and shows no obvious improvement regardless the honeycomb thickness. Also, similarity is found at the further installation distance, in Figure 5.15 (b) for $Lb/D = 5$, where the same smooth flow behind the honeycomb is present for both investigated thicknesses. In addition, the normalized axial velocity profiles for different honeycomb thicknesses are presented in Figure 5.16. The obtained velocity profiles are compared with those of the straight pipe and the 90-degree pipe bend without the honeycomb at three locations: $z/D = 7$, 10 and 15. It is clearly shown that all the curves for different t/D display similar shapes at all measured locations for both cases of Lb/D. In Figure 5.16 (a) where the honeycomb straightener is at the closet position from the bend outlet, the increased thickness to t/D = 1 maintains the disordered character of the velocity profile. The flow performs similarly worse than without honeycomb installation and thus keeps its deviation from the straight pipe velocity profile. There are also similar two-peak distributions with much accelerated region of the flow towards the outer side that subsides with increasing z/D. There is also no significant difference presented in Figure 5.16 (b) for the reviewed range of thicknesses for the case of Lb/D = 5. The oscillations observed for t/D = 1 at $z/D = 7$ are due to the jet flow out of the honeycomb that exists at the measurement point, at the near location to the honeycomb. With the increasing z/D, the trend of recovery to the straight pipe flow is observed without the influence of the honeycomb thickness.

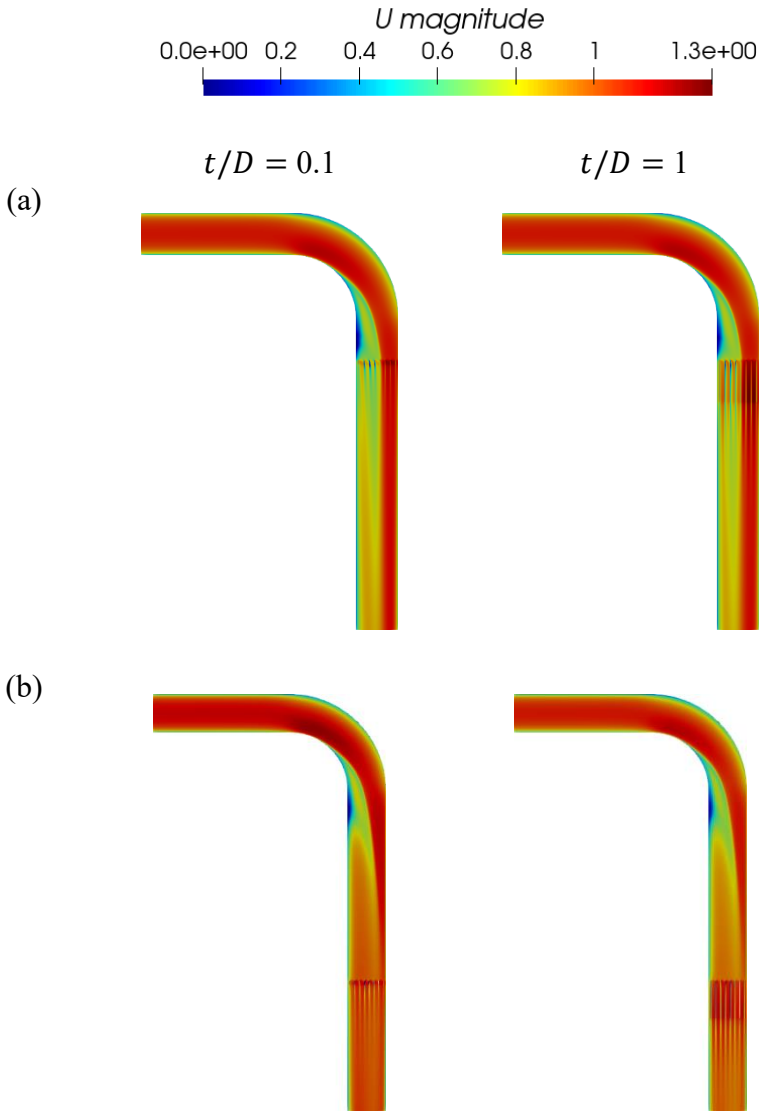

Figure 5.15. The magnitude of the velocity in plane A for the pipe bend with the honeycomb at (a) $Lb/D = 1$ and (b) $Lb/D = 5$, for the honeycomb thickness t/D = 0.1 and t/D = 1.

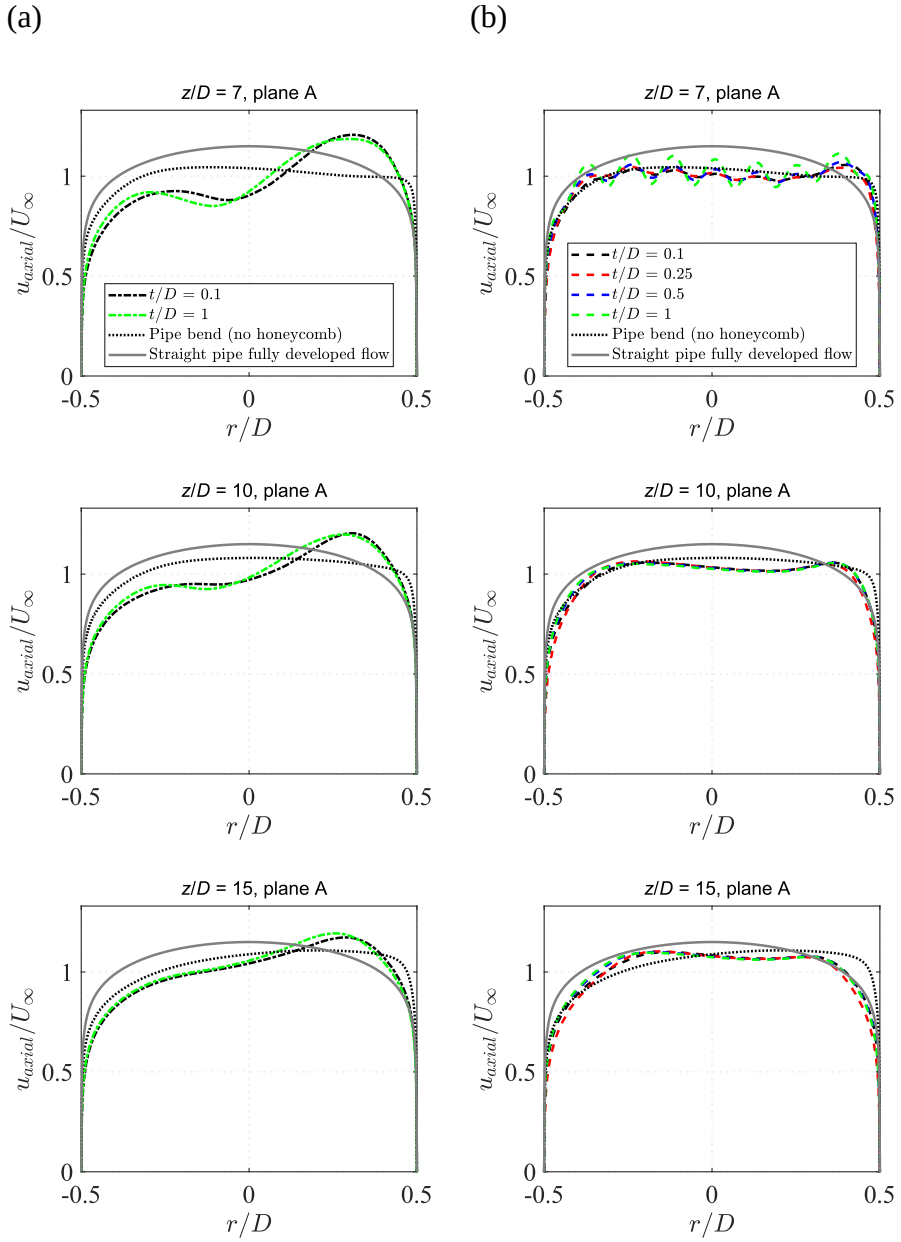

Figure 5.16. The normalized axial velocity for (a) $Lb/D = 1$ and (b) $Lb/D = 5$ in plane A for different honeycomb thicknesses, t/D.

In order to investigate closely the effects of the different honeycomb thickness, the performance of the swirl intensity, I_s, is illustrated in Figure 5.17. It is observed similar exponential downward pattern of I_s, for the range of the honeycomb thickness, t/D between 0.1 and 1. The effect of the honeycomb with the Lb/D = 1 and t/D = 1 largely corresponds to the case of Lb/D = 5 and t/D = 0.1, where I_s approaches the value of 10^{-5} behind the honeycomb and at around z/D = 10 slightly increases. However, with the increasing t/D for Lb/D = 5, the swirl intensity drops even below $I_s = 10^{-5}$ at around z/D = 12. Since the two cases of t/D = 0.5 and t/D = 1 show similar I_s profile, the

former can be considered as the most effective one out of all scrutinized in this study, considering the manufacturing cost.

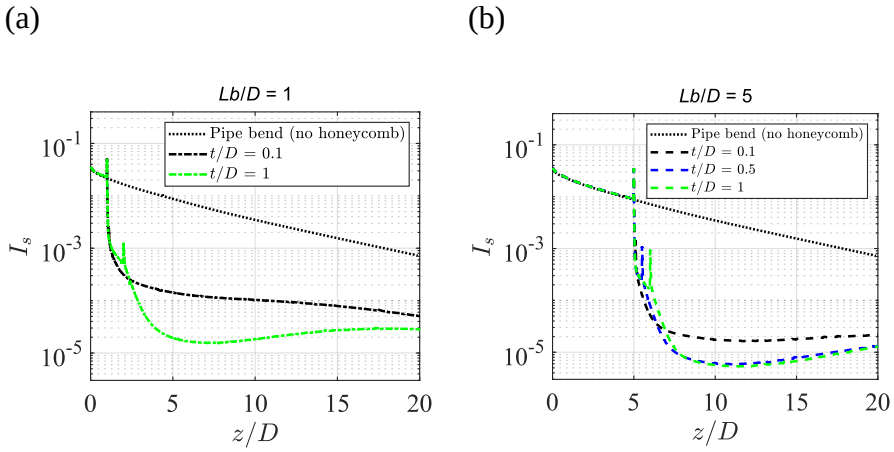

Figure 5.17. The normalized swirl intensity, I_s, along the pipe for (a) $Lb/D = 1$ and (b) $Lb/D = 5$ for different honeycomb thicknesses, t/D.

5.5. Conclusions

- Honeycomb straightener installed at the furthest considered distance from the bend outlet, $Lb/D = 5$, shows the best improvement in smoothing nonuniformities in the flow. The flow becomes smooth approximately at z/D = 15 measured from the bend outlet. It is important to mention that installing the honeycomb straightener closer to the bend outlet, i.e., $Lb/D = 1$, results in a more distorted flow profile than that observed in the corresponding bend geometry without the straightener. Based on these observations, it is recommended to place the flow straightener at the minimum distance of $Lb/D = 5$.
- The swirl intensity dissipates much earlier as the honeycomb installation distance behind the bend increases. It is found that at $Lb/D = 5$ the honeycomb straightener is the most successful in removing swirl in the flow through the pipe.
- The axial vorticity becomes the weakest and almost vanishes when the honeycomb is installed at the furthest considered distance from the bend outlet, Lb/D = 5. It is also proved, that the honeycomb can eventually make the flow straight, which is visualized by the velocity streamlines.
- The increase of the honeycomb thickness from t/D = 0.1 to 1 shows no significant influence on the axial velocity behaviour regardless the honeycomb installation distance, Lb/D.
- However, the different honeycomb thickness affects the swirl intensity behavior. The honeycomb thickness greater than or equal to 0.5, $t/D \geq 0.5$, is recommended for eliminating the swirl.

It is concluded that neither the studied distances of the honeycomb nor the thicknesses can make the honeycomb recover the velocity profile symmetry. Although the device does not fullfil the requirement of the flow conditioner, it removes the swirl effectively as specified by the flow straightener purpose in Annex C of ISO 5167. Based on the performed study, the optimum installation distance and thickness of the investigated honeycomb design can be chosen as $Lb/D = 5$ and $t/D = 0.5$, respectively. In the case of inserting the flow meter downstream of the honeycomb straightener, it is recommended that the minimum installation distance should be kept at $z/D = 15$ to ensure the most favorable measurement performance.

References

[1] ISO 5167-1:2003 Measurement of fluid flow by means of pressure differential devices inserted in circular cross-section conduits running full — Part 1: General principle and requirements.

[2] Baker, R. C., 2000. Flow Measurement Handbook: Industrial Designs, Operating Principles, Performance and Applications, Cambridge University Press.

[3] Laws, E. M., 1990. Flow conditioning—a new development. *Flow Meas. Instrum.*, 1(3), pp. 165-170.

[4] Bates, I. P., 1991. Field use of K-lab flow conditioner Proceedings of the North Sea Flow Measurement Workshop, Norwegian Society of Chartered Engineers.

[5] Mattingly, C. E. and Yeh, T. T., 1991. Effects of pipe elbows and tube bundles on selected types of flowmeters. *Flow Meas. Instrum.*, 2(1), pp. 4-13

[6] Kinghorn, F. C., McHugh, A. and Dyet, W. D., 1991. The use of etoile flow straighteners with orifice plates in swirling flow. *Flow Meas. Instrum.*, 2(3), pp. 162-168.

[7] Ouazzane, A. K. and Benhadj R., 2002. Flow conditioners design and their effects in reducing flow metering errors, Sensor Review, 22(3), pp. 223-231.

[8] Laribi, B., Wauters, P., & Aichouni, M., 2002. Experimental study of aerodynamic behavior downstream of three flow conditioners. In *Fluids Engineering Division Summer Meeting*, 36150, pp. 115-119.

[9] Hogendoorn, J., Boer, A. & Laan, D., 2005. Flow disturbances and flow conditioners: The effect on multi-beam ultrasonic flow meters.

[10] Erdal, A., Sivertsen, A. S., Langsholt, M. and Andersson, H. I., 1996. Three-dimensional computation of turbulent flow through a flow conditioner, Proceedings of the 8th International Conference on Flow Measurement, Flomeko '96, Beijing, China, pp. 718 – 723.

[11] Vaidya, H. A., Ertunc, O., Genc, B., Beyer, F., Koksoy, C. and Delgado, A., 2011. Numerical simulations of swirling pipe flows- decay, *J. Phys*., Conf. Ser. 318, pp. 062022.

[12] Kim, J., Yadav, M. and Kim, S., 2014. Characteristics of Secondary Flow Induced by 90-Degree Elbow in Turbulent Pipe Flow. *Eng. Appl. Comput. Fluid Mech*., 8(2), pp. 229-239.

[13] Tamrina, K. F., Sheikhb, N. A., Rahmatullaha, B., & Malim, T., 2016. Numerical analysis of swirl intensity in turbulent swirling pipe flows. *Sci. Eng.*, *78*(5-10), pp. 133.

[14] Yehia, A., Khalid, M. S., Hossam, S. A., & Jaafar, M. N., 2009. CFD analysis of incompressible turbulent swirling flow through zanker plate. *Eng. Appl. Comput. Fluid Mech.*, 3(4), pp. 562-572.

[15] Hallanger, A., 2002. CFD Analyses of the Influence of Flow Conditioners on Liquid Ultrasonic Flowmetering. In Oseberg Sor, a Case Study, North Sea Flow Measurement Workshop (Vol. 1).

[16] Askari, V., Nicolas, D., Edralin, M. & Jang, C., 2019. Computational Fluid Dynamics Model for Sensitivity Analysis and Design of Flow Conditioners. In *SIMULTECH*, pp. 129-140.

[17] Spearman, E.P., Sattary, J.A. & Reader-Harris, M.J., 1996. Comparison of velocity and turbulence profiles downstream of perforated plate flow conditioners. *Flow Meas. Instrum.*, 7(3-4), pp. 181-199.

[18] Jurga, A.P., Janocha, M.J., Yin, G., Giljarhus, K.E.T. and Ong, M.C., 2021. Validation and assessment of different RANS turbulence models for simulating turbulent flow through an orifice plate. *IOP Conf. Ser.: Mater. Sci. Eng.* 1201, pp. 012019.

[19] Jurga, A.P., Janocha, M.J., Yin, G. and Ong, M.C., 2022. Numerical simulations of turbulent flow through a 90-degree pipe bend. *J. Offshore Mech. Arct. Eng.* (Under review).

Chapter 6.

Conclusions

6.1. Summary of the key findings

The key findings based on the conclusions presented in Chapter 4, Chapter 5 and Chapter 6 are formulated below as the answers to the research questions posed in Chapter 1, Section 1.2.

Answer to the first research questions:

- The key flow parameters used to evaluate the behavior of eight different RANS turbulence models to investigate the turbulent flow through the orifice plate are the velocity distribution and the turbulence intensity.
- The best performance for simulating the fully developed turbulent flow through the orifice plate in a pipe is presented by the EARSM, the results of which are the closest to the published experiment.
- The discharge coefficient obtained by the EARSM turbulence model gives the best agreement with the ISO discharge coefficient when compared with the calculations of other investigated models.
- The EARSM outperforms other studied turbulence models in predicting the turbulent flow through the orifice plate which is proved by the excellent agreement with the experiments and the similarity to the ISO discharge coefficient.
- The EARSM's assumption of anisotropic Reynolds stress tensor is decided to be used for further research to study the effects of the pipe bend and flow conditioner on the flow behavior.

Answer to the second research questions:

- The key flow parameters used to evaluate the influence of the pipe curvature and Re on the behavior of the turbulent flow through the 90-degree pipe bend are the axial velocity, the velocity perturbation, the pressure difference and the vorticity.
- The pioneering usage of the EARSM turbulence model to resolve the Reynolds stresses in the pipe bend indicated better agreement with the experimental data than other turbulence models used so far in the published literature.
- The flow behavior at the pipe bend and downstream of the bend depends strongly on the curvature ratio of the bend (Rc/D), while the effects of the Re on the flow pattern are insignificant for the investigated range of Re from 1×10^4 to 6×10^4.
- With the decreasing Rc/D, i.e., for $Rc/D \leq 4$, the strength of the velocity perturbation becomes larger, the pressure gradients in the cross-section increase and

the vorticity becomes stronger. For $Rc/D < 2$, the flow velocity profile becomes highly distorted. With the increasing Re, there is a diminishing trend of the impact of the bend radius on the flow behavior.

Answer to the third research questions:

- The axial velocity profile and the swirl intensity are the main parameters used to investigate the turbulent flow through a 90-degree pipe bend with the honeycomb straightener as the goal with the flow conditioning is to achieve a swirl-free and symmetrical velocity profile in a pipe.
- Although the velocity profile is improved downstream of the honeycomb straightener, it does not reach a good match with the fully developed profile for the studied combinations of the increasing distances from the bend outlet, Lb/D and thicknesses, t/D.
- The swirl intensity decreases faster right behind the honeycomb, when influenced by the increasing Lb/D and t/D, which is as expected for the flow straightener to meet the swirl-free requirement of the flow.
- The optimum installation distance and thickness of the investigated honeycomb design can be assumed as $Lb/D = 5$ and t/D = 0.5, respectively, to achieve the best improvement in smoothing nonuniformities in the flow pattern and become the most successful in removing the swirl in the flow through the pipe.
- In the case of inserting the flow meter downstream of the honeycomb straightener, it is recommended that the device should be installed at the minimum distance of z/D = 15 behind the bend for further investigation of the measurement performance.

6.2. Future work

The future work may be focused on the following:

- Study the effect of the honeycomb openings size on the flow.
- Benchmarking the effectiveness of the honeycomb straightener against other flow conditioners to get an overview of the best performing device with regard to removing the swirl and restoring the velocity profile.
- Study on the measurement performance of the orifice flow meter with the honeycomb downstream of the 90-degree pipe bend. The effect of the honeycomb on the discharge coefficient error could be examined in order to find the optimum honeycomb position from the bend outlet to provide the highest measuring accuracy.
- Study on the effect of different upstream sources of disturbance on the performance of the honeycomb that can contribute to broaden the application of the device in terms of variable upstream flow conditions, other than 90-degree pipe bend.